ASSESSMENT OF SHIP CARGO LIQUEFACTION

By

Lei Ju

A thesis submitted in fulfillment of the requirements for the degree of Doctor of Philosophy

Department of Naval Architecture, Ocean and Marine Engineering
Universities of Strathclyde
March, 2017

Statement

Abstract

Liquefaction of fine particle cargoes such as unprocessed nickel ore and iron ore, resulting in cargo shift and loss of stability of ships, has caused the loss of many lives in marine casualties over the recent few years. Since the dangers of cargo liquefaction have long been known to the shipping industry, the question of why the phenomenon is resurfacing now would be a legitimate one.

Under the requirements of International Maritime Bulk Solid Cargoes (IMSBC) Code adopted by the Maritime Safety Committee of the Organization, the moisture content of the cargo that may liquefy shall be kept less than its Transportable Moisture Limit (TML) in advance of loading, as determined from one of three laboratory test methods specified in IMSBC code. However, the accuracy of these methods is still not understood and the TML result varies particularly when conducted in different laboratories or in different methods for a given sample (Rose, 2014). Considering the ambiguity of testing (unavailability or non-compliance) and the variability in cargo properties and state as well as conditions that can lead to liquefaction (pertaining to ship design and operation and to environmental conditions), it is necessary to investigate the root causes that trigger the phenomenon and address the problem in a comprehensive manner. On the other hand, despite the positive steps that have been taken towards prevention of such shipping accidents, IMSBC code appears to have certain limitations and leaves the shipper responsible to involve the competent authority and the operator for the characterization of the cargo and the hazards it entails for the ship and its crew, if in doubt. This thesis, therefore, gives consideration to the development of the numerical simulation method to the ship cargo liquefaction, which could be feasibly used as a reference and possibly support a suitable regulatory framework for the liquefaction analysis of cargoes.

Acknowledgements

I would like to express my deepest gratitude and appreciation to my supervisor, Professor Dracos Vassalos, whose kindest guidance, patience, understanding, encouragement and support over the past three years. Even during the period when I suspected successful completion of this research, Professor Vassalos always gave me confidence and motivation.

I would like to express my sincere thanks to my external examiner, Professor K.J. Spyrou and my internal examiner, Professor Panagiotis Kaklis for the comments and suggestions with high academic level. I extend a special thank you to Professor Atilla Incecik and Professor Sandy Day for the kindest and most generous financial support for the software licenses.

My sincerest thanks also go to Professor Chengi Kuo, Dr. Evangelos Boulougouris, Dr. Zhiming Yuan, and Mrs. Thelma Will for their kindest help throughout this process. And my heartfelt gratitude goes to Professor Yumin Su in Harbin Engineering University who I learned from for his persistent attitudes toward scientific research. I would like to thank Professor Yang Liu at University of Science & Technology Beijing for discussing the liquefaction research.

I also wish to express my sincerest gratitude to Dr. Wei Jin, Dr. Zhiliang Gao, Mengshi Sun, Enqian Liu, Yuanchuan Liu, Yue Gu, Hanlin Wang, SSRC group members Dimitrios Mermiris, Konstantinos Sfakianakis, Dimitrios Sfakianakis, Rastko Simic, Yu Bi, my MSRC group members Romanas, Sheena, Lin and other colleagues in NAOME. You are the best members I have ever worked together.

My special thanks are for my beloved parents for their devoted love. Whenever I think about how to express my gratitude, it is not enough no matter how to say. Wherever I remember the kindest friendship, bliss will spread across my face.

Publications

1. Ju L., Vassalos D., Jin W., Rolling motion of Newtonian and non-Newtonian fluids in a ship hold, *5th International Maritime Conference on Design for Safety*, November 25-27 2013, Shanghai, China

2. Ju L., Vassalos D., Potential assessment of cargo fluidization based on an UBC3D-PLM model, *12th International Conference on the Stability of Ships and Ocean Vehicles*, June 14-19 2015, Glasgow, UK

3. Ju L., Vassalos D., Boulougouris E., Numerical assessment of cargo liquefaction potential, *Ocean Engineering*, volume 120, p383-388, 2016

Contents

List of Figures

List of Tables

Acronyms/Glossary

Angle of Repose: The steepest angle of descent to the horizontal plane to which a material can be piled without slumping.

BC Code: The problems involved in the carriage of bulk cargoes were recognized by the delegates to the 1960 International Conference on Safety of Life at Sea. The first edition of the Code of Safe Practice for Solid Bulk Cargoes (BC Code) had been published in 1965 by Sub-Committee of International Maritime Organization (IMO).

CFD (Computational Fluid Dynamics): A branch of fluid mechanics that uses numerical analysis and algorithms to solve and analyze problems that involve fluid flows.

CMAT (Contact Model Assignment Table): A very generic tool that can handle both built-in contact models and user-defined contact models in PFC software.

DEM (Discrete Element Method): DEM is a method to compute the motion and effect of a large number of small particles.

DSS (Direct Simple Shear): The direct simple shear test is a laboratory testing method used to directly determine the shear modulus of soil.

Degree of Saturation (S): Volume of water within the inter-particle voids of a granular material (such as a dry bulk commodity). It is expressed as a percentage, where water completely fills the voids at S=100% and the material is completely dry at S=0%.

FMP (Flow Moisture Content): The lowest moisture content at which liquefaction can occur which can be determined in the laboratory.

FEM (Finite Element Method): FEM is a numerical technique for finding approximate solutions to boundary value problems for partial differential equations.

Fric (Friction Coefficient): A parameter in rolling resistance linear model.

Group A Cargo: Cargoes which may liquefy if shipped at moisture content (MC) in excess of the transportable moisture limit (TML) [Ref. IMSBC Code 1.7.12].

IMSBC Code (International Maritime Solid Bulk Cargoes): The International Maritime Solid Bulk Cargoes (IMSBC) Code is the regulatory tool used by IMO to ensure the safe carriage of solid bulk materials.

IMO (International Maritime Organization): A sub-body of the UN and the international maritime regulator. Renamed from the Inter-Governmental Maritime Consultative Organization (IMCO) in 1982.

MC (Moisture Content): The portion of a representative sample consisting of water, ice or other liquid expressed as a percentage of the total wet mass of that sample [Ref. IMSBC Code 1.7.20].

NS (Navier-Stokes): The Navier-Stokes equations are the fundamental partial differentials equations that describe the flow of incompressible fluids.

PFC (Particle Flow Code): PFC is advanced, fast and extremely versatile commercial, multi-physics simulation software.

Rfric (Rolling Friction Coefficient): A parameter in rolling resistance linear model.

TxC (tri-axial shear test): A common method to measure the mechanical properties of many deformable solids, especially soil (e.g., sand, clay) and rock, and other granular materials.

TML (Transportable Moisture Limit): A concept within the IMSBC Code that represents the maximum moisture at which a Group A cargo can be safely loaded to prevent liquefaction (TML [% moisture] = 90% × FMP [% moisture]).

Chapter 1 Introduction

1.1 Background

Over the past few years, the risk of cargo liquefaction on ship safety has risen sharply. The liquefaction of mineral ores, such as iron ore and nickel ore from India, Indonesia, the Philippines and New Caledonia, can result in cargo displacement (‘cargo shift’) and loss of ship stability, which has been a major cause of marine casualties. Forces applied by the ship’s motion and the engine vibration during passage may cause particle re-arrangement and compaction. The gaps between the particles become smaller in the process, with the corresponding pore pressure progressively increasing. As a result, the water holding ability of particles and the friction coefficient between cargoes decreases. In particular, the water in the interstellar spaces comes together to form a liquid layer that allows the cargo above to move relative to the cargo below — as if the two layers were part of a liquid, and hence the term ‘liquefaction’. Such a transition during ocean carriage can cause a sudden loss of stability of the carrying vessel. In the ClassNK magazine 64th edition, it read that from the end of 2010 to the end of 2011, for a period of approximately a year, four ships capsized and sank due to a loss of hull stability attributed to the liquefaction of cargo. Those ships were M/V “JIAN FU STAR”, M/V “NASCO DIAMOND”, M/V “HONG WEI” and M/V “VINALINES QUEEN”, with each of those having departed from the Indonesian ports of Obi Island, Tahuna, Bitung and Morowali. A total of 66 crew members were killed. Appendix 1 includes the abysmal record of the past seven years and a series of submissions to IMO have taken place over the years pertaining to the potential of a cargo. The above tragic accident is not the only one of its kind and unfortunately, it will not be the last unless immediate and comprehensive action is taken by the industry.

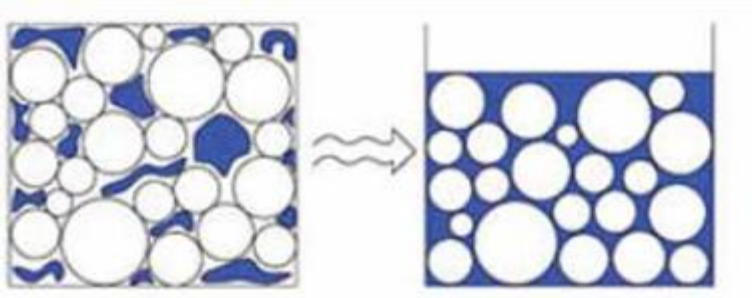

Figure 1.1 Transition from solid state to fluid state (Publication from Gard, 2014)

The mechanisms that cause a solid bulk cargo to liquefy are complex. Cargoes in nature contain certain moisture, as shown in Figure 1.1. It is this moisture that leads to the risk of liquefaction, although the moisture in the cargoes is not visibly wet in appearance. The most widely known cargoes with this hazard are nickel ore and iron ore, which are widely distributed all over the world. These cargoes are usually in their solid state during the act of ship loading, with particles in direct contact with each other and, therefore, there is a physical strength of resistance to shear strains. On the other hand, cargoes like mineral ores loaded onboard a vessel have granular material which is exposed to mechanical agitation and energy input in the form of engine vibrations, vessel movement, and wave impact. This results in a gradual settling and compaction of the cargo. The gaps between particles become smaller and the air is exhausted in the process, while the pore water pressure between particles increases sharply, pressing the particles away from each other. Internal friction weakens as particles are no longer in direct contact and the cargo turns into a viscous fluid, i.e. all or partial cargoes have liquefied.

Cargo liquefaction is susceptible to a wide range of factors that influences a cargo's likelihood to shift, such as the properties of the cargo, the ability to hold water, the initial moisture content, the moisture migration (climate), loading conditions (the porosity and the confining pressure) and the type of cargo ship. The liquefied cargoes, or partially liquefied cargoes, flow to one side of the ship with a roll but do not completely return with a roll to the other direction, with the risk of the ship progressively reaching a dangerous heel and capsizing. It is unpredictable, rapid, and deadly. During the process of

liquefaction, the cargo will experience a transition from solid to partially liquefied state, and then to a fully liquefied state. All of these three states have an impact on ship stability, which cannot be addressed separately.

1.2 Methodology

Numerical simulations examining liquefaction to date are focused on the earthquake liquefaction based on the Finite Element Method (Unno, 2008; Byrne, 2004). Conventional procedures used to assess liquefaction broadly tend to predict the triggering of liquefaction. However, assessment of ship cargo liquefaction, which is the concern in this research, needs to investigate the interaction between cargo displacement and ship response through the liquefaction process. Ship stability due to cargo shift is an interdisciplinary problem that demands a practical method and solution, including:

1) Soil Mechanics: Cargo liquefaction and cargo shift, which interacts with structure movement, will be addressed in this section.
2) Maritime Engineering: Ship stability in waves contributed by cargo displacement will be addressed in this section.

Therefore, a new simulation method based on the existing theoretical basis will be developed in order to address these problems. In the soil mechanics section, the problems which need to be addressed include cargo liquefaction and cargo shift. Commercial software (PFC2d) based on the Discrete Element Method (DEM) is used in the thesis to describe the cargo shift of granular particles (Chapter 5). The UBCSAND liquefaction model will be embedded in the DEM code, which will address the information in cargo liquefaction (Chapter 6). In the section of Maritime Engineering, ship response in waves will be simulated using ANSYS Fluent software. A CFD-DEM adapter will be developed to exchange key data between PFC2d and ANSYS Fluent software to investigate the coupled interaction (Chapter 7). This simulation method will address the ship cargo liquefaction problem and the ship response due to cargo shift in a holistic way. However, there still needs to be significant experimental data to validate this simulation method.

1.3 Contributions of This Study

Broadly, the contribution of this work is the introduction of a new method which takes into account cargo shift, cargo deformation, and its interaction with ship response. In particular, the contributions accruing from the research are:

1) The evaluation of methods currently in use in the research on cargo liquefaction, especially for the interaction between ship response and cargo shift.
2) DEM applications to cargo shift based on commercial software (PFC2d).
3) The development of the DEM liquefaction model, giving consideration to cargo shift and deformation.
4) The development of a new method for investigating the ship response in waves due to cargo shift.

1.4 Scope of This Study

Since the liquefaction of mineral ores, resulting in cargo shift and loss of stability, has been a major cause of marine casualties for many decades, attention needs to be paid to the carriage of unprocessed natural ores. The overall scope of this study is to assess the liquefaction potential in the process of carriage of cargoes. This method could be used as a reference and possibly support a suitable regulatory framework for liquefaction analysis of ship stability so that decision making during the loading and transport process is effective in avoiding ship capsizes and casualties.

The present research aims are:

1) to simulate cargo liquefaction based on the CFD and DEM models;
2) to identify cargo shift at various moisture contents based on the DEM;
3) to analyze the whole liquefaction process from unsaturated state to saturated state based on the DEM;
4) to study ship response in waves due to cargo shift based on a CFD-DEM adapter.

The study is subdivided into eight sections addressing the research aims above. The layout of the thesis is as follow:

In Chapter 1, the background and motivation of this thesis are presented followed by the mechanism of cargo liquefaction and its interaction with ship stability. In addition, the methodology in the thesis is addressed briefly.

In Chapter 2, a key literature review of present methods of research on cargo liquefaction to date is given, focusing on the existing regulations and guidelines and the scientific methods for predicting liquefaction.

Chapter 3 summarizes the numerical models in the thesis, which includes how to solve the problems of granular cargo flow and ship response. Stress calculation and elastic-plastic strain are also presented in this chapter.

Chapter 4 investigates the present simulation methods to solve the liquefaction problems. To some extent, the current methods based on the Finite Element Method and Finite Volume Method cannot address this problem thoroughly. Thus, the limitations of present methods are stated in this chapter.

In Chapter 5, the granular particle flow based on the DEM is simulated to compare with the nickel ore flow to identify contact properties at various moisture contents. Dynamic stability analysis is conducted to identify the fluctuation force due to cargo shift on the containers by varying the degree of saturation, frequency, and amplitude.

In Chapter 6, a liquefaction model based on the DEM is presented. Simple shear and cyclic shear simulations are conducted to validate the model. A new liquefaction assessment criterion is discussed based on this liquefaction model.

In Chapter 7, a CFD-DEM adapter is developed as an attempt to investigate the effect of

cargo flow due to cargo liquefaction on the ship response in waves. CFD numerical validation and DEM numerical validation focusing on the sensitivities of grid size, time-step size and particle numbers are investigated. In addition, coupled motion in waves based on the CFD-DEM adapter will be simulated, to identify the sensitivities of particle numbers.

In the last chapter (Chapter 8), the major conclusions, discussions and recommendations are presented. In following research, experimental work will be carried out to validate the numerical model.

Chapter 2 Literature Review

Brazil is the world's largest iron ore producer and exporter, accounting for about 25% of the global market share of iron ore trade volume (Market Realist, 2015). Based on the significant transportation amount and frequency of accidents (see Appendix 1) occurring in the last 20 years, cargo liquefaction has long been an interest of the shipping industry. Despite this, there has been limited research on cargo liquefaction.

The interaction between ship motion and cargo displacement can lead to capsizing. However, researchers to date have not considered these problems in a holistic way. To prevent ship capsizing due to cargo liquefaction, organizations such as IMO, ClassNK and Technical Working Group have carried out preliminary explorations and created some regulations and guidelines. As known, iron ore or nickel ore behaves like soil. Soil liquefaction happens frequently in an earthquake. At present, liquefaction models have been developed by researchers focusing on earthquake liquefaction. Obviously, loss of ship stability due to cargo shift is a cargo-sea-ship problem. These three aspects cannot be analyzed separately. Therefore, how to solve these three problems based on numerical simulations and laboratory experiments is a pressing issue. In this chapter, a literature review about ship capsizing due to cargo shift will be summarized, including regulations and guidelines, and scientific methods for predicting cargo shift — especially for the liquefaction phenomenon (Figure 2.1).

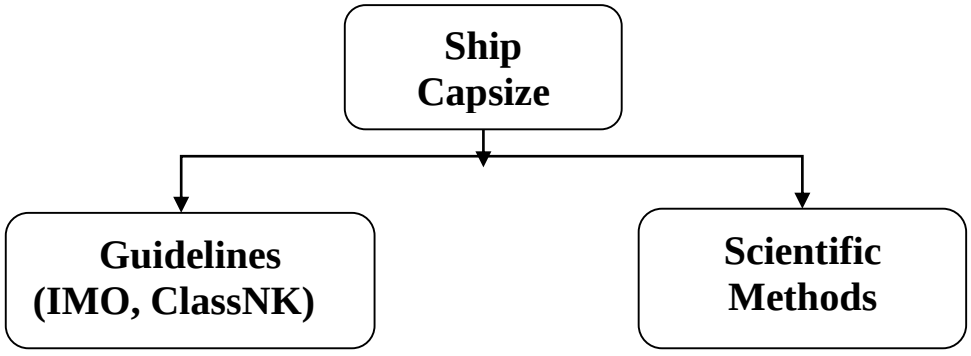

Figure 2.1 Framework of key literature reviews

2.1 Regulations and Guidelines

2.1.1 IMSBC Code

Liquefaction problems involved in the carriage of bulk cargoes were recognized by the delegates to the 1960 International Conference on Safety of Life at Sea. The first edition of the Code of Safe Practice for Solid Bulk Cargoes (BC Code) had been published in 1965 by Sub-Committee of International Maritime Organization (IMO).

With the stimulus, compaction and vibration of cargoes during a voyage, cargoes like iron ore and nickel ore may become fluid. Ship motion may cause liquefied cargoes to shift such that the vessel may capsize. Cargo shift can be divided into two types, including sliding failure or liquefaction consequence as summarized in the IMSBC code. In actual fact, the sliding failure and liquefaction consequence exist simultaneously. The sliding failure may occur when liquefaction accumulates to a certain degree, which further intensifies the onset of liquefaction.

The moisture content of cargoes is a key parameter which is relevant to liquefaction. If the moisture is below a certain level, the interstitial spaces between the particles could accommodate all of the moisture such that the increase of pore water pressure is inhibited during compaction. Liquefaction does not occur when the cargo contains very small particles; the cargo consists of large particles or lumps; the cargo contains low moisture content. In these three cases, cargo movement can be restricted and water will pass through the large porosity. When moisture content exceeds the Transportable Moisture Limit (TML), cargo may liquefy and generate a dangerous wet base (IMSBC code). Therefore, TML is the estimation criterion for the carriage of solid bulk cargoes. The test procedures for cargo TML will be explained in Appendix 2.

Nickel ore is newly being categorized as Group A cargo in IMSBC code. Group A Cargoes mean cargoes which may liquefy if shipped at moisture content (MC) in excess of the

transportable moisture limit (TML). The lowest moisture content at which liquefaction can occur is called the Flow Moisture Point (commonly abbreviated FMP) which can be determined in the laboratory. TML is a parameter that is calculated as 0.9 times the FMP. The numerical value of FMP must be determined by laboratory testing. If the moisture content of cargoes exceeds the FMP, liquefaction may occur at any time during the voyage. Even the moisture content is below the FMP, liquefaction may also occur (TWG report, 2013). At the time of loading cargoes, compaction may occur, resulting in liquefaction or cargo shift. It is for these reasons that the IMSBC Code incorporates provisions intended to ensure that, to avoid liquefaction, only cargoes with sufficiently low inherent moisture content are loaded.

Despite the fact that the IMSBC Code prescribes the testing and certification requirements designed to ensure that cargoes are loaded only if the moisture content is sufficiently low to avoid liquefaction occurring during the voyage, inaccurate declarations and certificates from shippers still appear to be at the heart of the problem.

2.1.2 Guidelines of ClassNK

Nickel ore with a diameter below 10mm with various moisture contents is shown in Figure 2.2 and Figure 2.3 (ClassNK, 2013). As the moisture content increases, the samples become increasingly muddy in appearance. In the Guidelines for the Safe Carriage of Nickel Ore, there is a focus on recommendations, how to test the TML and take precautions during the carriage of nickel ore. As introduced in the IMSBC code, cargoes with moisture content in excess of TML should not be loaded on the ship. Even cargoes with moisture content less than the TML have the risk of liquefaction because of measurement error and atmospheric moisture migration. Therefore, some precautions have been given to enhance ship security during voyages. The precautions in the guidelines will be explained in Appendix 3. The work conducted by ClassNK has combined laboratory measurements and numerical simulations aimed at developing a set of operational guidelines pertaining to the stability and strength of carrier ships. However,

it focused on how to test the TML and took precautions during the carriage of nickel ore.

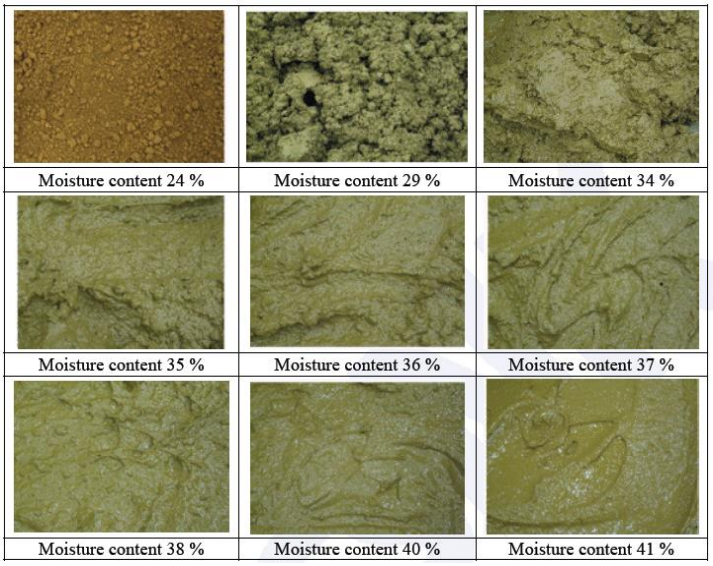

Figure 2.2 Appearance of nickel ore samples with various moisture contents (Indonesian Product)

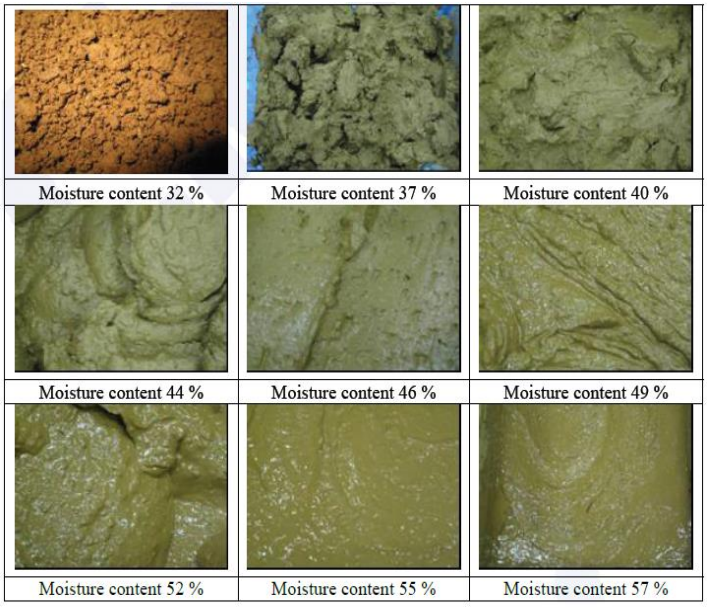

Figure 2.3 Appearance of nickel ore samples with various moisture contents (Philippines Product)

2.1.3 TWG Report

The Iron Ore Technical Working Group (TWG, 2013) has expended considerable effort on the evaluation and verification of liquefaction and considered the adequacy of current methods for determining the Transportable Moisture Limit (TML). The Technical Working Group (TWG), comprising one Brazilian and two Australian mining companies, has undertaken a program of research on representative Australian and Brazilian Iron Ore Fines (IOF) materials to assess their behavior when seaborne transported in bulk, with emphasis on liquefaction aspects (Appendix 4). However, the research appears to focus on cargo liquefaction based on the traditional criteria of earthquake liquefaction, which may not apply to the ship solid bulk cargo transportation problem. More importantly, the research separated cargo shift from ship stability, with all the ensuing limitations, i.e., emphasis correctly put on avoiding the hazard but without due consideration to the impact of its occurrence (not a "fail-safe" system), which is an uncharacteristic approach when applied to safety-critical systems (loss of human life at stake).

2.2 Scientific Methods for Predicting Liquefaction

2.2.1 Granular Material

As seen in Figure 2.3, granular materials show a great variety of particle size distributions, shapes, and moisture contents. Also, mining in various ore mine fields determines the property and behavior of the cargo. Granular materials are simple but behave differently considering the combination of liquid, gas, and water. Some distinctive properties of granular materials are discussed by Jaeger et al. (1996). Granular materials can flow like fluids. However, granular flow cannot behave like water and be described by Navier-Stokes (Spandonidis and Spyrou, 2016). The behavior of granular cargoes transported by sea has not been sufficiently investigated at present. A simulation approach was developed based on molecular dynamics, combined with a rudimentary model of vessel motion in beam seas (Spandonidis and Spyrou, 2012). Coupling ship motion with cargo flow was

conducted to identify the effect of shifting cargo on a vessel's motion. The simulation approach effectively captured vessel dynamics due to its comparison between cargo movement and experimental data.

Ship's motion may cause a cargo to shift sufficiently to capsize the vessel. Cargo shift can be divided into two types, namely, sliding failure or liquefaction consequence (IMSBC code). Some cargoes may appear to be in a relatively dry state when loading. However, it may still contain a certain amount of moisture. According to IMSBC code, liquefaction does not occur if the cargo contains very small particles because particle movement will be restricted by cohesion; the cargo contains very large particles because water will pass through the large spaces, and the cargo contains low moisture content. During the voyage, with stimulus and compaction, cargoes can change into a fluid state gradually. Cargo liquefaction may weaken the shear strength and friction between particles due to compaction, resulting in high flow characteristics of cargoes. The common contributor to the capsizing of ships is that cargo flows to one side and does not flow to the other side with a roll, which shifts the center of gravity and weakens ship stability. Even for dry cargoes, ship stability may result in dry cargo shift or sliding failure. Sliding failure may occur when piles of cargo inclines to certain angles, resulting in the breaking of the angle of repose.

2.2.2 Angle of Repose

The angle of repose of granular material is the steepest angle of descent to the horizontal plane to which a material can be piled without slumping. It is a basic property of non-cohesive granular materials: the maximum slope angle at which the material is at rest (Lowe, 1976). When exceeding this angle, the granular material begins to flow. The angle of repose is a key parameter in many geomorphological phenomena. Angles of repose can be determined in three different manners: 1) Experiments were done with various granular materials to determine the angle of repose as a function of material properties and to determine direct relations between the angle of repose, runout length and dynamics; 2)

slope angles of dry or submerged dense granular flow deposits were measured in nature, including on other planets and the Moon; 3) physics-based numerical models were run whereby resulting morphology and dynamics such as velocity and runout length were matched to a real case by calibrating the angle of repose (Kleinhans et al, 2011). To determine the angle of repose, the evolution of the free surface for several rates of tilting was monitored and a series of sway and heave tank oscillations recording the movement of material's centre of mass has been performed by Spandonidis and Spyrou (2013). Cargo stability influences ship stability directly. In IMSBC code, for non-cohesive bulk cargoes having an angle of repose greater than 30° to 35°, the cargoes shall be trimmed according to the following criteria for improving the cargo instability:

1) the unevenness of the cargo surface measured as the vertical distance (Δ h) between the highest and lowest levels of the cargo surface shall not exceed B/10, where B is the beam of the ship in metres, with a maximum allowable Δ h = 1.5m, or
2) Loading is carried out using trimming equipment approved by the competent authority.

2.2.3 Granular Material Liquefaction

Experimental methods

To address the granular material liquefaction phenomena, experimental works have been conducted by researchers. The effects of soil water saturation on the liquefaction of Hostun RF sand was designed by Arab et al. (2012), and indicated that a low saturation level will increase liquefaction resistance. The results are in accordance with the conclusions in the tri-axial cyclic shear tests conducted by Zhou (2013; 2014). Cyclic loading on iron ore concentrate was conducted to study the deformation and mechanical properties of iron ore concentrate. When the moisture content was above the critical moisture content, the sample would slowly be destroyed even under a small dynamic stress or sufficiently long vibration times. Liquefaction of granular materials in a rectangular container has also been experimentally investigated by Koromila et al. (2013), who developed some insights into

how the liquefaction phenomenon related to the duration of liquefaction and intensity of excitation on a rectangular container based on two different materials (sand and olive pomace) containing various moisture contents. Their experiments indicate that homogeneous cargo loading can lead to substantial loss of stability after cargo liquefaction. Even at small dynamic stresses on particles with sufficient periods of vibration, the cargoes will lose effective stress and reach a state of failure (Unno, 2006).

Continuum methods

Most liquefaction models are based on continuum methods, such as the Finite Element Method (FEM). This effective stress model describes the stress-strain behavior in soil dynamics. The concept of effective stress for saturated soils was introduced by Terzaghi (1936). Effective stress (σ') acting on soil is calculated from two parameters: total stress (σ) and pore water pressure (u). Following this, many researchers have proposed different methods based on the effective model (e.g., Biot, 1941; Nurand and Byerlee, 1971).

$$\sigma' = \sigma - u$$

Since the application of the effective stress concept has made a great contribution to the study of saturated soil, many researchers extended this concept from a saturated state to an unsaturated state. The modified generalization of the effective stress for unsaturated soil was proposed by Bishop (1959). The relationship between χ and the degree of saturation was obtained experimentally.

$$\sigma' = (\sigma - p_a I) + \chi s_c I$$

σ': the effective stress tensor

σ: the total stress tensor

χ: the Bishop's parameter

s_c: the matric suction, which is $p_a - p_w$

I: the second order unit tensor

After the proposed effective stress for unsaturated soil, many researchers carried on the

study to describe unsaturated soil behavior (Jennings, 1961; Coleman, 1962; Blight, 1967). Most research was based on the Bishop's equation. A numerical model was developed by Hanbing Bian (2007) to describe the behavior of unsaturated soils under seismic loading. For sandy soil in partially saturated conditions, for example, when the volumetric water content exceeds a certain value (50%), the soil suction is negligible, with the difference of pore-water pressure and pore-air pressure being close to zero. The contractile skin effects are also neglected. An elastoplastic model (Sun, 2007) was presented to predict the hydraulic and stress–strain behavior of unsaturated soils. The model takes into consideration the effect of the degree of saturation on stress-strain behavior, the effect of the void ratio on water-retention behavior, and the influence of suction. Model predictions of the stress–strain and water-retention response are compared with those obtained from triaxial tests on unsaturated soil during isotropic and shear loading with and without suction change. The coupled unsaturated hydraulic-mechanical elastoplastic model was presented by Liu Chunyang (2009). Stress-strain variables were derived and based on the theory of mixtures with interfaces (Muraleetharan and Wei, 1999), a soil water characteristic curve with a framework of elastoplasticity is coupled with the deformation of the soil skeleton.

The UBCSAND model is widely used to predict soil liquefaction. The liquefaction model, based on commercial software, PLAXIS, was used to describe the mechanical behavior of soils under cyclic shear (Ju, 2016). The UBCSAND model was developed at the University of British Colombia, which utilized isotropic and kinematic hardening rules for primary and secondary yield surfaces to properly take into account the accumulation of excess pore water pressure and effects of soil densification during cyclic loading. By means of a simplified Rowe's stress-dilatancy theory, the model is capable of modeling liquefaction for different stress paths (Galavi, 2013). The UBCSAND model is thus an effective stress plasticity model for use in advanced stress-deformation analyses of geotechnical structures (Beaty et al., 2011). The model was developed primarily for sand-like soils which has the potential for liquefaction under seismic loading. It was used to predict the shear stress-strain behavior of the soil using an assumed hyperbolic

relationship and was able to estimate the associated volumetric response of the soil skeleton using a flow rule that is a function of the current stress ratio. One of the first uses of the UBCSAND model was to predict the behavior of the CANLEX (Canadian Liquefaction Experiment) embankments. The fills were rapidly constructed on loose tailing deposits to create a liquefaction response (Puebla et al., 1997). This model was soon adapted to seismic evaluations and applied to the response analysis of the Wildlife Site and the Superstition Hills Earthquake of 1987 (Beaty and Byrne, 1998).

Discrete element methods

Most of the methods for liquefaction are based on the effective stress model to establish a constitutive equation. This lacks the study of discrete characteristics of cargo flow. Cargoes like iron ore and nickel ore behave like soils. Thus, to study ship stability due to cargo movement, a molecular dynamics method can be used to predict cargo shift and ship response in a holistic way (Spandonidis and Spyrou, 2013). The DEM method was originally developed by Cundall in 1971 to address problems in rock mechanics (with a theoretical basis established by Isaac Newton in 1697). The DEM modeling approach is widely used in the soil response analysis (Zhou, 2009; Dabeet, 2012, 2014; Xue, 2014).

Coupled continuum-discrete model is widely proposed and developed to simulate the mesoscale pore water flow and solid matrix deformation of saturated soil, by solving the Navier-Stokes equation for fluid, linear and angular momentum for each particle (Shamy, 2005). CFDEM project[1] is an open source high-performance scientific computing in fluid mechanics and particle science by CFDEM research GmbH. The motion of the particles is resolved with DEM, and the CFD method is used to calculate the fluid flow. The granular phase which occupies a certain volume in each computational cell is accounted for by introducing a "volume fraction" into the Navier-Stokes equations. Furthermore, the granular and fluid phase can exchange momentum, heat, and mass. Some typical

[1] http://www.cfdem.com/

applications for the CFD-DEM method are the simulation such as fluidized beds, metallurgical processes (e.g. blast furnace), pneumatic conveying chemical and pharamceutical reactors any kind of granular flow influenced by the interstitial fluid phase (Goniva, 2012). However, the CFD-DEM method at present is based on a saturated state, while ship cargoes contain three phases: water, air and soil, which reflect an unsaturated state. Thus when considering the unsaturated state, the soil suction should be included into the dynamic equation.

2.2.4 Sea-Cargo-Ship Problem

Cargo shift will influence the position of the centre of gravity of the ship, resulting in a large angle of heel. As the Figure 2.4(a) shows, the weight (W) of the ship acts downward through the centre of gravity of the ship (G). This force is resisted by an upward buoyant force equal to W through the centre of buoyancy (B) which is the geometric centre of the submerged volume displaced by the ship. At stable state, B and G keep in line along the vertical direction. With an external force on the ship (from wind or waves), the ship will result in a large heel. This will result in B to shift while G will not move. This variation will cause a righting moment (W*GZ) and the ship will oscillate from one side to the other side. If transverse cargo shift occurs, it is possible for B and G to reverse position, as shown in Figure 2.4(b) which can result in the ship capsizing quickly (Committee on Ship's Ballast Operations, 1996).

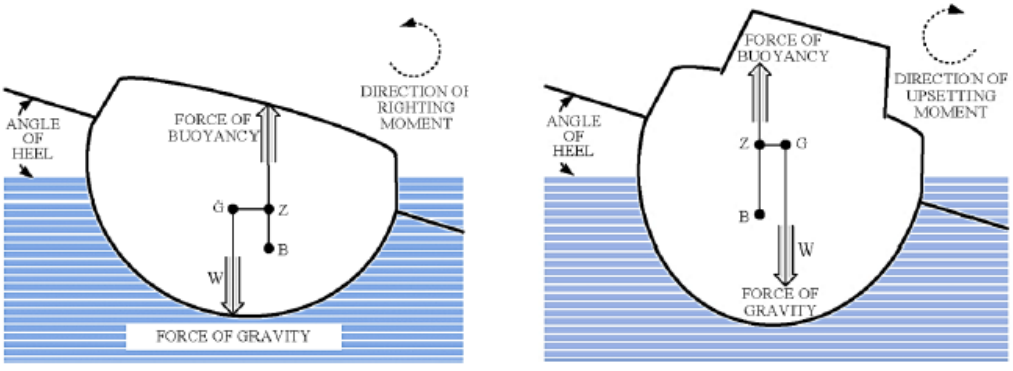

Figure 2.4 (a) Stable ship inclining and (b) GZ become negative, causing capsize (Rose, 2014)

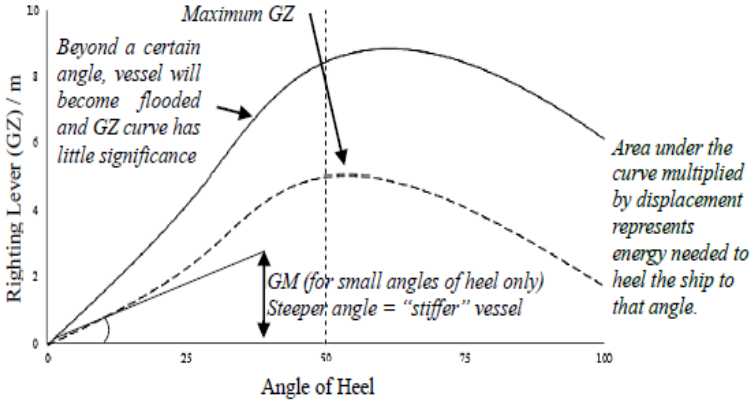

Figure 2.5 Key features of a GZ stability curve. Before liquefaction (solid line) and after liquefaction (dashed line) (Koromila et al., 2013)

A ship's stability is often expressed by the 'stability curve' (Figure 2.5), which provides information about the righting lever (GZ) for any angle of heel (based on an assumed centre of gravity). Some information can be obtained by this curve: 1) the range of stability; 2) the angle of vanishing stability; 3) the maximum GZ, and 4) the initial GM. It also compares the ship stability before and after cargo liquefaction by Koromila et al (2013). It shows that when cargo liquefied, the ship stability will decrease greatly.

Cargoes at risk of liquefaction include those with moisture, air, and solid skeletons. Before loading, the cargoes may look dry, however, the ship motion will compact the cargoes and rearrange, resulting in the loss of water holding ability. The pore water pressure between particles will increase and the shear strength will decrease, causing major displacement of cargo, termed cargo liquefaction (see Figure 2.6). The whole process of ship loss due to cargo liquefaction is displayed in Figure 2.7.

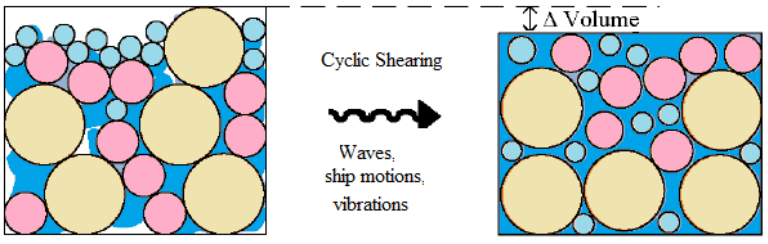

Figure 2.6 The granular particles: Before liquefaction (left) and after liquefaction (right)

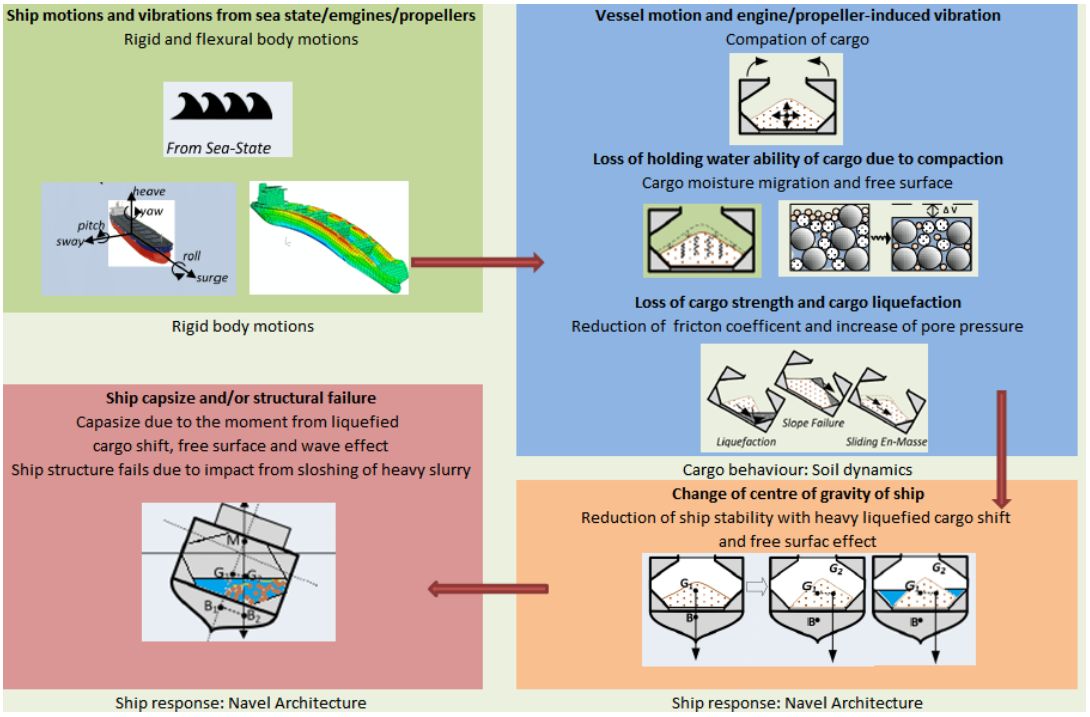

Figure 2.7 Illustration of liquefaction phenomenon and ensuing effects (Rose, 2014)

Liquefied cargo will behave as a non-Newtonian fluid which flows to one side with roll but cannot flow to the other side in a timely manner (Ju et al, 2013). The accurate predictions of highly nonlinear free-surface flows and the impact by fluid are very important, especially in waves. Many researchers have conducted work on the interaction between water flow and ship motion in waves (Zhao, 2012; Lee, 2010; Toumi, 2009; Andrei, 2013). However, there are some limitations based on the continuum methods. Cargo shift with nickel ore or iron ore reflects a discrete character along with the occurrence of liquefaction. Micro-scale granular method based molecular dynamics can solve these problems better (Spandonidis and Spyrou, 2013). The micro-scale modeling approach was developed to simulate the dynamic behavior of granular materials having physical properties and conforming to bulky ship cargos. This method predicted cargo shift and related phenomena. Container dimensions, the number of particles, and filling ratio variations are considered to study the surface profile and centre of mass. When experiencing the sway, heave and roll motion, the shift of a cargo's centre of mass changes with time (Spandonidis and Spyrou, 2016). The Discrete Element Method (DEM) has been

applied to solve ship related problems in recent years. For example, the interaction between drifting pancake ice floes and moored ships have been simulated with the DEM. The pancake ice floes are modelled with three-dimensional discrete elements by considering the buoyancy, drag force and added mass of current. The ship hull is constructed with combined discrete elements via certain overlaps. The interaction between ice floe and ship hull is determined through element contact detection and impact force calculation (S Ji, 2013).

Two simulation methods are discussed below to investigate the behavior of granular particles.

Soft sphere molecular dynamics (MD=DEM)

The DEM was originally developed by Cundall in 1971 to address problems in rock mechanics. Essentially, MD and DEM are identical in terms of particle shape and both methods are based on Newton's second law. MD studies the physical movement of atoms and molecules, which is applied today mostly in chemical physics, material science and the modelling of biomolecules. MD can simulate a wide variety of granular flow in static and dynamic conditions. However, the maximum number of particles is limited by computation ability. DEM considers the rotation movement, particle shape, and distribution of particles. Three codes based on MD (DEM) will be introduced as below:

Code developed by NTUA

The "Molecular Dynamics" method was developed by Spandonidis and Spyrou (2013) at the National Technical University of Athens based on the method developed by Poschel & Schwager (2005), presenting some distinctive features:

1) The code can solve the coupled roll-granular cargo problem formulation to the ship's body. Two problems have been tackled simultaneously: prediction of the wave-induced ship motion and prediction of the motion of a granular particle in the hold.
2) Two interaction forces have been analyze: dry granular solids and granular solids with humidity. Particularly for the particles with humidity, it brings dry granular solids to

wet granular solids, which are much closer to the reality of unsaturated cargoes.

Lammps

LAMMPS is a classical molecular dynamics code which can be used to model atoms. However, due to the limitation of no pair-style capability between particles, LAMMPS is not suitable to model the cargo shift or its interaction with ship movement.

PFC

Particle Flow Code (PFC) is advanced multi-physics simulation software based on the DEM. The particles are rigid bodies using the soft contact approach, where the particles are allowed to overlap at contact points. Particles interact with each other at pair-wish contacts by means of an internal force and moment, which provides a dynamic solution to Newton's laws of motion. One of the assumptions is that particles are treated as rigid bodies. However, elastic-plastic strain of the cargo occurs during compaction. In this thesis, PFC software is used based on some assumptions.

Event-driven (ED) simulation

ED is conceptually different from DEM since collisions are dealt with using a collision matrix that determines the momentum change on physical grounds. ED is also called hard sphere modelling. Particles are assumed to be rigid and follow a disturbed motion until a collision occurs (Lubachevsky, 1991; Miller, 2004). It is purely algebraic calculations, however, the instantaneous nature of hard sphere collisions is artificial, and it is a valid limit in many circumstances. Even though details of the contact or collision behavior of two particles are ignored, the hard sphere model is valid when binary collisions dominate and multi-particle contacts are rare. The lack of physical information in the model allows a much simpler treatment of collisions (Luding, 2008).

2.3 Conclusions

The above literature review illustrates the current guidelines and methods to solve liquefaction problems. The limitations of the current guidelines have been discussed. Granular material liquefaction has been introduced by means of experimental methods, continuum methods and discrete element methods. Focusing on ship stability due to cargo shift in this thesis, a molecular dynamics method or discrete element method is more suitable to model the discrete character of cargo flow. PFC software is applied to describe the granular material flow based on the rolling resistance linear model, which can shape the angle of repose by incorporating rolling torque to control the roll motion. In addition, ship stability coupled with cargo shift is a sea-ship-cargo problem, which needs to be investigated in a holistic way.

Chapter 3 Basic Mathematical Model

The adopted modelling approach is explained in this chapter. The model can simulate both cargo shift due to cargo liquefaction and the ship response in waves. Based on the DEM (Discrete Element Method) theory, the flow of the particles can be simulated by the Newton's second law. Accordingly, elastic-plastic strain of each particle can be calculated by the UBCSAND model and the pore water pressure can be obtained by the hydraulic model. Based on the assumptions that one ball is regarded as a hypothetical assembler of particles, the radius of ball can be scaled with the elastic-plastic strain and the flow characteristics of cargoes in various moisture content can be approximately modelled by according friction coefficient, the DEM liquefaction model will be developed. The whole liquefaction process can be addressed by this model to capture the process from initial state to liquefied state of cargoes.

The response of the ship vessel in waves can be simulated by the CFD software ANSYS Fluent. The momentum equation, continuity equation and Volume of Fluid (VOF) equation are presented in this chapter. Combined with dynamic meshing method, a two-dimensional wave tank will be established.

Based on the development of the CFD-DEM adapter, the DEM liquefaction model is combined with ANSYS Fluent software to assess the response of ship vessel in waves due to cargo shift, particularly addressing the liquefaction phenomenon. The validation of the approach will be presented in Chapter 5 and Chapter 6.

3.1 DEM Dynamics Simulation

The Particle Flow Code (PFC) is based on DEM, which simulates the movement of granular particles and the interaction between particles. The particles are rigid which move independently, translate and rotate. The interaction between particles is based on the

means of pair-wise contacts. Contact mechanics is embodied in particle-interaction laws that update the internal forces and moments. The time evolution of this system is computed, which provides an explicit dynamic solution to Newton's laws of motion (PFC help manual). Detailed information about PFC is explained in Appendix 5(A). As discussed in Chapter 2, FEM cannot describe the discrete characteristics of granular particles, while DEM can solve this problem more precisely. Therefore, the modelling approach is mainly based on PFC software to describe cargo flow.

Elastic-plastic strain of particles will be formed during compaction. According to the *dynamic stress* on particles, the elastic-plastic strain can be identified based on the UBCSAND model. With the deformation of each particle, the degree of saturation can be obtained and the pore water pressure can be calculated according to the *Soil Water Characteristic Curve (SWCC)*. When conducting the laboratory experiments, the pore water pressure can be tested by the pressure sensor to validate the model.

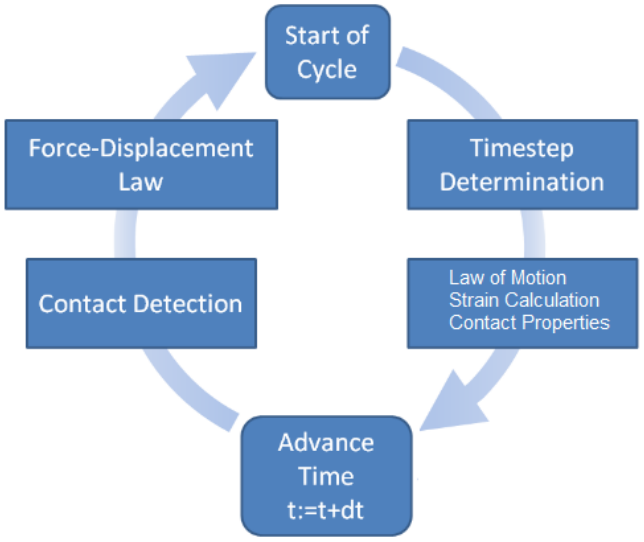

Figure 3.1 Sequence of primary operations that occur during each cycle, termed the cycle sequence

The cycle sequence is the sequence of operations that are executed during a single PFC cycle. These operations include (Figure 3.1):

1) Timestep Determination - The DEM method requires a valid, finite timestep to ensure the numerical stability of the model and that all contacts are created between pieces prior to the point that forces/moments develop between interacting bodies.
2) Law of Motion - The position and velocity of each body/piece is updated according to Newton's laws of motion using the current timestep and the forces/moments calculated during the previous cycle.
3) Strain Calculation -According to the stress on the particles, the elastic-plastic strain is updated by scaling the radius of each particle.
4) Contact Properties -With the updated degree of saturation, the contact properties are updated.
5) Advance Time - The model time is advanced by adding the current timestep to the previous model time.
6) Contact Detection - Contacts are dynamically created/deleted based on the current piece positions.
7) Force-Displacement Law - The forces/moments developing at each contact are updated by the appropriate contact model using the current state of the pieces.

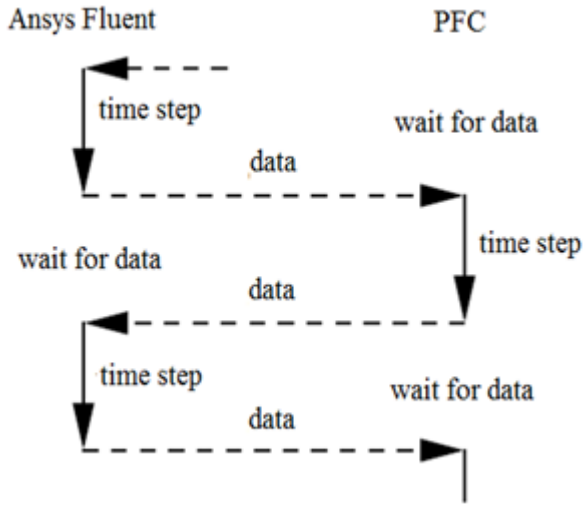

Figure 3.2 Adapter for coupled motion

In view of the ship motion in waves, ANSYS Fluent software is used to solve the 6-DOF motion. A CFD-DEM adapter is also developed to transfer data for the coupling between

ship response and cargo shift. At the first step, the angular velocity of the ship in waves is calculated using ANSYS Fluent software and is sent to the PFC2d. The corresponding moments on the ship due to cargo shift will be obtained. This external moment is transferred to the ANSYS Fluent, and so on, as seen in Figure 3.2. Based on the CFD-DEM adapter, cargo flow, ship response and sea state can be regarded in a holistic manner, which can offer unique opportunity to model the liquefaction problem, accounting for all pertinent parameters (ship, cargo, sea) and their interplay.

3.1.1 Contact Force and Stress

The force acting on each particle due to interaction with all its neighbouring particles is calculated based on the Rolling Resistance Linear Model in the PFC. It has advantages in describing the granular particles' motion and the angles of repose, which incorporates rolling torque to control the roll motion acting on the contacting particles.

The internal force and moment (F_c and M_c) act at the contact location in an equal and opposite sense on the two pieces. The relative displacement increment of each particle during a time step is given according to the force-displacement law, which consists of the following steps (for details see Appendix 5B):

1) Update the linear normal force and the linear shear force.
2) Update the dashpot normal force and the dashpot shear force.
3) Update the rolling resistance moment.

$$F_c = F^l + F^d \quad M_c = M_r \tag{3.1}$$

F^l: the linear force

F^d: the dashpot force

M_r: the rolling resistance moment

The dynamic stress of each particle is defined and calculated during shaking. For granular assemblies in a dynamic regime, a definition of a mean stress tensor is more disputable. A consistent definition must involve not only contact forces between particles, but also

inertia effects of grains subjected to dynamic effects (Fortin, 2003). Stress is defined as follows (François Nicot, 2013):

$$\langle\sigma_{ij}\rangle = \frac{1}{V}\sum_{c=1}^{N_c} f_i^c l_j^c + \frac{1}{3V}\sum_{p\in V}\left(\varepsilon_{ijk}M_k^p\right) + \frac{1}{3V}\sum_{p\in V} J_p\left((\Omega^p)^2\delta_{ij} - \Omega_i^p\Omega_j^p\right) \quad (3.2)$$

V: the representative elementary volume (REV)

f_i^c: the contact reaction force

l_j^c: the branch vector joining the centre of the particles in contact

ε_{ijk}: the Levi-Civita symbol

M_k^p: the moment imbalance for particle 'p'

J_p: the moment of inertia for particle 'p'

Ω^p: the angular velocity for particle 'p'

The equation above is the general expression of the average Cauchy stress tensor within a particle assembly of spheres, including dynamic effects related to both particle spin velocity and acceleration. Particles are assumed to be spheres, the centres of which are assigned to belong to the same plane. In two-dimensional conditions, $\bar{M}^p = M^p\bar{z}$ and $\bar{\Omega}^p = \Omega^p\bar{z}$ where $\bar{z}$ is the unit vector normal to the plane considered. Thus, $\Omega_i^p = 0$ for i=1, 2. Moreover, it is worth noting that the quantity $J_p(\Omega^p)^2/2$ represents the spin kinetic energy K_s^p of the particle 'p'. Thus, equation above gives, for $\mathrm{i,j} \in \{1,2\}$:

$$\langle\sigma_{ij}\rangle = \frac{1}{V}\sum_{c=1}^{N_c} f_i^c l_j^c + \frac{1}{3V}\sum_{p\in V}\left(M^p\varepsilon_{ij3} + 2K_s^p\delta_{ij}\right) \quad (3.3)$$

3.1.2 Elastic-plastic Strain

According to the dynamic stress calculated, the elastic-plastic strain of each particle can be obtained based on UBCSAND model (Ju, 2016). The elastic behavior, which occurs within the yield surface, is controlled by two parameters expressed in terms of the elastic bulk modulus K_B^e and the elastic shear modulus k_G^e as shown below:

$$K_B^e = k_B^e P_A\left(\frac{p'}{P_A}\right)^{me} \quad (3.4)$$

$$K_G^e = k_G^e P_A (\frac{p'}{P_A})^{ne} \quad (3.5)$$

p': the mean effective stress

P_A: the reference stress (usually equal to 100kPa)

k_B^e: the bulk modulus numbers

k_G^e: the shear modulus numbers

me: the elastic exponent which define the rate dependency of stiffness

ne: the elastic exponent which define the rate dependency of stiffness

The plastic behavior which occurs outside the yield surface is controlled by the hardening rule as reformulated by Tsegaye (2011), given as:

$$dsin\phi_{mob} = 1.5K_G^p \left(\frac{p}{P_A}\right)^{np} \frac{P_A}{P_m} (1 - \frac{\sin\phi_{mob}}{\sin\phi_{peak}} R_f)^2 d\lambda \quad (3.6)$$

$d\lambda$: the plastic strain increment multiplier

np: the plastic shear modulus exponent

ϕ_{mob}: the mobilized friction angle, which is defined by the stress ratio

ϕ_{peak}: the peak friction angle

R_f: the failure ratio n_f/n_{ult}, ranging from 0.5 to 1.0

The critical yield surface (Alexandros & Vahid, 2013) could be defined to determine the elastic strain or plastic strain of each particle:

$$f_m = \frac{\sigma'_{max} - \sigma'_{min}}{2} - (\frac{\sigma'_{max} + \sigma'_{min}}{2} + c' cot\phi'_p) sin\phi_{mob} \quad (3.7)$$

σ'_{max}: the maximum principal stresses

σ'_{min}: the minimum principal stresses

c': the cohesion of the soil

ϕ'_p: the peak friction angle of the soil

ϕ_{mob}: the mobilized friction angle during hardening

3.1.3 Soil Water Characteristic Curve

With the elastic-plastic strain of each particle, the development of the degree of saturation can be updated. With an increasing degree of saturation, the contact properties (friction coefficient) change. According to the experimental data, the corresponding friction coefficient will be set on the contact pieces (Chapter 5). Since (ship) cargo liquefaction will go through a longer-term process during carriage, the pore water pressure can be calculated according to the Soil Water Characteristic Curve (SWCC), which relates to the water content or degree of saturation to pore water pressure. When conducting the laboratory experiments, the pore water pressure can be tested by the pressure sensor to validate the model.

SWCC is the basis for estimating the dynamic analysis of unsaturated soils. The most common model to describe the hydraulic behavior of unsaturated soils is the model of Van Genuchten (1980) relationship. Van Genuchten function is a three-parameter equation and relates the saturation to the suction pore pressure head $\emptyset_p$ (see Figure 3.3):

$$\mathrm{S}(\phi_p) = S_{res} + (S_{sat} - S_{res})[1 + (g_a|\phi_p|)^{g_n}]^{g_c} \tag{3.8}$$

$$\phi_p = -p_w/(\rho_w * g) \tag{3.9}$$

S_{res}: the residual saturation which describes the part of water that remains in soil even at high suction heads

S_{sat}: the saturation when the pores are filled with water

In general, the pores at saturated conditions the pores cannot be completely filled with water and some air bubbles can be present in water, therefore, in this case, S_{sat} will be less than 1. g_a, g_n and g_c are empirical parameters.

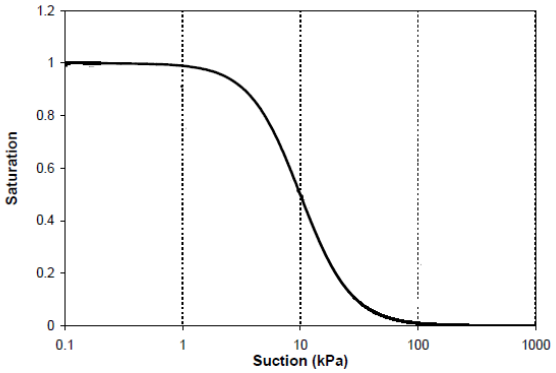

Figure 3.3 Van Genuchten SWCC curves, g_a=1.0, g_n=2.0 and g_c=-1.0 (Galavi, 2010)

3.2 Ship Response

Ship stability due to cargo shift is a coupled phenomenon which needs to address the cargo shift and ship stability in waves in a holistic manner. Therefore, an adapter is developed to combine PFC software with ANSYS Fluent software, which allows for the transferring of data during the coupled calculations without any changes in the source of the simulation code. Detailed information about the adapter is described in Chapter 7. Based on ANSYS Fluent commercial software, the Reynolds-averaged Navier-Stokes equations (RANS) with SST $k-\omega$ model is solved to study the ship response in waves. The VOF algorithm is applied to capture free surface. The governing equations can be written as follows (ANSYS FLUENT Theory Guide 2013):

Continuity equation:

$$\nabla \cdot u = 0 \tag{3.10}$$

∇: Hamiltonian or gradient operator

u: Velocity vector

Momentum equation:

$$\frac{\partial}{\partial_t}(\rho u) + \nabla \cdot (\rho u \otimes u) = \rho g - \nabla P + \nabla \cdot (\mu \nabla \otimes u) \tag{3.11}$$

g: Gravity vector

P: Pressure

μ: Viscosity

SST $k-\omega$ Turbulence model:

$$\frac{\partial}{\partial t}(\rho k)+\frac{\partial}{\partial x_i}(\rho k u_i)=\frac{\partial}{\partial x_j}\left(\Gamma_k \frac{\partial k}{\partial x_j}\right)+G_k-Y_k+S_k \tag{3.12}$$

$$\frac{\partial}{\partial t}(\rho \omega)+\frac{\partial}{\partial x_i}(\rho \omega u_i)=\frac{\partial}{\partial x_j}\left(\Gamma_\omega \frac{\partial \omega}{\partial x_j}\right)+G_\omega-Y_\omega+D_\omega+S_\omega \tag{3.13}$$

G_k: the production of turbulence kinetic energy

G_ω: the generation of ω

Γ_k: the effective diffusivity of k

Γ_ω: the effective diffusivity of ω

Y_k: the dissipation of k due to turbulence

Y_ω: the dissipation of ω due to turbulence

D_ω: the cross-diffusion term

S_k and S_ω: the user-defined source terms

VOF equation:

By solving momentum equations and tracking the volume fraction of each fluid throughout the domain, VOF model is used to track the variation of volume transferring between air and fluid. It can be defined as:

a_q =0, the cell is empty of the qth fluid

a_q=1, the cell is full of the qth fluid

$0 < a_q < 1$, the cell contains the between the qth fluid and one or more other fluids.

Where a_q is the volume fraction of q^{th} fluid.

By solving a continuity equation for the volume fraction of one or more phases, the interface between phases can be tracked. For q^{th} phase, the equation is defined as:

$$\frac{1}{\rho_q}\left[\frac{\partial}{\partial t}\left(a_q\rho_q\right)+\nabla\left(a_q\rho_q\vec{v}_q\right)=S_{a_q}+\sum_{p=1}^{n}\left(\dot{m}_{pq}-\dot{m}_{qp}\right)\right] \quad (3.14)$$

In this function, $\dot{m}_{pq}$ and $\dot{m}_{qp}$ are the mass transfer from phase p to phase q and from phase q to phase p respectively. S_{a_q} is zero.

$$\sum_{q=1}^{n} a_q = 1 \quad (3.15)$$

3.3 Coupled Model Input Parameters

The principal framework will address the ship cargo liquefaction problem based on the DEM combined with the CFD method. The coupled model input parameters include three parts: deformation parameters, hydraulic parameters, and contact model parameters, as shown in

Table **3.1**. According to contact force and moment, the particle movement will be updated according to Newton's second law. During the same time step, in calculating the stress on the particles, the strain of particles will be identified based on the UBCSAND model. With the development of the degree of saturation, the pore water pressure and contact model parameter, particularly the friction coefficient at various moisture contents (degree of saturation), will be updated. Based on a CFD-DEM adapter, cargo displacement, ship response and sea state can be regarded in a holistic manner which can offer the unique capability to model the liquefaction problem.

Table 3.1 Coupled Model Input Parameters

	Symbol	Description
Deformation parameters	$\varphi_p(\circ)$	Peak friction angle
	$\varphi_{cv}(\circ)$	Constant volume friction angle
	k_B^e	Elastic bulk modulus
	k_G^e	Elastic shear modulus
	k_G^p	Plastic shear modulus
	me, ne	Elastic bulk, shear modulus index
	np	Plastic shear modulus index
	R_f	Failure ratio
	P_A	Atmospheric pressure
Hydraulic parameters	g_a, g_n, g_c	Empirical parameters
	n_{sat}	Saturation when the pores are filled with water
	n_{res}	Residual saturation when the part of water remains at high suction heads
	MC	Moisture content
	Poro_initial	Initial porosity
Contact model parameters	*emod*	effective modulus
	kratio	stiffness ratio
	fric	friction coefficient
	rfic	rolling resistance coefficient
	dp_nratio	normal critical damping ratio
	dp_sratio	shear critical damping ratio
	dpmod	dashpot mode

Chapter 4 CFD Applications to Liquefaction

Most of the research on earthquake liquefaction is based on the CFD technique, mostly in terms of the Finite Element Method (FEM). PLAXIS 2D is a powerful and user-friendly finite element package for analysis of deformation and stability in geotechnical engineering and rock mechanics. Applications range from excavations, embankment, and foundations to tunnelling, mining and reservoir geomechanics. The UBCSAND liquefaction model (Beaty & Byrne, 1998) is one of the most useful models available in the PLAXIS software, and can determine liquefaction potentials. Numerical analysis based on the UBCSAND model in this chapter will provide essential reference and conclusions for the following chapters (including advantages and limitations). Meanwhile, the UBCSAND model will be embedded into the DEM in Chapters 5 and 6 to identify deformation and discrete characteristic of the granular material. Furthermore, for the reason that liquefied cargo behaves like a non-Newtonian fluid, a Herschel-Bulkley non-Newtonian model is selected to investigate the rolling response of a 2D container in regular waves on account of cargo shift based on the ANSYS Fluent code.

4.1 Assessment of Cargo Liquefaction

Tri-axial shear test (TxC), direct simple shear test (DSS) and cyclic shear test are common methods to measure the mechanical properties of many deformable solids, especially soil (e.g., sand, clay) and rock, and other granular materials. Therefore, TxC, DSS and cyclic shear test are conducted to validate UBCSAND model.

4.1.1 Monotonic Loading

The input parameters for modelling the tri-axial compression test (TxC) and the direct simple shear test (DSS) on loose Syncrude sand are defined in Table 4.1. Stress-strain path response derived from UBCSAND model shows a good agreement with the experimental

data provided by Puebla & Byrne & Philips (1997) as shown in Figure 4.1.

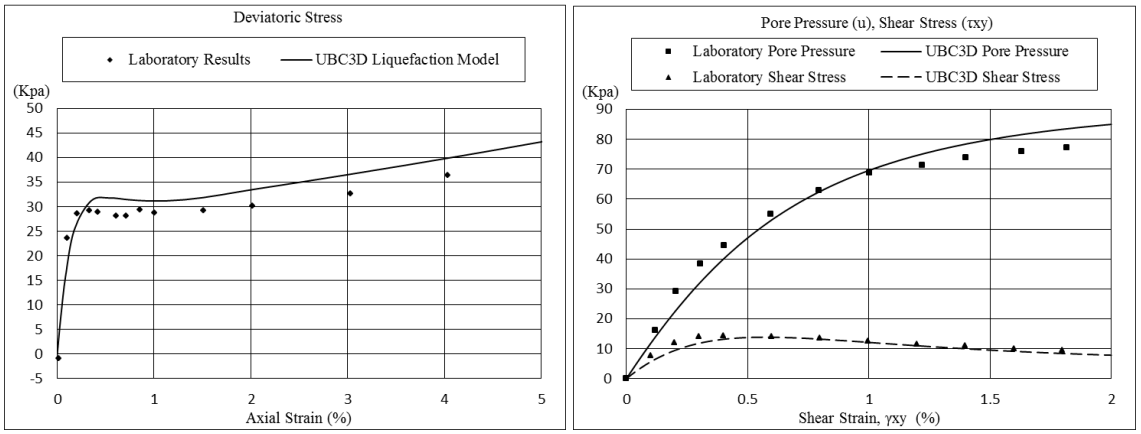

(a) Undrained tri-axial compression (b) Undrained simple shearing

Figure 4.1 Monotonic loading (TxC, DSS)

Table 4.1 UBC3D input parameters for all the validation tests

Parameter	Syncrude S.(TxC, DSS)	Fraser S. (Cyclic DSS)	Cargo(FEM)
$\varphi_p(\circ)$	33.7	33.8	31.2
$\varphi_{cv}(\circ)$	33	33	34.6
k_B^e	300	607	720
k_G^e	300	867	1031
$K_G^p(TxC)$	310	-	
$K_G^p(DSS)$	98.3	266	700
$me = ne$	0.5	0.5	0.5
np	0.5	0.4	0.4
R_f	0.95	0.81	0.74
$N1(60)$	8	8	13
fac_{hard}	1	1	0.45
fac_{post}	0	0.6	0.01

4.1.2 Cyclic Loading

The behavior of loose Fraser sand under cyclic direct simple shear is modelled and the numerical results are compared with experimental data published by Sriskandakumar (2004). The relative density (RD) of the tested sand is 40%. In Figure 4.2, Figure 4.3 and Figure 4.4, the evolution of stress-strain path response is presented. The applied CSR equals 0.08, 0.1 and 0.12 respectively. The vertically applied stress is 100kPa in all cases. The K0 factor is assumed to be 1 for simplification. On the basis of the comparison with experimental data, UBCSAND liquefaction model could address the liquefaction phenomena effectively, including the evolution of pore pressure ratio and the triggering point of liquefaction.

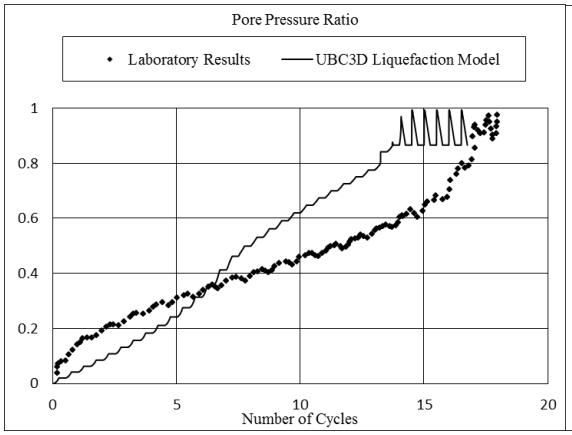

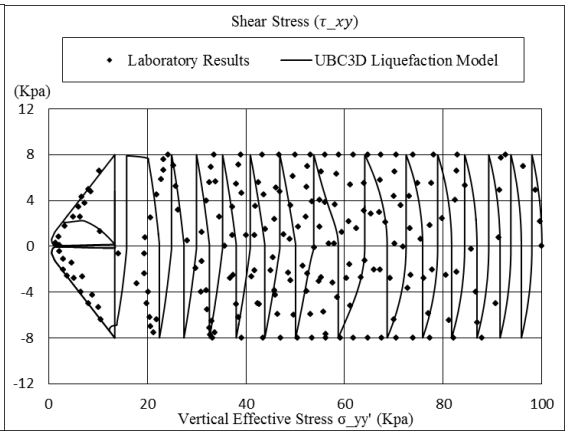

(a) Pore pressure ratio (b) Vertical effective stress-shear stress curve

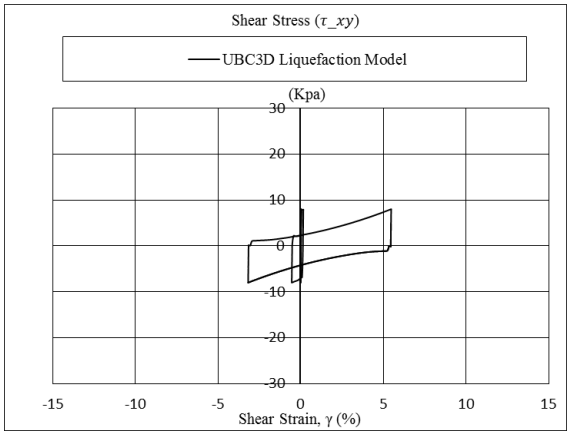

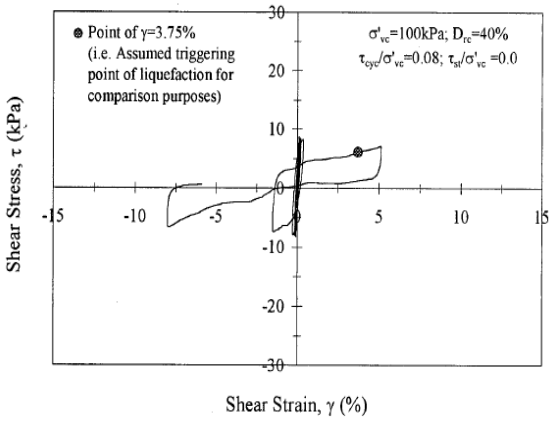

(c) Stress-strain curve (Left: simulation results; Right: experimental data)

Figure 4.2 Cyclic DSS stress controlled (RD=0.4 CSR=0.08 =100kpa)

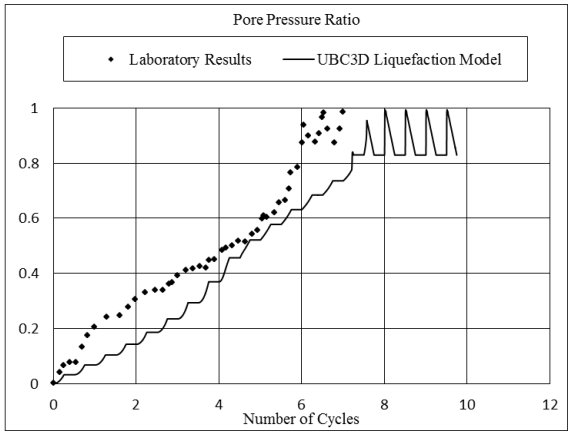

(a) Pore pressure ratio

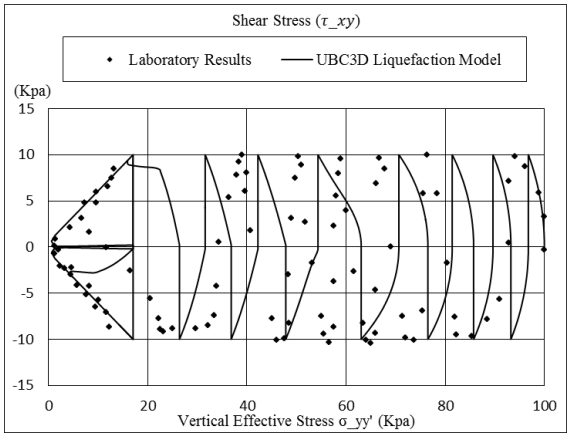

(b) Vertical effective stress-shear stress curve

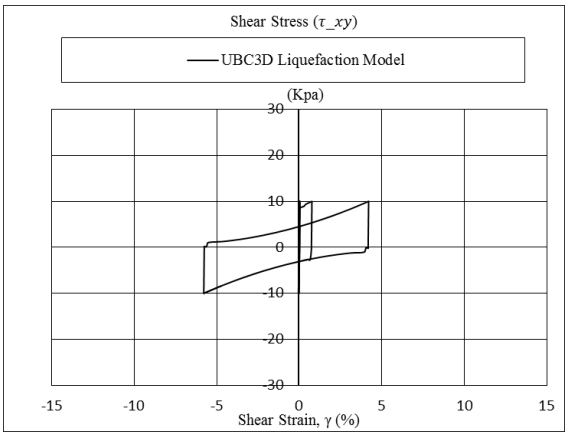

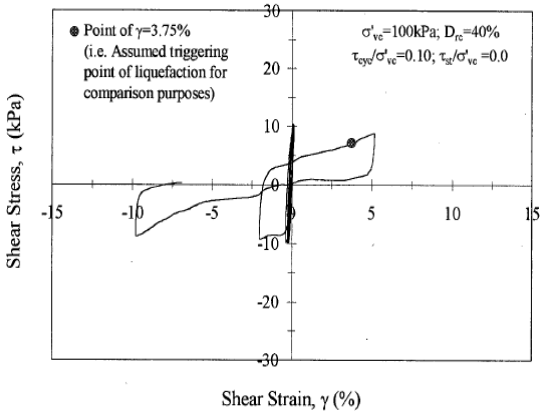

(c) Stress-strain curve (Left: simulation results; Right: experimental data)

Figure 4.3 Cyclic DSS stress controlled (RD=0.4 CSR=0.1 =100kpa)

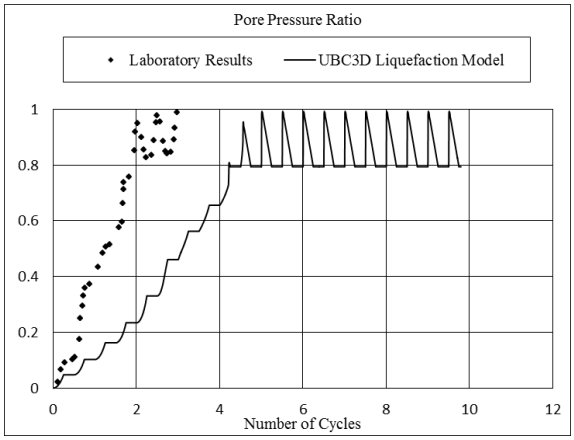

(a) Pore pressure ratio

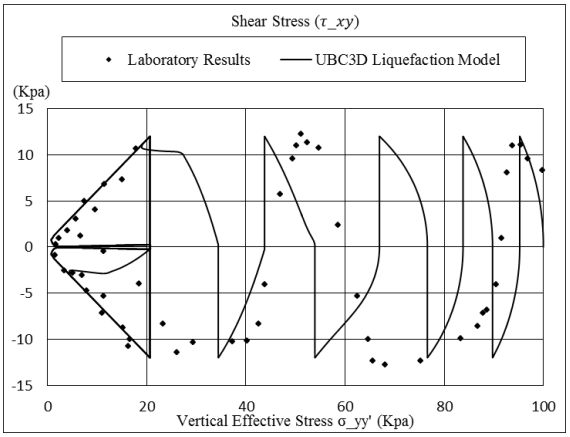

(b) Vertical effective stress-shear stress curve

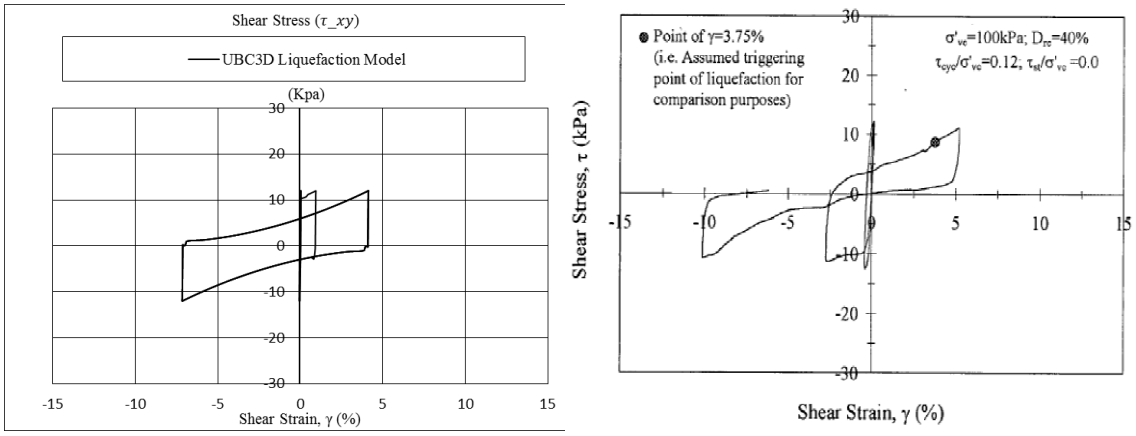

(c) Stress-strain curve (Left: simulation results; Right: experimental data)

Figure 4.4 Cyclic DSS stress controlled (RD=0.4 CSR=0.12 =100kpa)

4.1.3 Definition of Liquefaction Point for Particles

In soil mechanics, a state of 'soil liquefaction' occurs when the effective stress of soil is reduced to essentially zero, which corresponds to a complete loss of shear strength. This may be initiated by either monotonic loading or cyclic loading, usually occurring in earthquake shaking or other sudden changes in stress conditions, causing it to behave like a liquid. However, for cargo liquefaction, the external load on the cargoes during carriage is primarily in the form of low-frequency. Effective stress of particles may not reduce to zero under the external load during the voyage. What is more concerning is that cargo mobility may cause the loss of ship stability. In view of the mechanism of cargo liquefaction, presented in Chapter 1, cargo containing some moisture will experience compaction to a degree during the voyage, causing the friction between particles weakening, which results in cargo movement. Therefore, the definition of the liquefaction point for a particle needs to be evaluated on a case-by-case basis.

As known in soil mechanics, the Soil Water Characteristic Curve (SWCC) is the basis for estimating the dynamic analysis of particles. The SWCC relates water content or degree of saturation to matrix suction of a particle. A representative SWCC is shown in Figure 4.5, which indicates that SWCC varies from a wide variety of iron ore fines. In brief, SWCC reflects the water holding ability of the granular material. Especially for the cargo

with high geothites content, the cargo has high “dehydration ability” (TWG report, 2013). If the cargo (unsaturated state) reaches the limit of holding water under the external load, which means the saturated state, water will be progressively drained from the interspace between particles. This consequence will decrease the shear strength and cause cargo movement. Therefore, in this research, if the degree of saturation of a particle reaches 100% or suction is equal to 0kPa (saturated state) according to the SWCC, the particle liquefies.

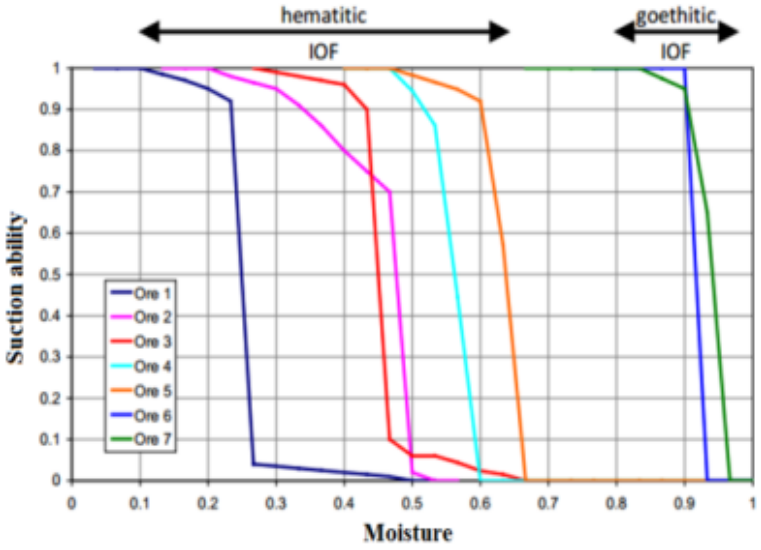

Figure 4.5 Soil-water characteristic curves

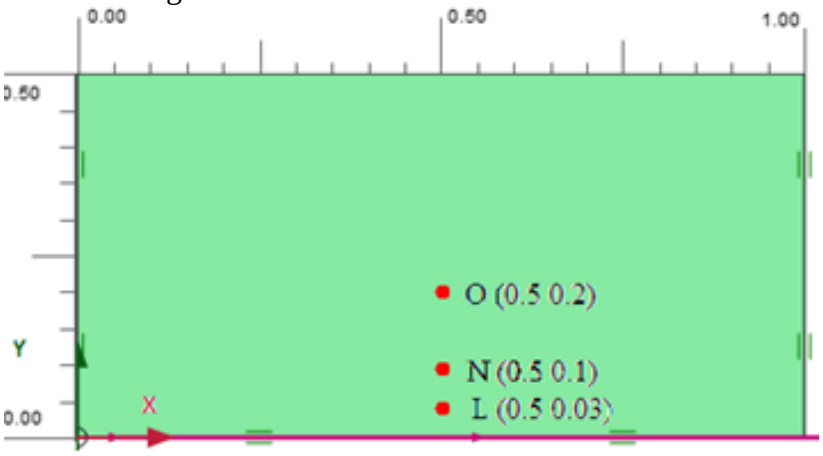

Figure 4.6 Centrifuge test model

4.1.4 Centrifuge Test

The centrifuge test on the free field response is conducted based on the UBCSAND model

and a parametric investigation is undertaken to identify the degree of saturation parameter that triggers cargo liquefaction. The geometry of layer is presented in Figure 4.6. Locations L, N, O are monitored through the test. The initial degree of saturation is supposed to be uniform and varies from S=99.0%, 97.0% and 94.0%. The initial stress is created by the gravity action. The boundary conditions are defined as: at the base of layer, where the vertical displacement is blocked, and when the input energy is sinusoidal horizontal acceleration with an amplitude of $0.02\mathrm{m}/s^2$and frequency of 2HZ. At the lateral boundaries, the horizontal displacement is blocked. The model parameters are listed in Table 4.1.

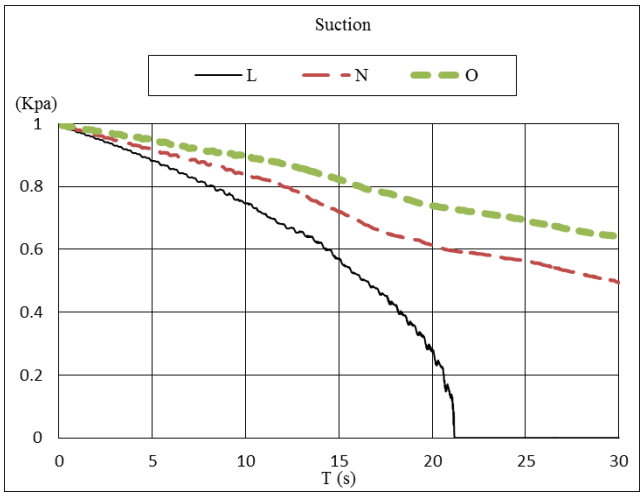

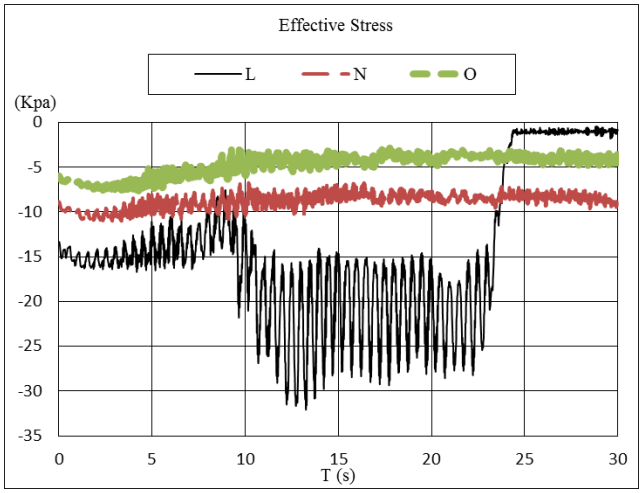

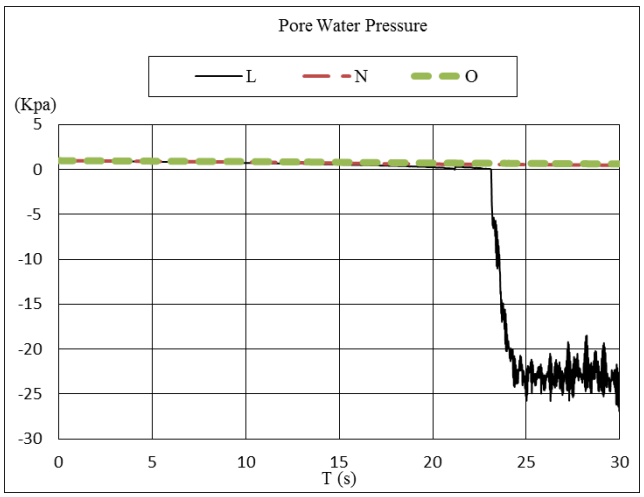

(a) Degree of saturation=94%

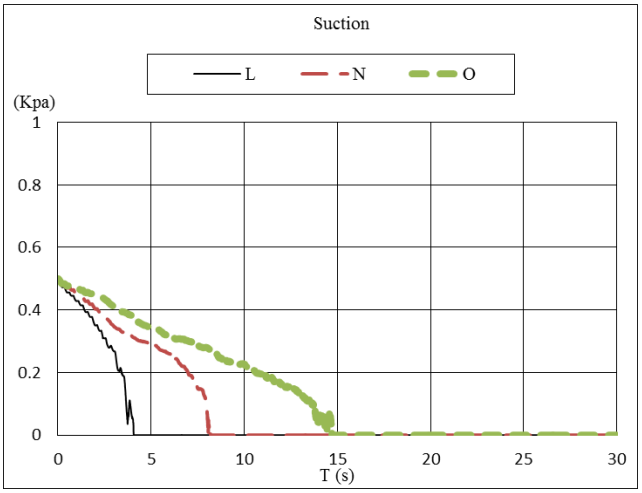

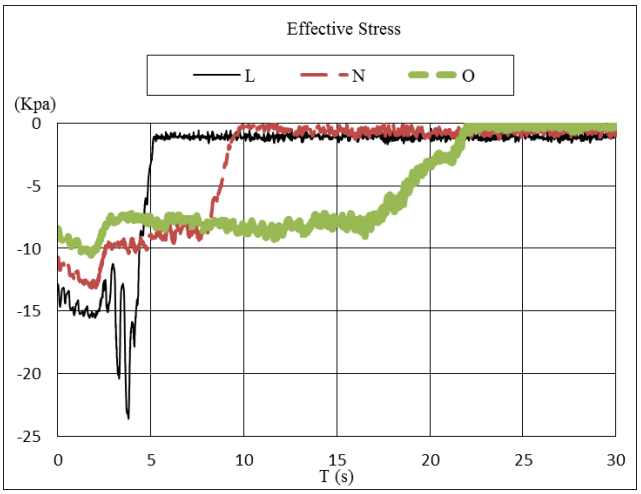

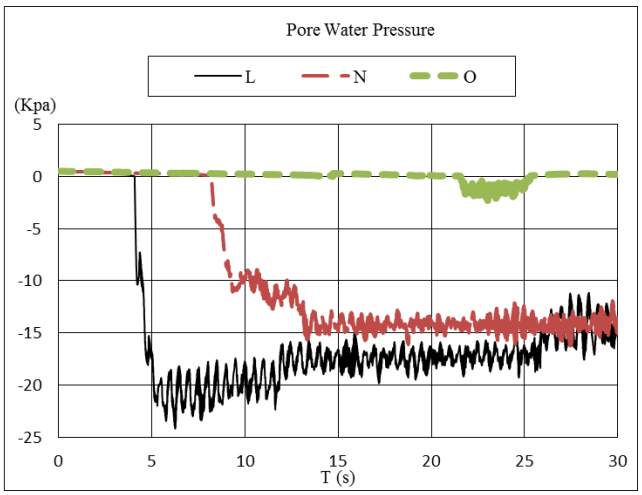

(b) Degree of saturation=97.0%

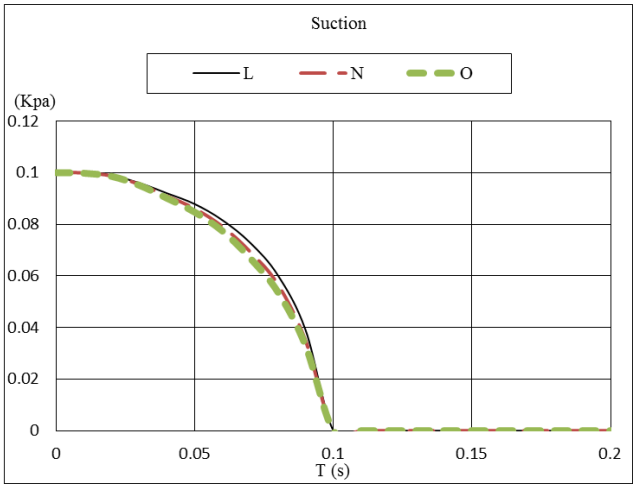

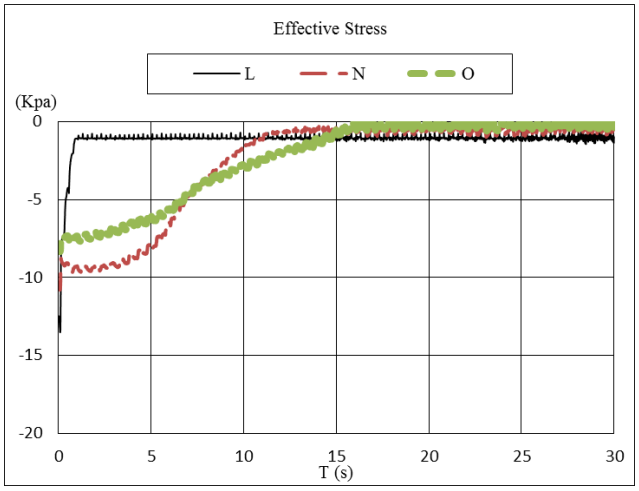

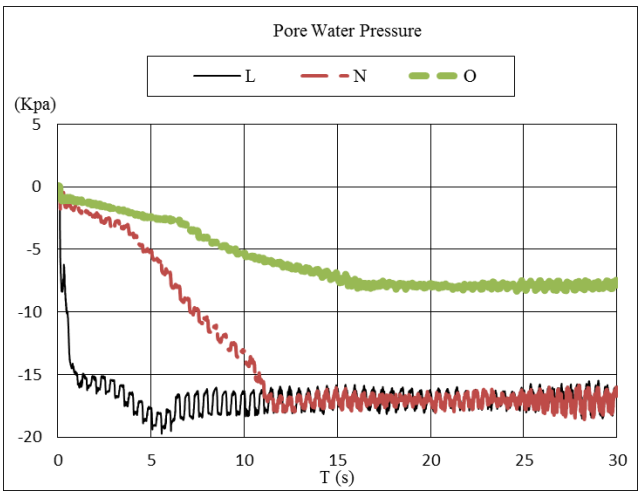

(c) Degree of saturation =99.0%

Figure 4.7 Evolution of suction, effective stress and pore water pressure during centrifuge test

From Figure 4.7, it can be seen that variation of the initial degree of saturation is very sensitive on the development of matric suction, effective stress and pore water pressure. When the initial degree of saturation is less than 94%, the onset of liquefaction at point L could be delayed to 23s, in comparison with an initial degree of saturation of 97% and 99%. Furthermore, the sample goes through compaction by the centrifuge wave from the unsaturated state (suction>0) to saturated state (suction=0). From the saturated state onwards, the pore water pressure increases rapidly and effective stress decreases to zero, which means liquefaction as defined in soil mechanics.

4.1.5 Shaking Table Test

Shaking table tests are conducted for comparison with the centrifuge test to discuss the difference in liquefaction point as defined in this thesis with the definition in soil mechanics. As discussed above, centrifuge wave is high-frequency, while the wave generated by sea state is low-frequency. Therefore, based on the new definition of liquefaction point presented in section 4.1.3, sway motion of a 2D container with varying amplitude, frequency and initial degree of saturation of granular materials is simulated by shaking the table to investigate the onset of liquefaction. The geometry of layer is shown in Figure 4.8. Locations M, L, K, P, O, and N are monitored through the test. The initial

degree of saturation is supposedly uniform and varies from 99%, 95.16%, and 92.38%. The frequency varies from 0.25HZ, 0.35HZ, and 0.5HZ. The amplitude varies from 0.02m, 0.04m and 0.06m. The boundary conditions are defined as: at the base of the layer, when the vertical displacement is blocked, and when the input energy is at the sinusoidal horizontal displacement condition. At the lateral boundaries, the horizontal displacement is free and has the same motion as the base of the container. The initial stress due to gravity is shown in Figure 4.8.

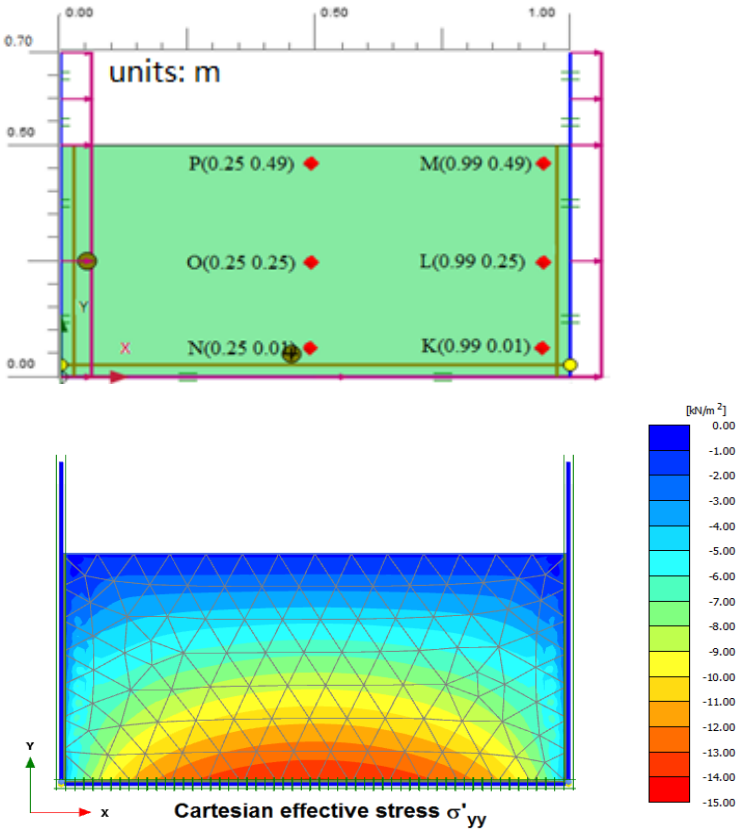

Figure 4.8 Shaking table test model (2D). (up: monitor points, down: the effective stress contour after gravity action)

From Figure 4.9, given the initial condition of amplitude 0.04m, frequency 0.25HZ and degree of saturation 95.16%, it can be observed that the granular materials close to locations L, O and K are at the threshold of liquefaction due to severe compaction. Locations M and P show dilation, N has high effective stress and is hence difficult to liquefy. Emphasis could be placed on the middle column of location O. It can be concluded

that the higher initial degree of saturation of material, frequency, and amplitude of energy input, the less the liquefaction resistance. From Figures 4.9(b) to (d), the amplitude, frequency of energy input and especially initial degree of saturation of the granular material presents a significant impact on liquefaction resistance.

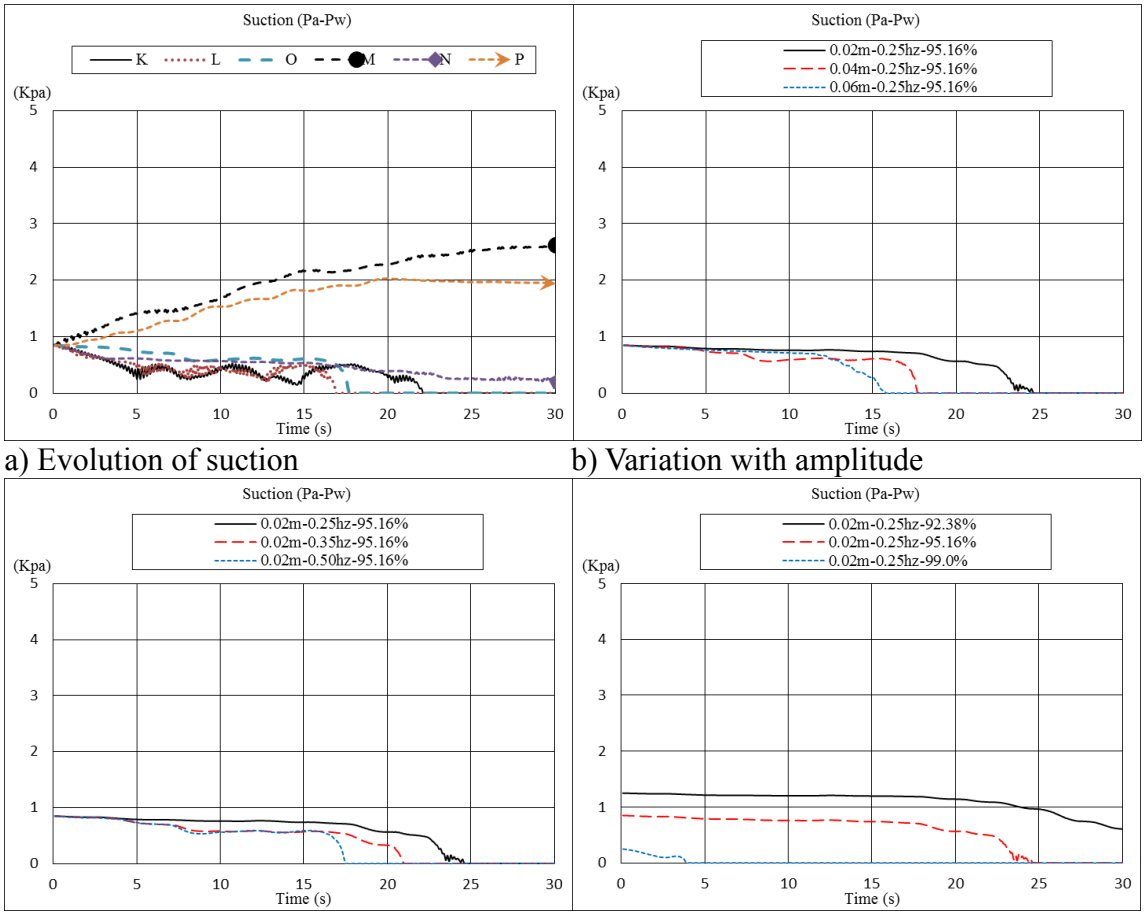

a) Evolution of suction b) Variation with amplitude

(c) Variation with frequency (d) Variation with degree of saturation

Figure 4.9 Shaking table test

4.2 Liquefied Cargoes (Non-Newtonian Fluid)

Liquefied cargoes behave like non-Newtonian fluid from observation (Ju, 2013; Zhang, 2016). The liquefied cargoes will flow to one side but not flow back with a roll. This phenomenon is similar to the flow properties of a non-Newtonian fluid. In this section, the Herschel-Bulkley fluid is selected as the non-Newtonian fluid to investigate the rolling response of a 2D container in regular waves on account of cargo shift based on the ANSYS

Fluent code. The constitutive equation of the non-Newtonian fluid is read by the UDF of ANASYS Fluent software. Coupled motion of the 2D rectangular structure filled partly with liquefied cargoes in waves is conducted. Basic validations are presented in Appendix 6.

A 2D rectangular hold (0.2m*0.13m), with moment of inertia of the actual mass of the structure at 0.236 $Kg.m^2$, is installed inside the rectangular structure (0.3m*0.3m) to simulate the ship response on account of sloshing flows in waves (see Figure 4.10). The structure floated at a draft that equals one-sixth of its height. It is filled with water and a non-Newtonian fluid with a filling area of 0.2m*0.045m, separately. The properties of the non-Newtonian fluid are defined as: flow index is 0.479, yield pressure is 30kPa and different density is 1000Kg/m3, 1250kg/m3, and 1500Kg/m3, separately. The same mass of the various cases is applied on the rectangular structure. The wave parameters are shown in Table 4.2. The gravity centre is set at the location of (7m, 0m). The coupled interaction between the non-Newtonian fluid sloshing and the response of the structure in the regular wave is discussed by examining the roll angle of the structure at the natural frequency. Roll motion in waves of the rectangular structure has been evaluated using experimental data in section 7.2.1.

Table 4.2 Parameters of linear wave

T (s)	ω (rad/s)	λ (m)	H (m)	kA
0.93	6.76	1.35	0.027	0.0628

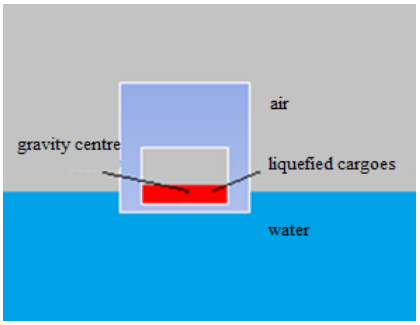

Figure 4.10 Sketch of calculation domain on account of sloshing flow for coupled motion

Figure 4.11 shows the free surface of the water and liquefied cargoes at time 10.8s, 11.0s, 11.2s, and 11.4s. Due to the properties of the non-Newtonian fluid, the fluid shows great inertia. If the fluid shifts to one side, the gravity centre will be changed due to the large weight of the fluid. In some cases, the moment induced by the fluid sloshing may be significant and cause a large contribution to the loss of ship stability. From Figure 4.12, the maximum roll angle of the container filled with high-density fluid gradually decreases. This means that the non-Newtonian fluid restrains the roll motion greatly in regular waves. This can be explained by the properties of the non-Newtonian fluid. If the shear stress is lower than the yield pressure, the fluid cannot flow. Also, there might be the possibility that the sloshing flow is restricted by the movement of rectangular structure in this natural frequency. This possibility will be discussed in following research.

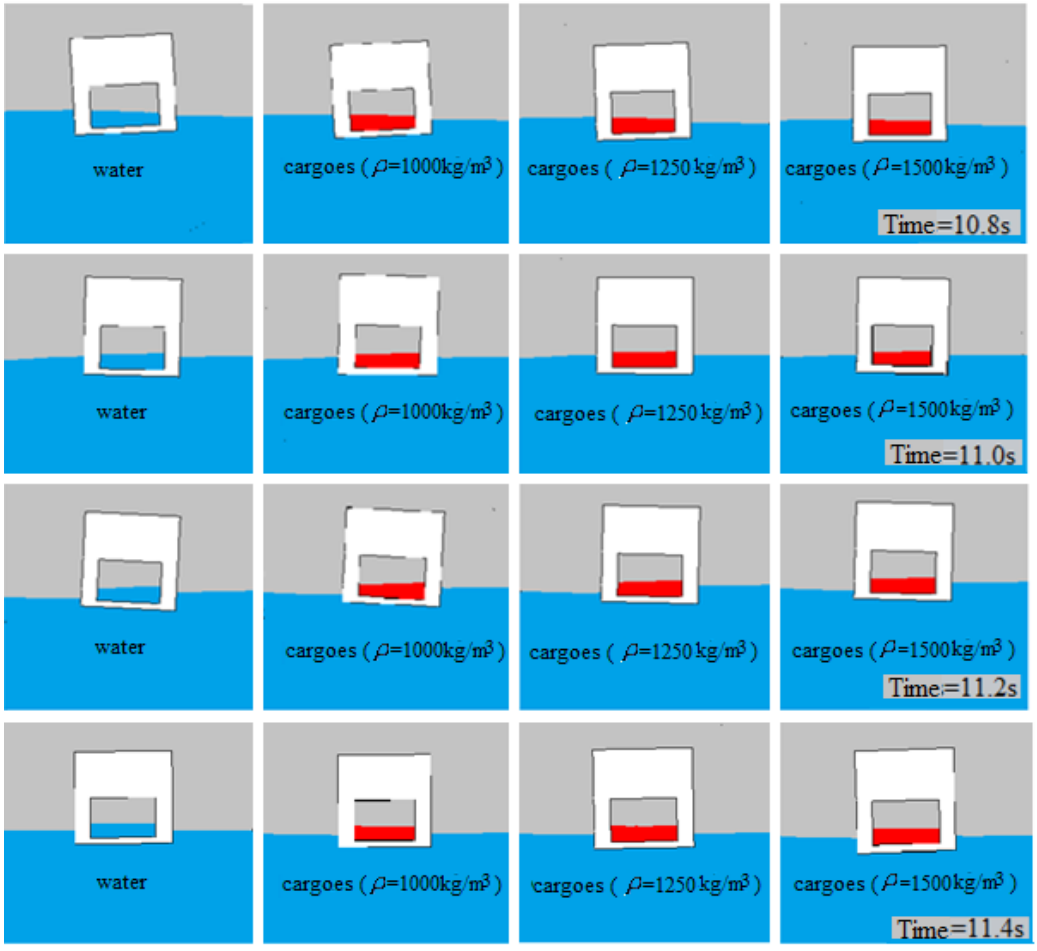

Figure 4.11 Contours of 2-D coupled motion in waves filled with water and non-Newtonian fluid (Time=10.8s, 11.0s, 11.2s and 11.4s)

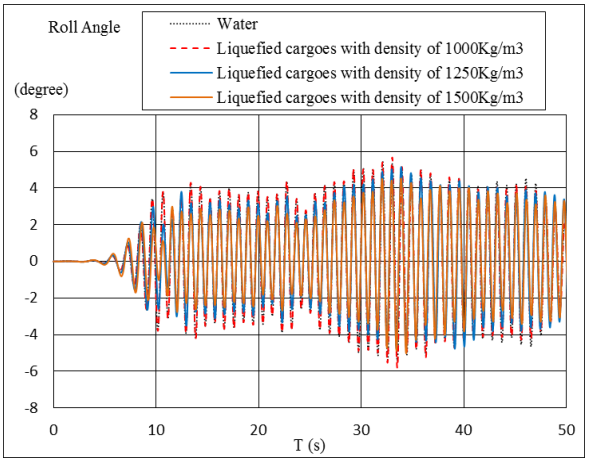

Figure 4.12 Time history of roll angle for coupled motion in waves filled with water and liquefied cargoes

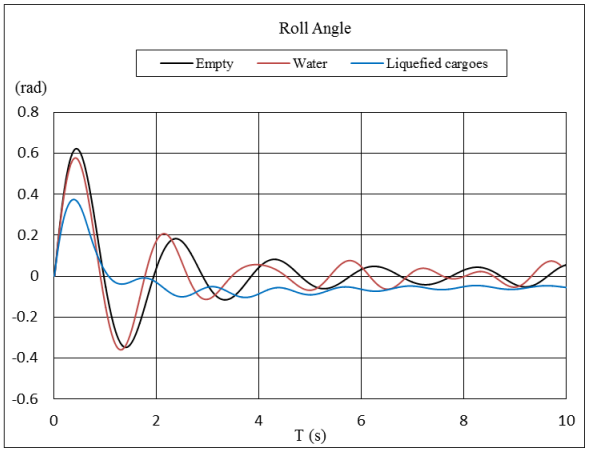

Figure 4.13 Time history of roll angle of the rectangular structure filled with air, water and non-Newtonian fluid for coupled motion under an instantaneous exciting force

Based on the discussions above, an instantaneous exciting angular velocity (1.5rad/s) is imposed on the structure to investigate the response of the structure due to sloshing flow. It can be seen in Figure 4.13 that when the container is empty, the roll angle gradually decreases to zero due to the damping effect; when the container is filled with water, the roll motion is affected by the water sloshing slightly; and when the container is filled by the non-Newtonian fluid, the shear stress of the fluid resists the yield pressure and the fluid begins to shift to one side, which changes the position of the center of gravity of the structure — causing a large heel. It can thus be concluded that instantaneous acceleration on the structure, for instance, irregular waves, may be the primary factor causing liquefied cargoes to shift.

4.3 Conclusions

In this chapter, research on cargo liquefaction based on traditional methods has been presented. First, Based on PLAXIS software, tests for monotonic loading and cyclic loading agree well with experimental data to validate the UBCSAND model and could be used to evaluate liquefaction potential. It is concluded that with an initial higher degree of saturation of cargoes, frequency, and amplitude of the external energy input, the cargo is less resistant to liquefaction. Among these three parameters, the only one that can be controlled is the degree of saturation. Therefore, reducing the initial degree of saturation of cargoes or the initial moisture content will enormously reduce the risk of liquefaction. Furthermore, from the coupling analysis of the rectangular structure response and sloshing flows of non-Newtonian fluid in waves based on ANSYS Fluent software, instantaneous acceleration of the structure, such as through irregular waves, may be the primary factor causing the liquefied cargoes to shift. The method used in this chapter can address the liquefaction phenomenon and ship response in waves to a large degree. However, CFD has some limitations in fully solving the loss of ship stability due to cargo shift:

1) the discrete characteristic of granular materials cannot be presented by the CFD method, especially for the interaction between cargo shift and ship response;
2) the angle of repose cannot be described by the CFD method, which is a significant character of granular materials;
3) the CFD method is unable to deal with the deformation problem of granular materials.

Therefore, in the next chapters, the CFD method combined with the DEM will be developed to tackle the limitations aforementioned. The framework of this new method is that cargo flow and cargo deformation will be determined by the DEM (PFC2d) and ship response in waves can be determined by the CFD (ANSYS Fluent). Finally, a CFD-DEM adapter will be developed to exchange necessary data to achieve a coupled calculation.

Chapter 5 DEM Application to Cargo Shift

While the CFD methods have some limitations in addressing cargo shift, as discussed in Chapter 4, the Discrete Element Method (DEM) offers some advantages. Particle Flow Code (PFC) is advanced multi-physics simulation software based on the DEM. The particles are rigid bodies using the soft contact approach, whereby the particles are allowed to overlap at contact points. Particles interact with each other at pair-wish contacts by means of an internal force and moment, which provides a dynamic solution to Newton's laws of motion. Rolling Resistance Linear Model in the PFC code incorporates the rolling torque to control roll motion, and the internal moment is incremented linearly with the accumulated relative rotation of the contacting pieces at the contact point, which can effectively shape the angles of repose commonly found in granular materials.

As moisture content increases, the cargo shows a muddy appearance progressively. When moisture content exceeds the TML, cargo may run the risk of liquefying, reducing ship stability and capsizing the ship. In this chapter, a static incline test is carried out to determine the flow characteristics at various moisture contents. The dynamic analysis is performed with respect to the fluctuation force on the rectangular structure, which identifies the modes of motion (frequency, amplitude, and moisture content) that interact with the container.

5.1 Moisture Content in Cargoes

Cargoes in nature contain certain moisture more or less. It is the moisture that leads the risk of liquefaction, although the moisture in the cargoes is not visibly wet in appearance. Unsaturated materials like soils are composed of three phases, including soil skeleton (solid), pore water (liquid) and pore are (gas). The air-water interface has a surface tension. In the unsaturated soil, the pore air pressure and pore water pressure are unequal and greater than the latter. The pressure difference (i.e., pore air pressure minus pore water

pressure) across the interface between air and water is called the matric suction. Matric suction is generally the key parameter describing the mechanical property of unsaturated soil. Matric suction is defined follows:

$S = u_a - u_w = \Delta P$

Where S depends on the curvature of the curved interface and surface tension.

The microstructure of three-phase unsaturated soils is schematically shown in Figure 5.1. Generally, when the matric suction decreases to nil, the unsaturated soil becomes the saturated soil according to the SWCC, which means that the pores are filled with water. On the basis of the definition of matric suction, unsaturated soil has a high holding water ability as the pore air pressure is greater than pore water pressure. When the suction decreases, the holding water ability of the soil skeleton decreases accordingly. In order to reflect the moisture in particles, many authors presented explicit capillary force functions, which have shown to be sufficiently accurate (Zhu et al., 2007). However, in PFC, the unsaturated state has not been developed. As discussed in Chapter 1, due to compaction owing to ship motion, the spaces between particles reduce resulting in the weakening of friction between particles. Therefore, we use the friction coefficient between the particles to represent the moisture content or degree of saturation. Section 5.2 will identify the friction coefficient of the moisture content between particles accordingly.

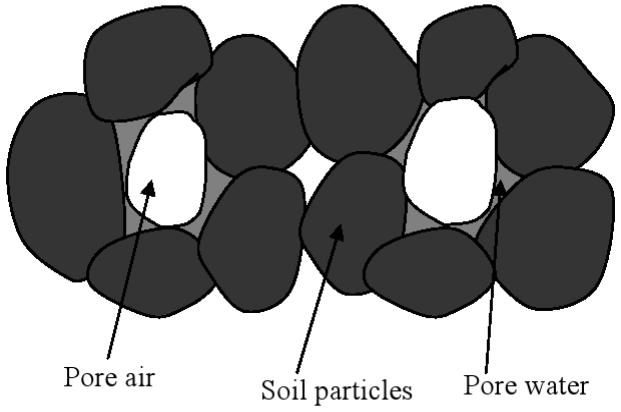

Figure 5.1 Microstructure of unsaturated soils (Liu, 2009)

5.2 Incline Test

A static incline test is carried out to identify the contact properties at various Moisture Contents (MCs). The behavior of the samples stored in the container is observed by inclining the container statically up to the maximum inclined angle of 50 degrees. This is compared with the experimental data from ClassNK (2011) to evaluate whether the DEM can effectively simulate the particle flow at different moisture contents.

5.2.1 Geometry and Setup

The 2D rectangular container (50cm*50cm*50cm) that was used for the static incline test was inclined by a crane, in which the sample was stowed with various moisture contents (ClassNK, 2011). Figure 5.2 shows the appearance of the static inclining test equipment and the initial state of the granular particles in PFC code.

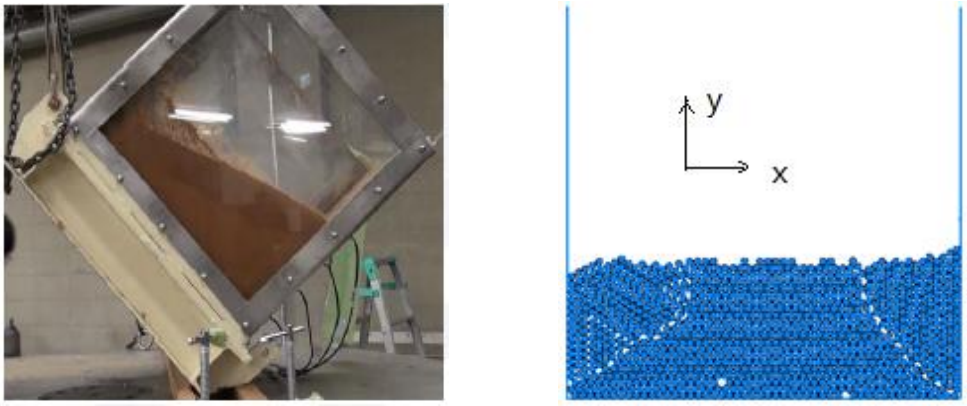

Figure 5.2 Static inclining test equipment (ClassNK, 2011) and initial state of granular particles

5.2.2 Results and Analysis

To address the coupled motion between ship response and cargo shift, flow characteristics of the cargo are initially identified. During the carriage of cargoes, the degree of saturation will increased, which weakens the friction between particles due to compaction. Therefore, cargo flow and ensuing fluctuation force on a container are determined by updating the friction coefficient in accordance with the relevant degree of saturation. The friction

coefficient varying with the degree of saturation can be obtained by experimental methods. Figure 5.3 shows the appearance of the nickel ore samples statically inclined at 50 degrees (Class NK, 2011). It is observed that the sample behavior becomes gradually near to a liquid one as moisture content increases. The rolling test results reflect this as well. To evaluate the application of the DEM on the granular materials, a static incline test is simulated, which shows a good agreement with the experimental data from Figure 5.4. Therefore, flow characteristics of the cargo at various moisture contents can be described by relevant friction coefficients and rolling friction coefficients derived from the Rolling Resistance Linear Model in PFC software. Fitting equations can be obtained to relate the degree of saturation (moisture content) to the friction coefficient, which could then be implemented into the DEM liquefaction model in Chapter 6. Therefore, cargo deformation and cargo flow can be considered simultaneously. However, the granular particle in PFC software is different from the material of nickel ore. Thus, more experiments should be done to validate this method.

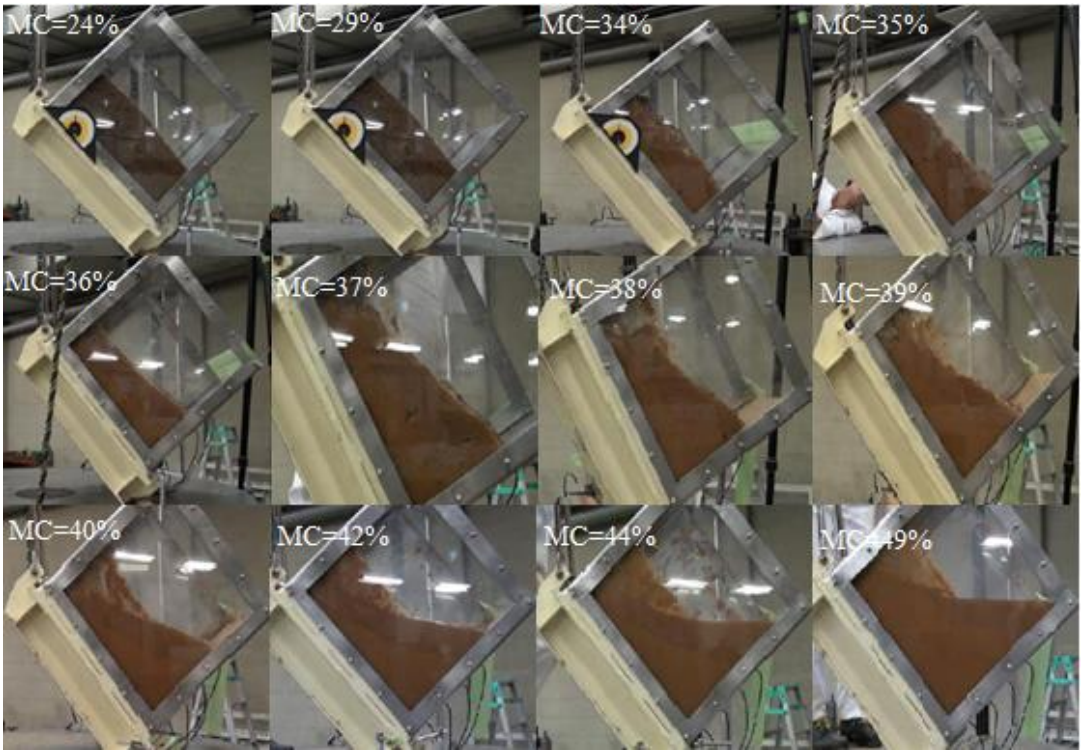

Figure 5.3 Appearance of Nickel Ore sample inclined at 50 °(Indonesian product,) (ClassNK, 2011)

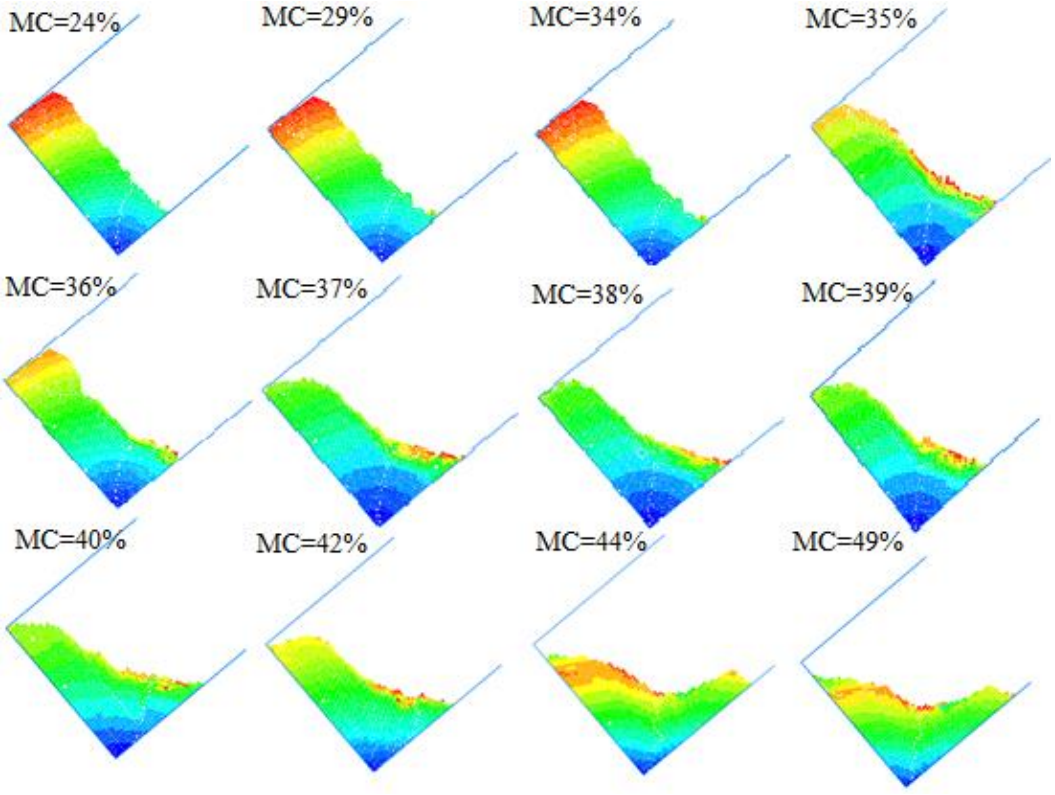

Figure 5.4 Appearance of particles inclined at 50 °(Blue color reflects the small displacement)

5.2.3 Parameter Selection

The contact parameters between particles at various MCs show great diversity. For predicting cargo flow accurately, the friction coefficients at various MCs need to be identified by the laboratory method as discussed. Table 5.1 shows the corresponding friction coefficient between particles at various MCs according to the static incline test from ClassNK.

Table 5.1 Constants of friction coefficient VS MC

Moisture Content	**Friction Coefficient**	**Rolling Friction Coefficient**
0.49	0.005	0.02
0.44	0.01	0.02
0.42	0.08	0.02
0.4	0.1	0.02
0.39	0.2	0.05
0.38	0.3	0.1
0.37	0.3	0.4
0.36	0.7	0.5
0.35	0.7	0.6
0.34	0.8	0.6
0.29	0.8	0.6
0.24	0.9	0.6

Fitting equations can be obtained to describe the relation between the friction coefficient and MC or degree of saturation. These two equations could be implemented into the liquefaction model in Chapter 6 to predict the cargo flow and cargo deformation. (See Figure 5.5 and Figure 5.6).

$$\text{fric} = \begin{cases} 0.9 & (MC \leq 24\%) \\ 20 * MC^2 - 12.6 * MC + 2.772 & (24\% \leq MC \leq 34\%) \\ 599320.6345 * e\text{^}(-38.665 * MC) & (34\% \leq MC \leq 50\%) \end{cases}$$

$$\text{rfric} = \begin{cases} 0.6 & (MC \leq 35\%) \\ -16.5 * MC + 6.45 & (35\% \leq MC \leq 39\%) \\ 0.02 & (39\% \leq MC \leq 50\%) \end{cases}$$

MC: moisture content

fric: friction coefficient

rfric: rolling friction coefficient

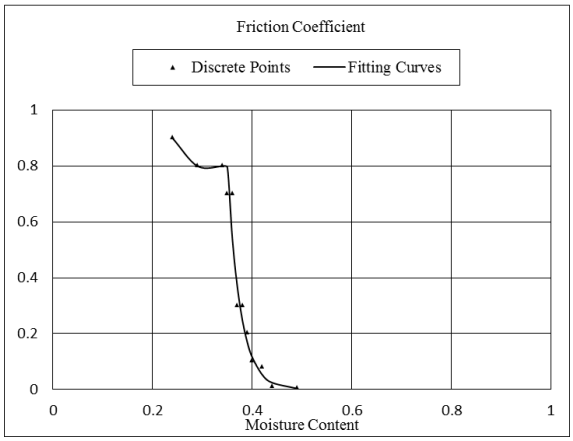

Figure 5.5 Friction coef. VS MC

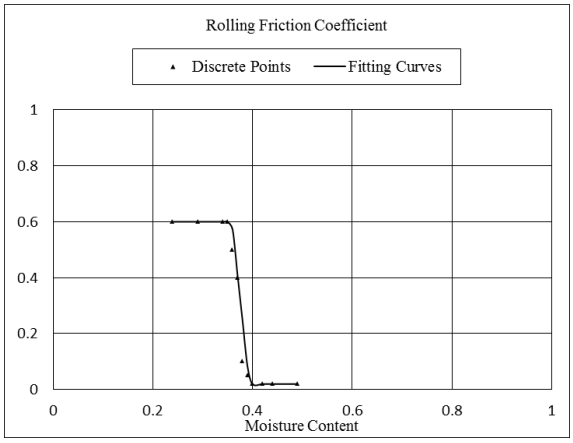

Figure 5.6 Rolling friction coef. VS MC

The dashpot force is produced by dashpots with viscosity given in terms of the normal and shear critical-damping ratios, β_n and β_s. Figure 5.7 - Figure 5.9 indicate that at various normal and shear damping ratios, the change of the displacement of the gravity centre shows little difference in the static incline test. Therefore, it is concluded that the normal and shear damping ratios derived from the Rolling Resistance Linear Model are insensitive to cargo flow.

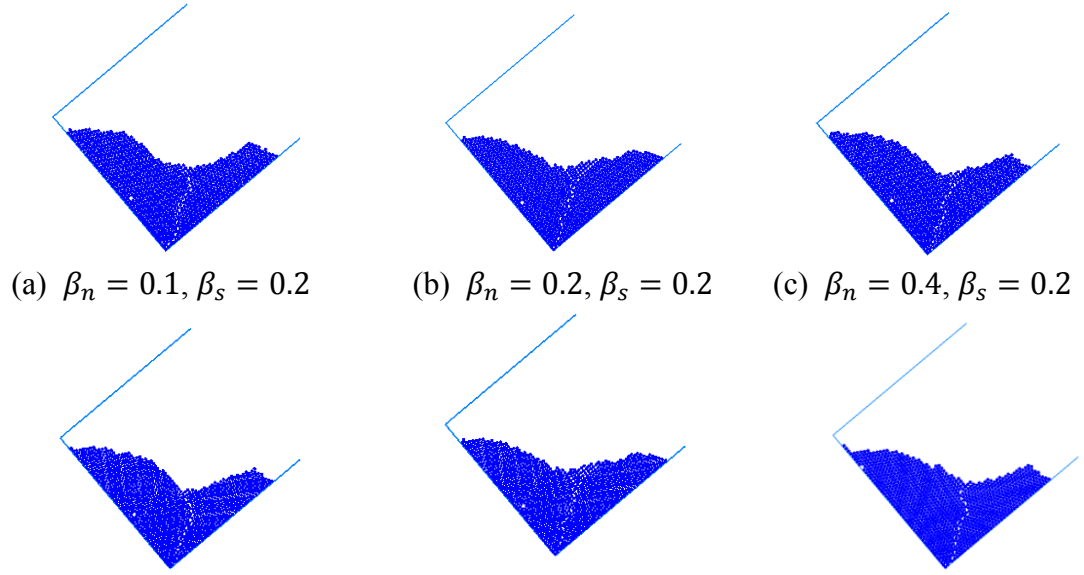

(a) $\beta_n = 0.1, \beta_s = 0.2$ (b) $\beta_n = 0.2, \beta_s = 0.2$ (c) $\beta_n = 0.4, \beta_s = 0.2$

(d) $\beta_n = 0.2,\ \beta_s = 0.1$ (e) $\beta_n = 0.2,\ \beta_s = 0.2$ (f) $\beta_n = 0.2,\ \beta_s = 0.4$

Figure 5.7 Parameter sensitivity analysis of normal and shear damping ratios in the static cline test (50 °)

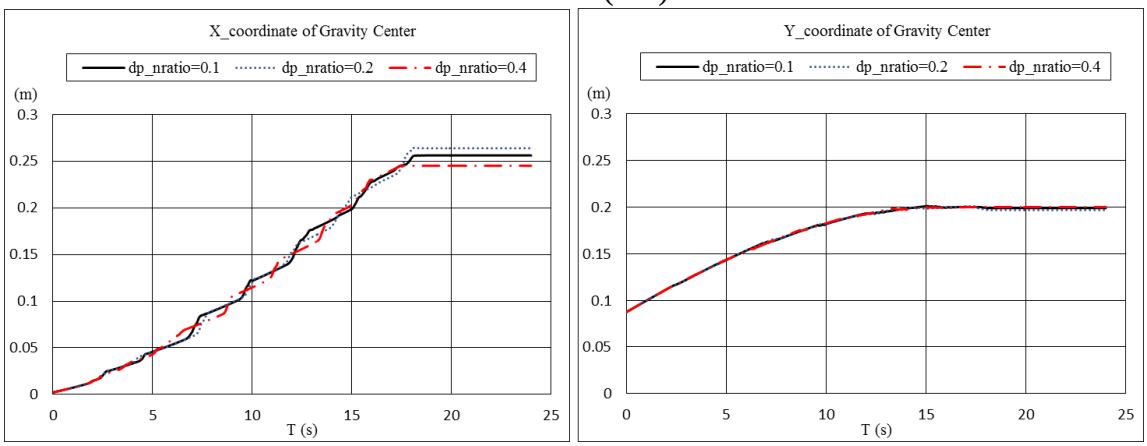

Figure 5.8 Coordinates of gravity centre of cargoes (50°;β_n=0.1, 0.2, 0.4; β_s=0.2)

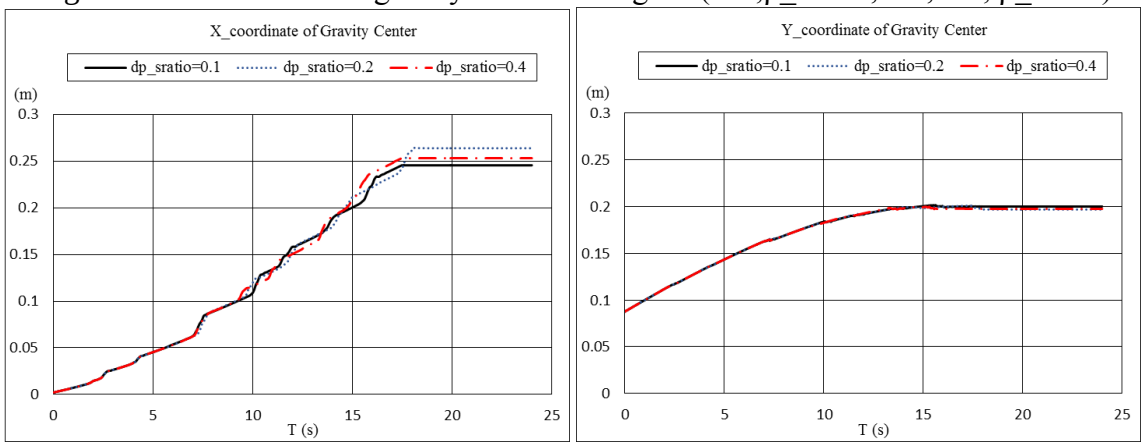

Figure 5.9 Coordinates of gravity centre of cargoes (50°;β_n=0.2; β_s=0.1, 0.2, 0.4)

5.2.4 Angle of Repose

The angle of repose is one of the most important macroscopic parameters, characterizing the behavior of granular materials (Spandonidis and Spyrou, 2013). The angle of repose or the critical angle of repose of a granular material is the steepest angle of descent or dip relative to the horizontal plane to which a material can be piled without slumping. As shown in Figure 5.10, the appearance of the angle of repose varies with the MC level. According to the liquefaction mechanism, cargoes with high MC or degree of saturation have a low friction coefficient, which generates a small angle of repose. For the container or ship hold filled by cargoes with a large angle of repose, the granular particles may have a large capacity to shift and contribute a large internal moment on the container or ship hold, especially for cargoes with a high MC or degree of saturation. Cargo shift will be discussed in the next section.

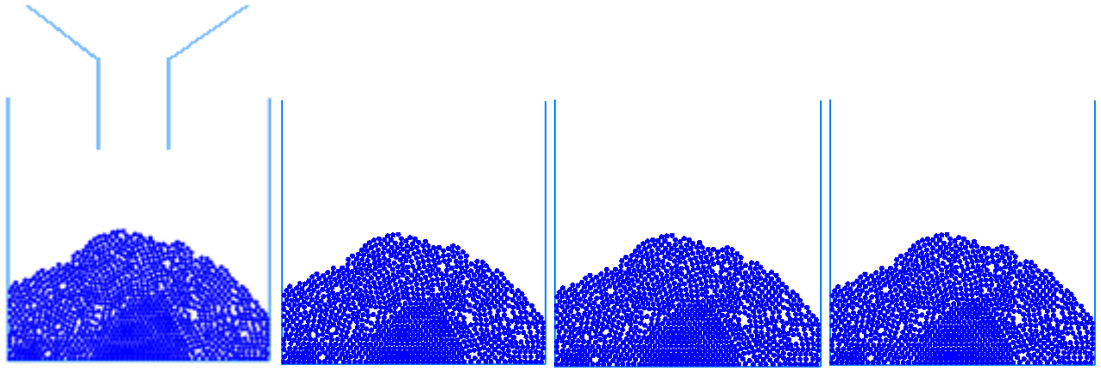

(a) MC= 24% (b) MC=29% (c) MC= 35% (d) MC=36%

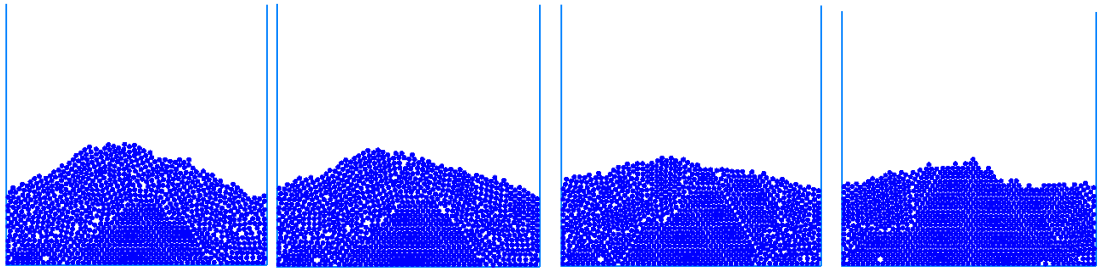

(e) MC= 37% (f) MC=38% (g) MC= 39% (h) MC=40%

Figure 5.10 Angles of repose at various MC

5.3 Cargo Shift

Solid bulk cargoes can shift by sliding failure or liquefaction consequence, and whilst the factors involved in each of these processes are different, the potentially disastrous consequences are the same listing or capsizing and/or structural damage (GARD, 1998). Trimming the cargo can prevent sliding failure (Lloyd's Register, 2013). Apart from reducing the possibility of cargo shift, weight distribution and stability are improved (GARD, 1998). However, it is appreciated that trimming has its disadvantages, e.g. increased time and cost at load and discharge ports. Solid bulk cargoes can flow like fluids. However, they cannot behave like water and be described by the Navier-Stokes equation (Spandonidis and Spyrou, 2016). Based on the fitting equation that relates the contact properties to MC, the shifting of cargo containing various MCs is investigated and the possibility of ship capsize is presented.

5.3.1 Uniform MC

A 2D rectangular structure (100cm*50cm) is used for the static incline test (see Figure 5.11). At the initial state, cargoes have a uniform moisture content of MC=24%, 29%, and 39%, separately. The container statically inclines at 50 degrees and then keeps stable.

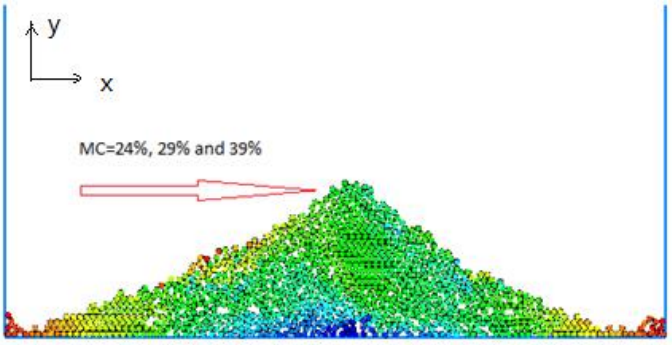

Figure 5.11 Peak pile of cargoes with uniform MC (Blue color reflects the small displacement)

It is observed from Figure 5.12 that the sample behavior shows various flow characteristics by monitoring the coordinates of the gravity centre at various initial MCs.

What is worth mentioning is that MCs of the sample are expressed in the form of correspondent friction coefficient. General speaking, with moisture content increasing, the sample comes close to liquid and tends to flow. However, from the results, the x coordinate of the gravity centre of the cargo with a MC of 29% is larger than that with a MC of 39%. It is concluded that the granular material flow is a complicated phenomenon that interacts with other particles. The interaction between particles shows nonlinear transition. Therefore, it is not completely reasonable to conclude that cargoes with higher MC or degree of saturation have higher flowability.

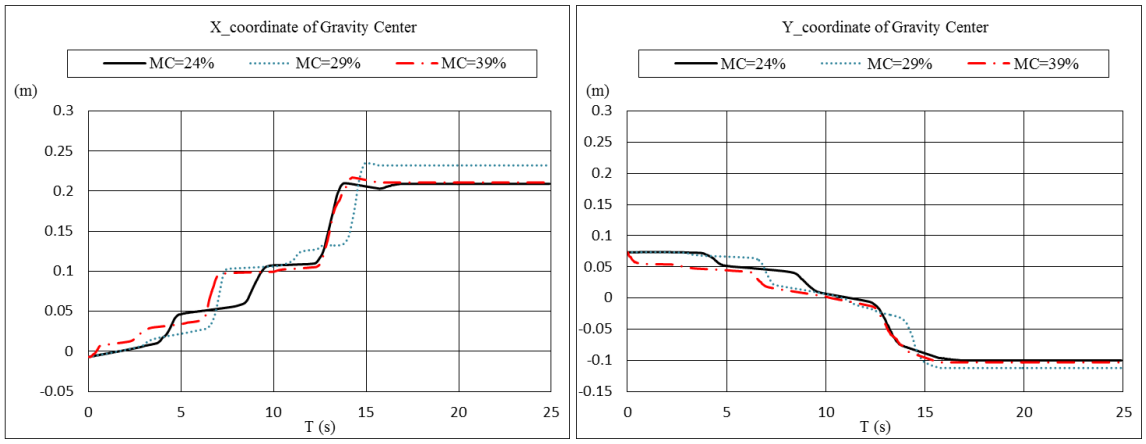

(a) X coordinate of gravity centre (b) Y coordinate of gravity centre

Figure 5.12 Coordinates of gravity centre of cargoes with uniform MC in static incline test (MC=24%,29%,39%)

5.3.2 Mixed MC

The same 2D rectangular structure (100cm*50cm) is used for the static incline test (see Figure 5.13). The main difference is that the MC of the sample at the bottom is set to a value of 49%, while the MC of the sample above is set to a value of 24%, 29% and 39%, separately. For cargoes of mineral ores loaded on board a vessel, the granular materiel is exposed to mechanical agitation and energy input in the form of engine vibrations, vessel movement, and wave impact, resulting in a gradual settling and compaction of the cargo. When some cargoes lost water holding ability, the wet base at the bottom will be generated. Therefore, cargoes at the bottom could be regarded as the wet base.

The likelihood of formation of a ‘wet base’ is a significant factor to be considered within the overall assessment and understanding of liquefaction and cargo stability. Some cargoes are susceptible to moisture migration and may develop a dangerous wet base, even if the average moisture content is less than the TML. As shown in Figure 5.14 and compared with Figure 5.12, it can be concluded that when the wet base is generated, flow characteristic of the cargoes is more evident. The cargo containing high MC flows to one side of the container with high probability. The coordinate of the gravity centre of cargoes changes to 0.37m along the x-axis and -0.15m along the y-axis after the static incline test if the wet base occurs. However, with no wet base, the coordinate of the gravity centre of the cargoes is 0.22m along x-axis and -0.1m along y-axis. That is, the presence of a wet base in the ship hold may result in a high flowability of the cargoes.

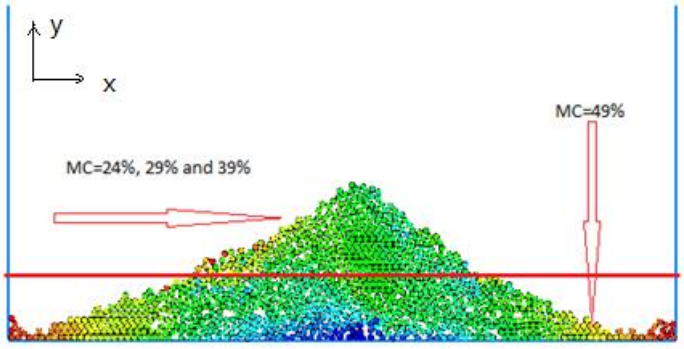

Figure 5.13 Peak pile of cargoes with mixed MC (Blue color reflects the small displacement)

Moreover, the free surface can be observed in the bottom holds of the vessels during a voyage. However, it is not necessarily an indication of liquefaction. The definition of liquefaction in earthquake engineering is not suitable for the cargo liquefaction discussed above. However, the presence of the wet base in the corners of the hold does decrease ship stability greatly. The area of the wet base is determined by a range of parameters, including the cargo holding water ability, cargo strength, the void ratio, cargo stow formation, initial bulk density and initial moisture content. To avoid the influence of the wet base on the ship, some recommendations and precautions are discussed as follows:

(1) Control the moisture content of cargoes when loading;

(2) Spread out the cargoes from peak pile to flat pile during carriage;

(3) Effective bilge well pumping is necessary;

(4) Prevent water infiltration to the hold;

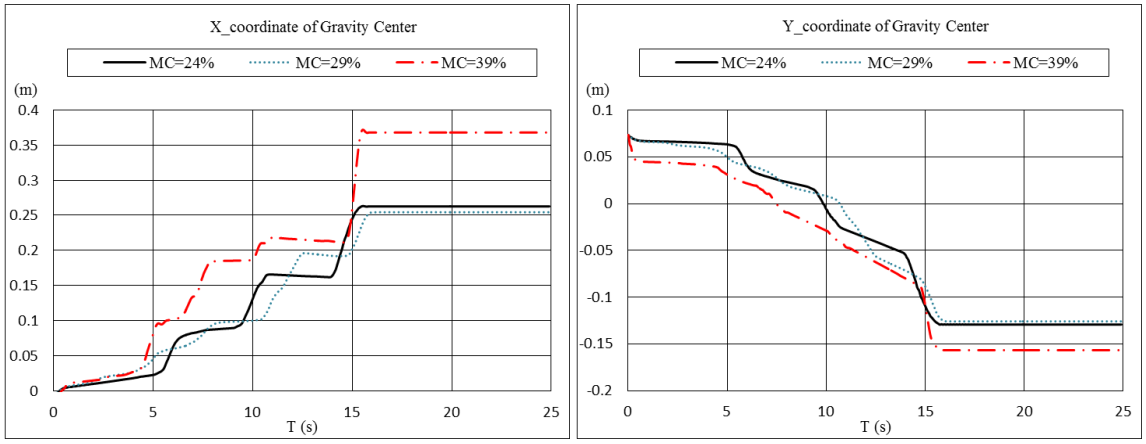

(a) X coordinate of gravity centre (b) Y coordinate of gravity centre

Figure 5.14 Coordinates of gravity centre of cargoes with mixed MC in static incline test (Bottom: MC=49%, Top: MC=24%, 29%, 39%)

5.3.3 Possibility of Causing Ship Capsizing

In this section, a probability of causing ship capsizing is discussed to investigate the cargo collapse effect. The angular velocity of the container is shown in Figure 5.15 in one circle. When the container rotates to a maximum degree at 6s, the friction coefficient of the cargoes in the region, ranging from x=-0.5m to x=-0.1m, instantaneously weakens to investigate the cargo collapse. The shear strength of particles in this region decreases as the friction coefficient decreases, causing cargo collapse (See Figure 5.16). When the container returns to the initial position again at 8.5s, the coordinate of the centre of gravity migrates to one side and the position of the gravity centre of the container greatly shifts. The migration of gravity centre in the simulation of container 1 (50cm*35cm) does not seem obvious. Therefore, container 2 (100cm*35cm) is used to compare with container 1. As shown in the results in Figure 5.17 and Figure 5.18, when the container, such as container 2, has enough space for particles to flow, cargoes tend to flow to one side and stay stable during the collapse. Consequently, the gravity centre of the container will be shifted greatly, which may reduce ship stability.

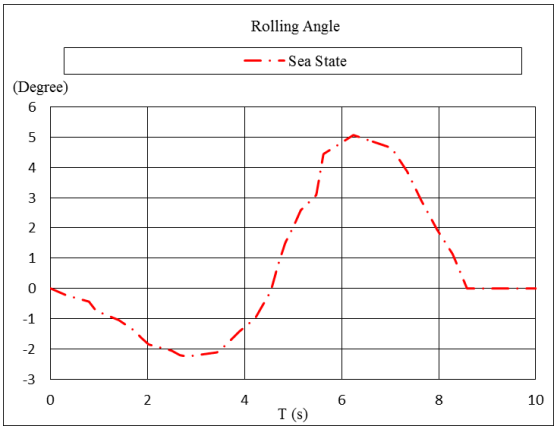

Figure 5.15 Motion of the container

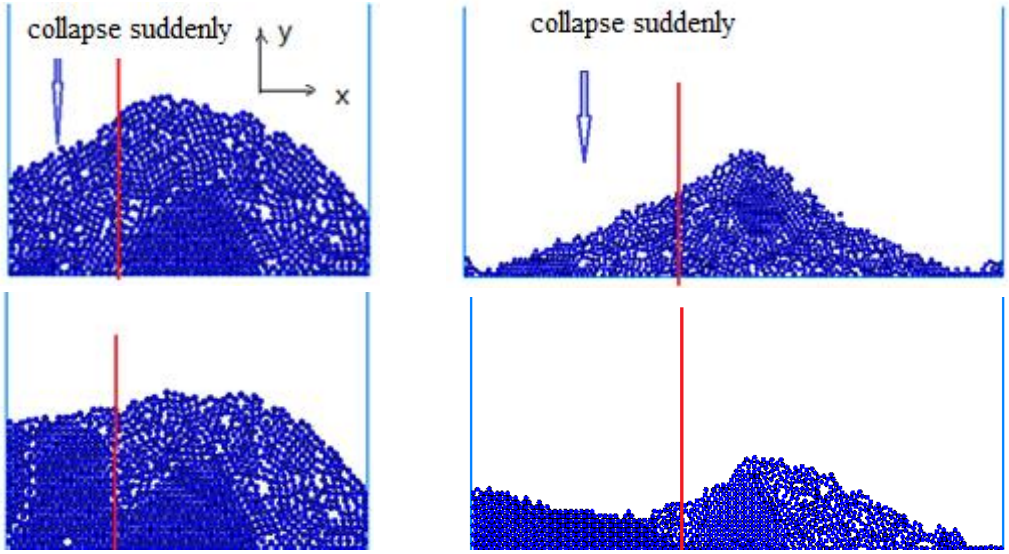

Figure 5.16 Comparison before and after cargo collapse (container 1: left; container 2: right. particles: 1024)

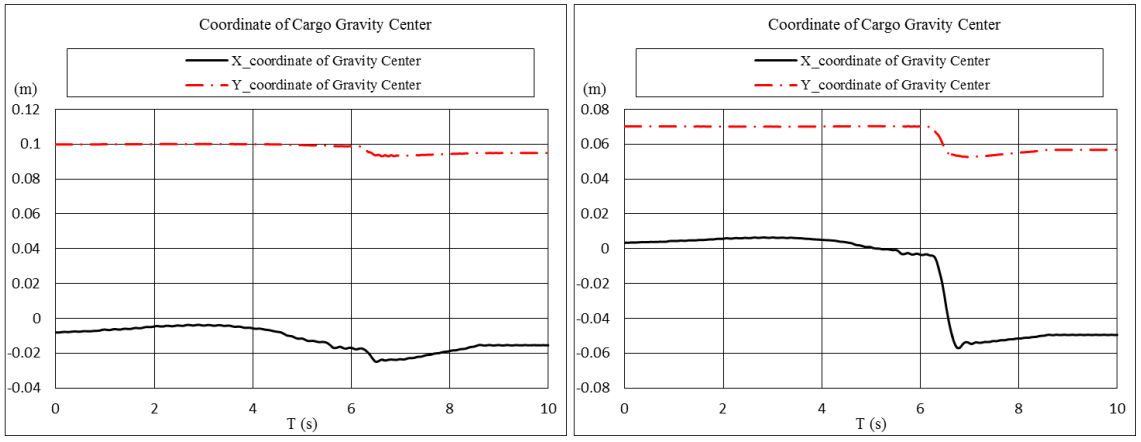

Figure 5.17 Coordinate of gravity centre of the cargoes during collapse (container 1: left; container 2: right)

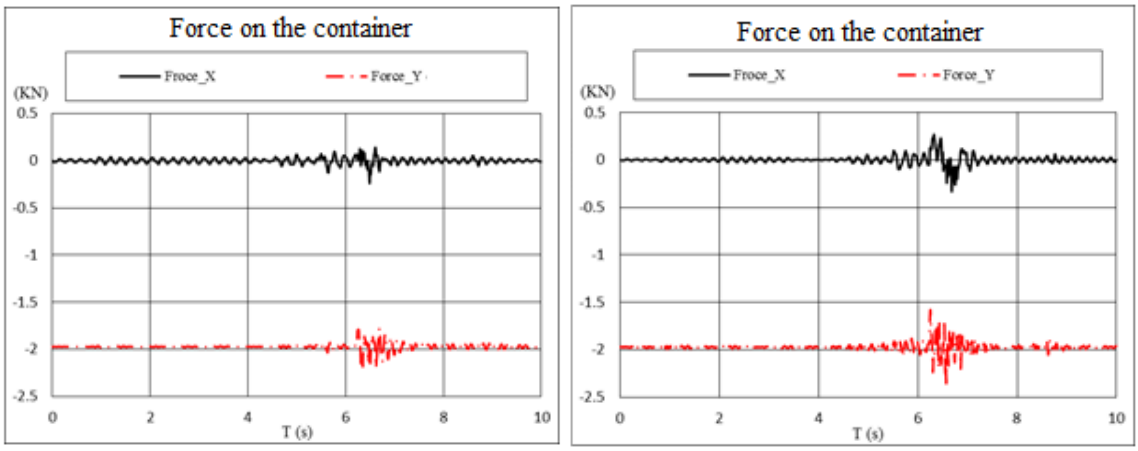

Figure 5.18 Fluctuation forces acting on container during cargo collapse (container 1: left; container 2: right)

5.4 Dynamic Stability Analysis

Sway and roll oscillations of a 2D rectangular structure (50cm*50cm) varying with amplitude, frequency and initial degree of saturation of cargoes are investigated to identify the interaction between cargo shift and container motion (see Figure 5.19).

5.4.1 Sway Motion

Firstly, sway oscillation varying with the initial MC of the cargoes is investigated. The amplitude is 0.3m and the frequency is 0.5HZ (Figure 5.20). The colour blue reflects that the displacement is small.

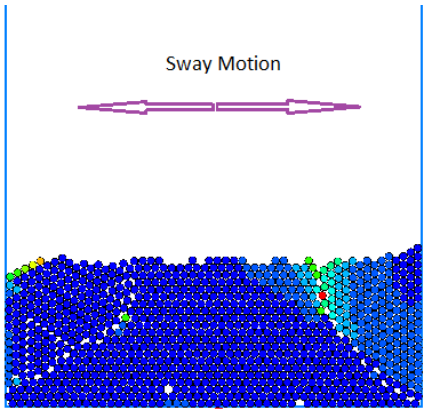

Figure 5.19 Initial appearance of cargoes for sway motion

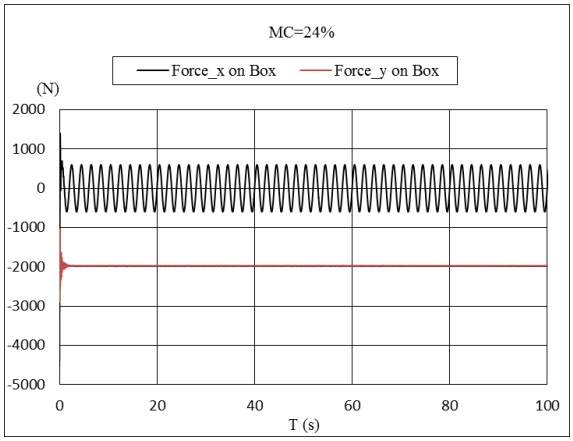

(a) MC=24%, Freq=0.5HZ, Ampl=0.3m

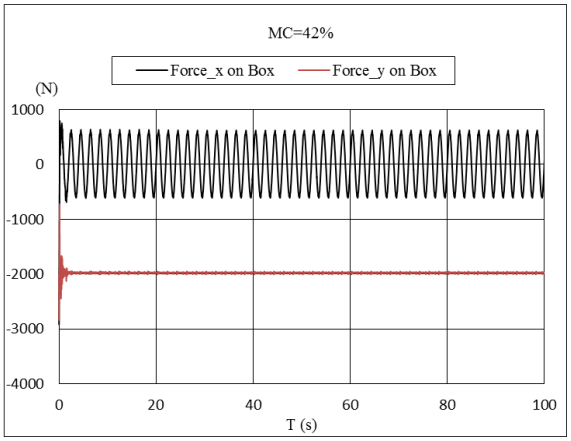

(b) MC=42%, Freq=0.5HZ, Ampl=0.3m

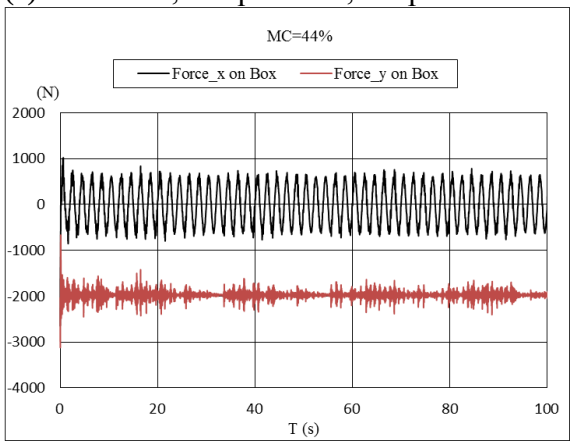

(c) MC=44%, Freq=0.5HZ, Ampl=0.3m

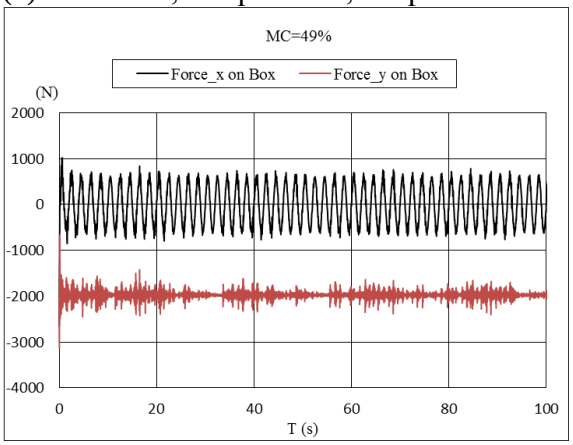

(d) MC=49%, Freq=0.5HZ, Ampl=0.3m

Figure 5.20 Fluctuation force acting on the container due to cargo shift versus MC (sway motion)

Following this, sway oscillation, varying with amplitude and frequency, is tested. (See Figure 5.21 and Figure 5.22).

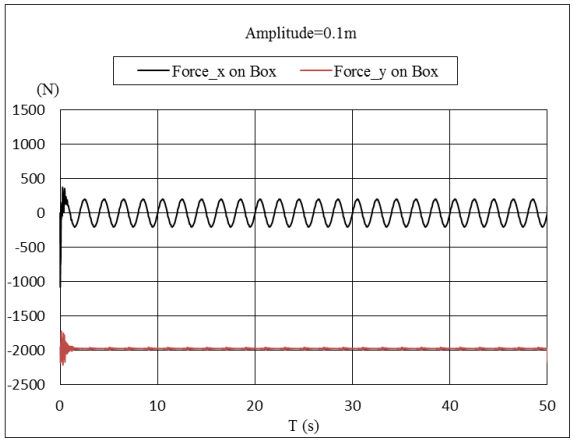

(a) MC=44%, Freq=0.5HZ, Ampl=0.1m

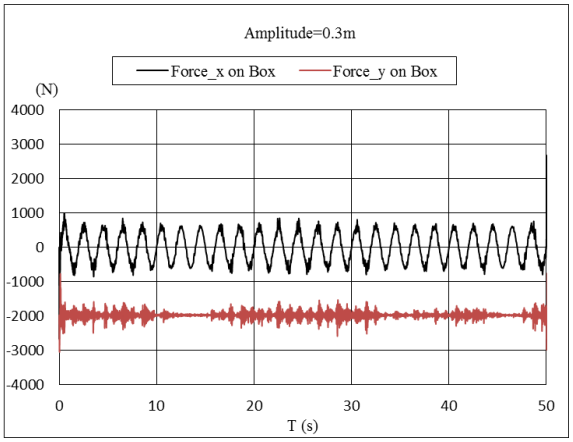

(b) MC=44%, Freq=0.5HZ, Ampl=0.3m

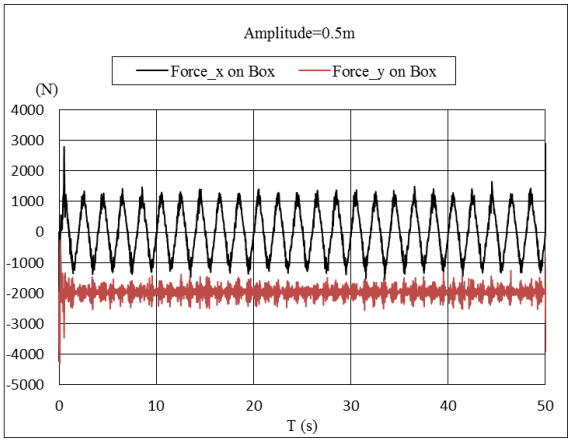

(c) MC=44%, Freq=0.5HZ, Ampl=0.5m

Figure 5.21 Fluctuation force acting on the container due to cargo shift versus amplitude (sway motion)

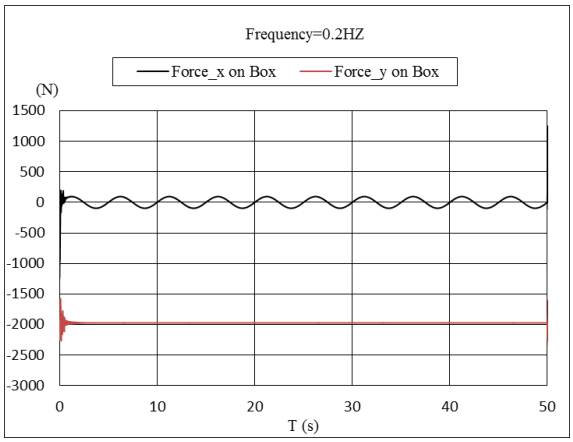

(a) MC=44%, Freq=0.2HZ, Ampl=0.3m

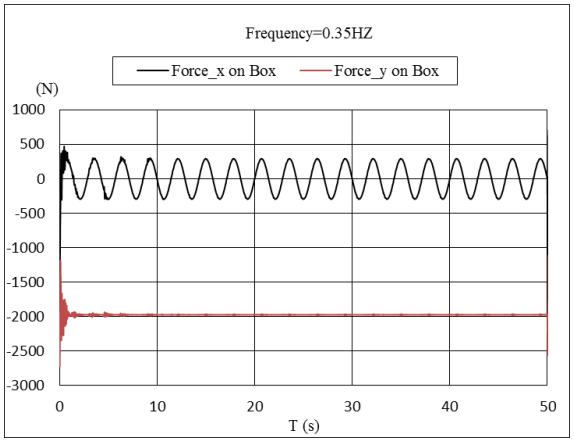

(b) MC=44%, Freq=0.35HZ, Ampl=0.3m

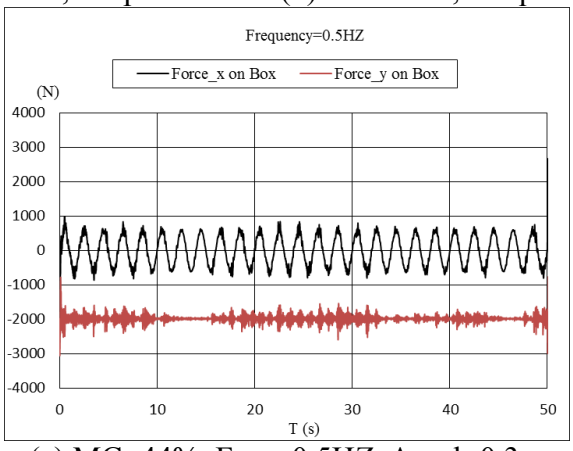

(c) MC=44%, Freq=0.5HZ, Ampl=0.3m

Figure 5.22 Fluctuation force acting on the container due to cargo shift versus frequency (sway motion)

5.4.2 Roll Motion with Flat Pile

Roll oscillation with the flat pile of cargo distribution varying with moisture content is tested. The rotation centre is as shown in Figure 5.23. The displacement amplitude is 25 degrees (0.4363rad) and frequency is 0.2HZ (see Figure 5.24).

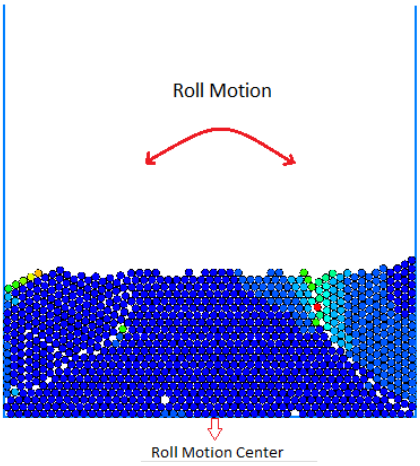

Figure 5.23 Initial appearance of cargoes for roll motion with flat pile

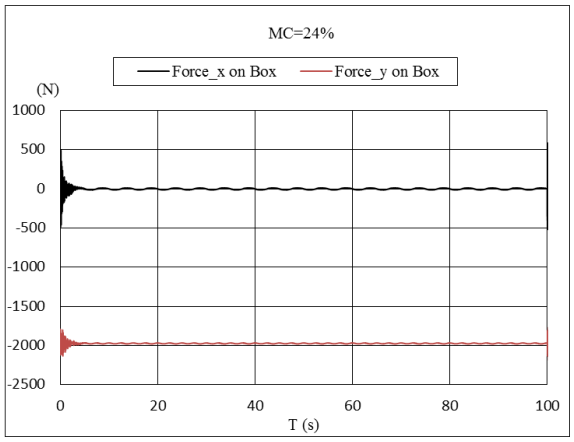

(a) MC=24%, Freq=0.2HZ, Ampl=25 °

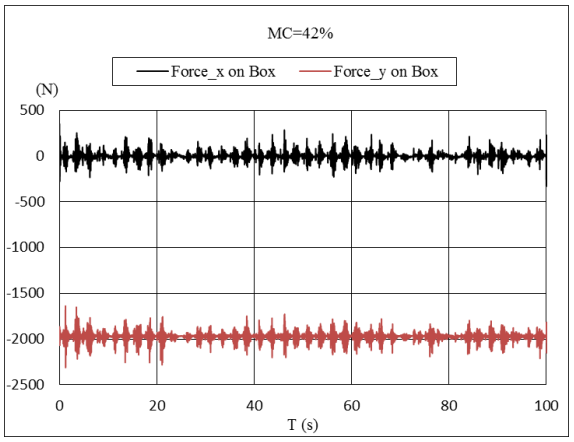

(b) MC=42%, Freq=0.2HZ, Ampl=25°

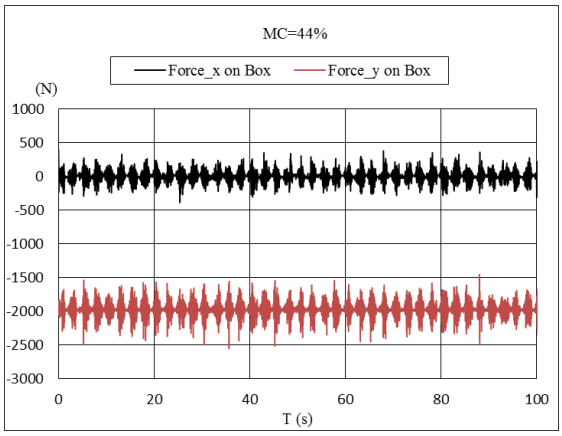

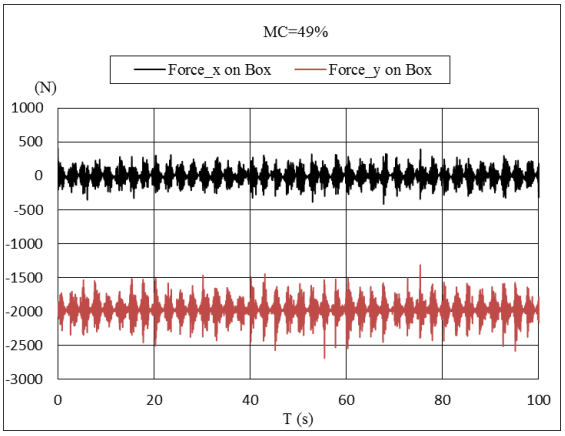

(c) MC=44%, Freq=0.2HZ, Ampl=25° (d) MC=49%, Freq=0.2HZ, Ampl=25°

Figure 5.24 Fluctuation force acting on the container due to cargo shift versus MC (roll motion with flat pile)

Then, roll oscillation varying with amplitude and frequency is tested (see Figure 5.25 and Figure 5.26).

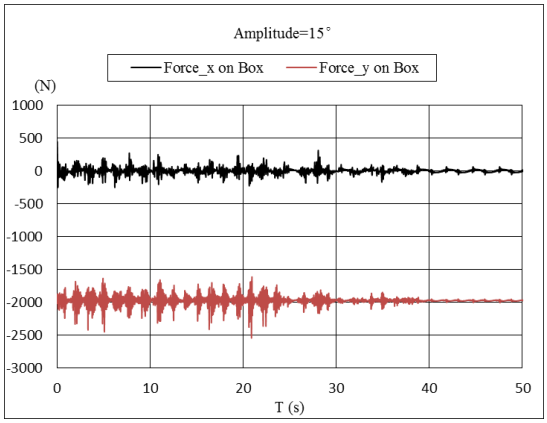

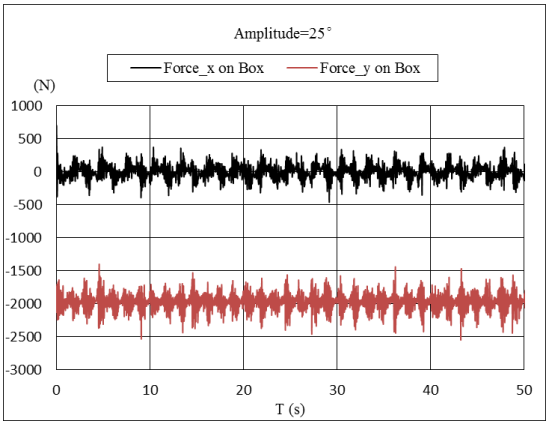

(a) MC=44%, Freq=0.35HZ, Ampl=15° (b) MC=44%, Freq=0.35HZ, Ampl=25°

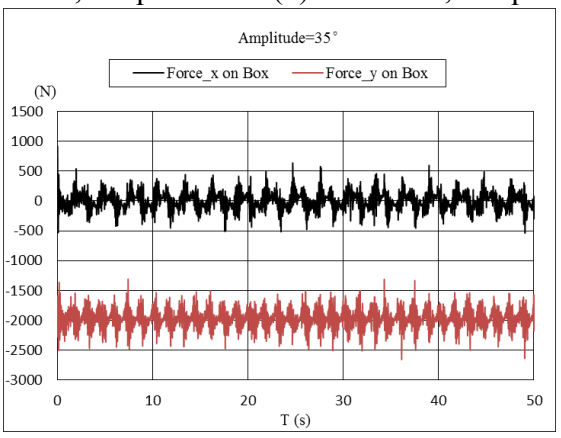

(c) MC=44%, Freq=0.35HZ, Ampl=35°

Figure 5.25 Fluctuation force acting on the container due to cargo shift versus amplitude (roll motion with flat pile)

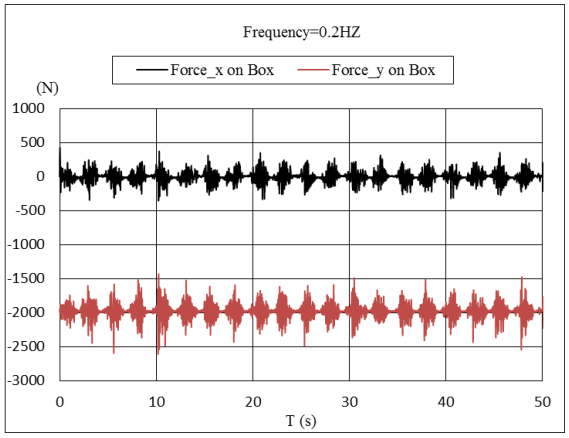

(a) MC=44%, Freq=0.2HZ, Ampl=25°

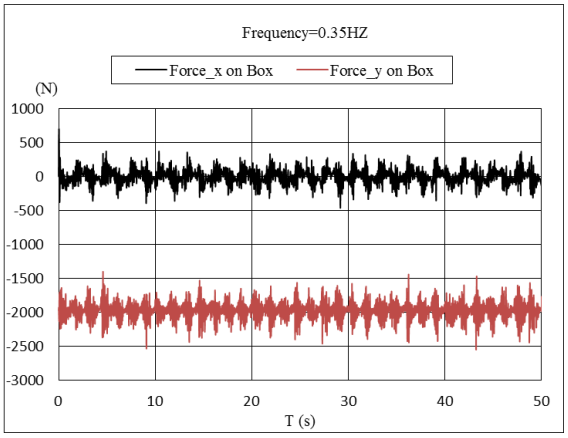

(b) MC=44%, Freq=0.35HZ, Ampl=25°

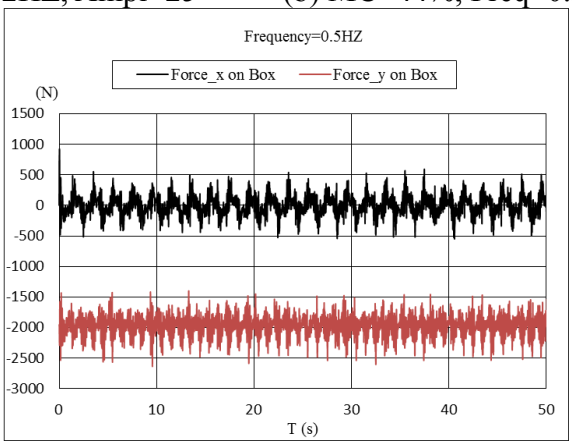

(c) MC=44%, Freq=0.5HZ, Ampl=25°

Figure 5.26 Fluctuation force acting on the container due to cargo shift versus frequency (roll motion with flat pile)

5.4.3 Roll Motion with Peak Pile

The angle of repose may be generated at the time of loading cargoes. When exceeding this angle, the granular material begins to flow. The roll oscillation with the peak pile of the cargo distribution is investigated in this section to identify the interaction between cargo shift and container motion (see Figure 5.27). First, roll oscillation varying with moisture content is tested. The amplitude is 25 degrees (0.4363rad) and frequency is 0.2HZ (see Figure 5.28).

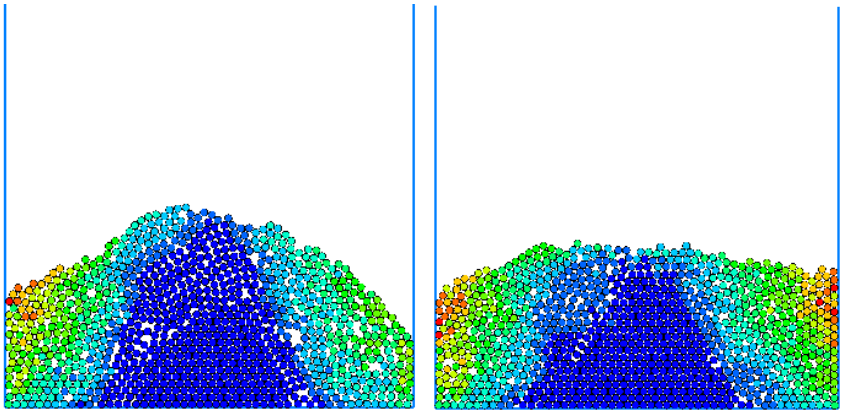

Figure 5.27 Appearance of Initial State (left) and after shaking state (right) of cargoes for roll motion with peak pile

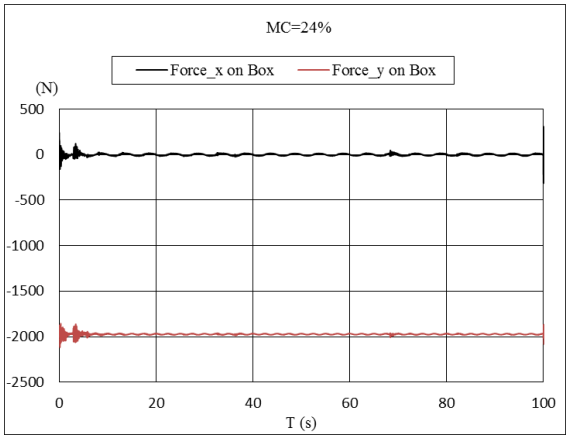

(a) MC=24%, Freq=0.2HZ, Ampl=25°

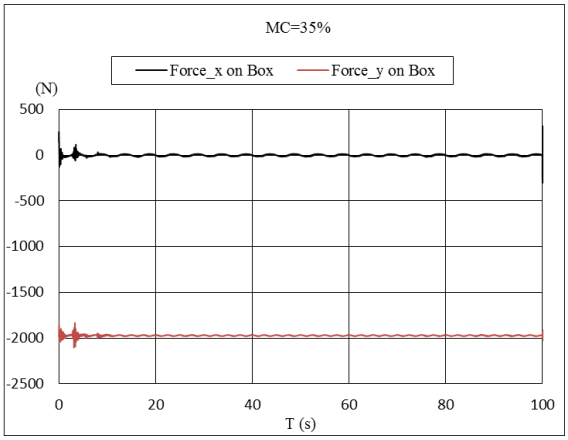

(b) MC=35%, Freq=0.2HZ, Ampl=25°

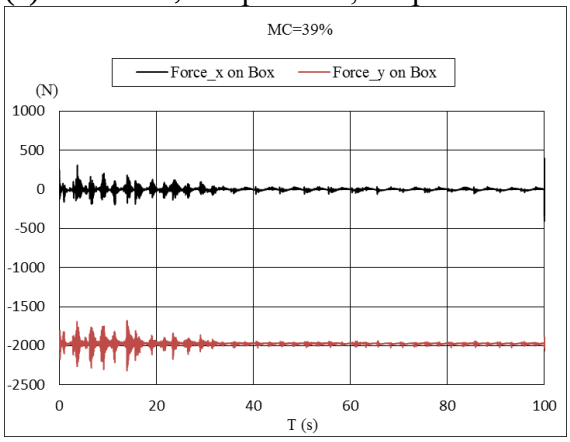

(c) MC=39%, Freq=0.2HZ, Ampl=25°

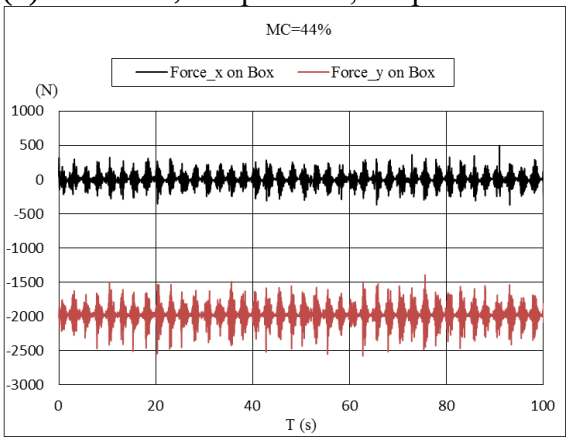

(d) MC=44%, Freq=0.2HZ, Ampl=25°

Figure 5.28 Fluctuation force acting on the container due to cargo shift versus MC (roll motion, peak pile)

Roll oscillation varying with amplitude and frequency is tested (see Figure 5.29 and Figure 5.30).

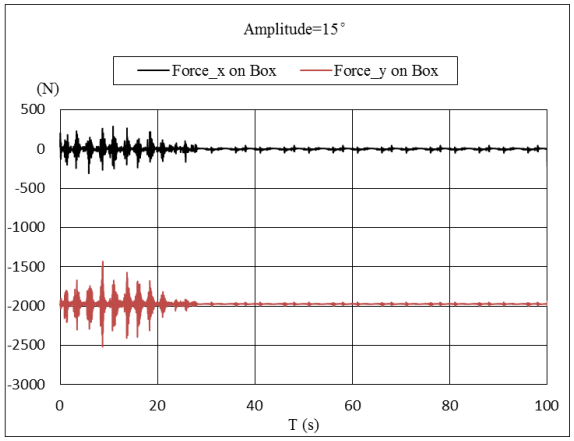

(a) MC=44%, Freq=0.35HZ, Ampl=15 °

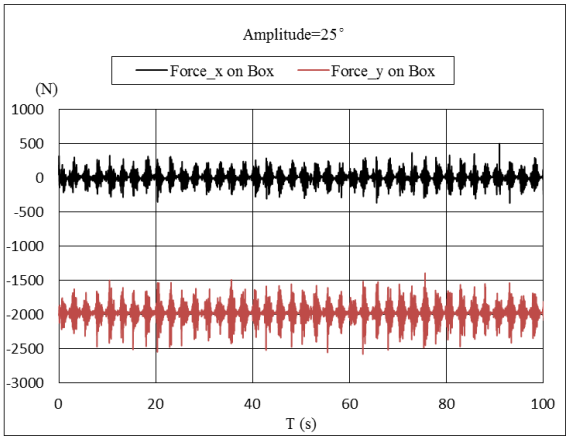

(b) MC=44%, Freq=0.35HZ, Ampl=20 °

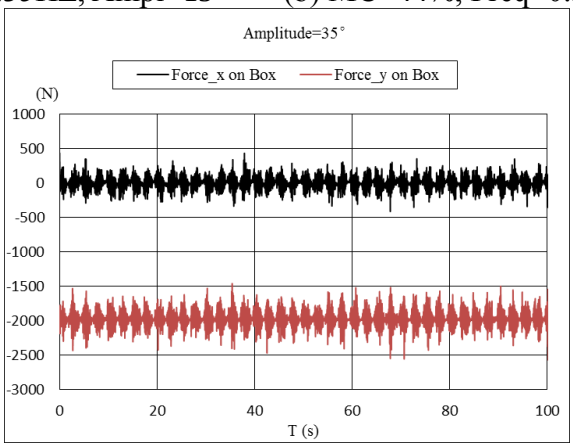

(c) MC=44%, Freq=0.35HZ, Ampl=35°

Figure 5.29 Fluctuation force acting on the container due to cargo shift versus amplitude (roll motion, peak pile)

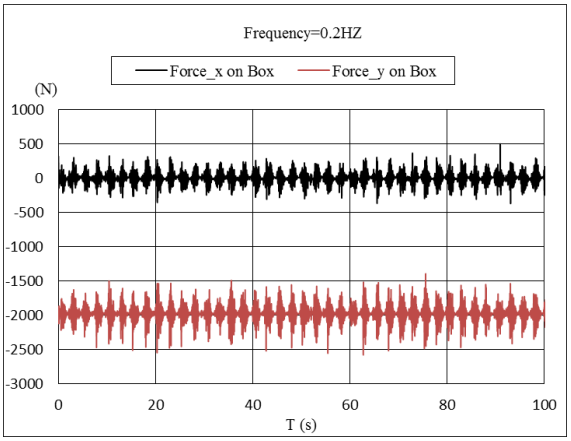

(a) MC=44%, Freq=0.2HZ, Ampl=25°

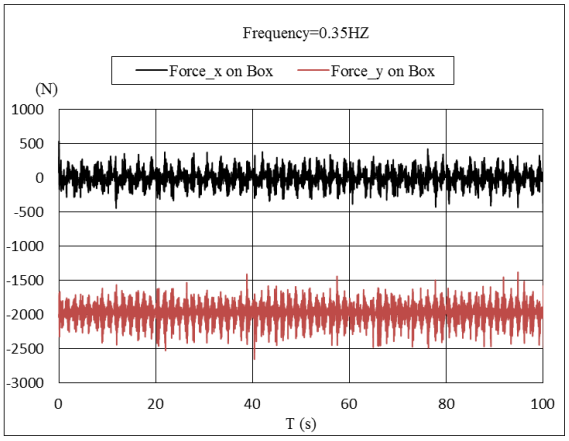

(b) MC=44%, Freq=0.35HZ, Ampl=25°

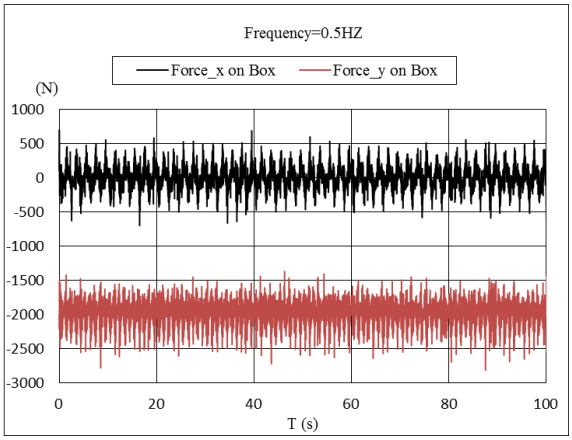

(c) MC=44%, Freq=0.5HZ, Ampl=25 °

Figure 5.30 Fluctuation force acting on the container due to cargo shift versus frequency (roll motion, peak pile)

5.4.4 Closure

Sway and roll oscillation of a 2D rectangular structure (50cm*50cm) varying with amplitude, frequency and initial degree of saturation of cargoes were investigated to identify the fluctuation force on the container due to cargo shift, which is similar to the research on the displacement of the centre of mass of materials by Spandonidis & Spyrou (2013).

Considering the sway oscillation, some findings are follows:

1) If the amplitude and the frequency are constant, the maximum fluctuation force along x acting on the container from cargo shift with a MC of 49% is 1.2 times larger than that with a MC of 24%.
2) If the MC and the frequency are constant, the maximum fluctuation force along x, acting on the container from cargo shift with the amplitude of 0.5m, is 6 times larger than that with an amplitude of 0.1m.
3) If the MC and the amplitude are constant, the maximum fluctuation force along x acting on the container from cargo shift with a frequency of 0.5HZ is 8 times larger than that with a frequency of 0.2HZ.

It can be concluded that the cargoes have a high probability to flow with higher initial MCs of cargoes and higher frequencies and amplitudes of external loadings. As for the roll oscillation, cargo flow with a flat pile and a peak pile were compared. The results showed that the flowability of cargoes with a peak pile is more obvious than those with a flat pile. Under the same initial condition, cargoes with peak pile are more likely to liquefy. Cargo liquefaction is susceptible to the distribution of cargoes in the hold. Therefore, during the loading and carriage of cargoes, a peak pile should be avoided.

5.5 Conclusions

A static incline test conducted by ClassNK was used to identify the contact properties at various MCs based on the DEM. According to the contact properties, cargoes containing uniform and mixed MCs were investigated to identify cargo shift. Generally speaking, with moisture contents increasing, the cargoes become close to liquid and tend to flow.

Dynamic stability analysis was conducted to identify the modes of motion, degree of saturation of cargoes, as well as amplitude, and frequency that affects cargo shift. It was concluded that the cargoes have a high probability to flow with higher initial MC of cargoes and higher frequency and amplitude of the external loading. Among these three factors, the only one that can be controlled during the voyage is the degree of saturation. Therefore, reducing the degree of saturation in cargoes will enormously reduce the ensuing problems of cargo shift during transportation of granular cargoes. Under the same initial condition, the cargoes with peak pile were more likely to liquefy. Therefore, during the loading and carriage of cargoes, the peak pile should be avoided.

The DEM can effectively simulate the cargo flow at different MCs by updating the friction coefficient at the contact pieces between particles. According to the comparison with experimental data from ClassNK, this method shows a good agreement. However, after all, the cargoes are dry granular particles which do not contain moisture inside. Therefore, this method to simulate unsaturated granular particles still needs to be investigated further.

Chapter 6 DEM Liquefaction Model

The potential of a cargo to liquefy is currently assessed with a set of laboratory measurements (prescribed in IMSBC), which constitute a fundamental requirement of the Code. However, in view of the ambiguity of testing (unavailability or non-compliance) and the variability of conditions (i.e. ship design and operation, and environmental conditions) that can lead to it, it is necessary to investigate the root causes that trigger the phenomenon and address the problem in a comprehensive manner. Most codes focusing on the fluid-structure interaction is based on saturated specimens, which have some limitations in addressing cargo liquefaction as cargoes contain three phases: water, air and solid skeleton which are in a unsaturated state. Therefore, based on some assumptions, the DEM liquefaction model is presented in this chapter, followed by experimental data to validate the model. The whole liquefaction process can be addressed by this model to capture the process from initial state to liquefied state, and the interaction between cargo shift and the response of the 2D rectangular structure. This DEM liquefaction model can combine with ANSYS Fluent software to assess the response of a 2D rectangular structure in waves due to cargo shift, particularly addressing the liquefaction phenomenon as will be discussed in Chapter 7.

6.1 Assumptions

The Particle Flow Code (PFC) cannot achieve the elastic-plastic strain, as the ball is considered as a rigid body. Further, the moisture between particles cannot be presented based on the code, as discussed in Chapter 5. Therefore, some assumptions are specified before using the DEM to address the liquefaction problem:

1) Each particle is regarded as a hypothetical assembler of particles, including many solid particles, water and air. The cargo just contains the solid skeletons. The porosity of the particles is also a hypothetical porosity. During compaction, the air will be expelled. When the unsaturated state becomes saturated, the volume of air becomes nil and the

water will attach the specific solid particles permanently, which cannot flow out. Water and air cannot be transferred to neighboring artificial particles as a result of exerted elastic-plastic strain.

2) The radius of the particle can be scaled with the elastic-plastic strain according to the stress on the particles in PFC based on the UBCSAND model. The amplitude of the strain depends on the artificial deformation parameters (
3) Table **3.1**).
4) Various friction coefficients can be used to represent various moisture contents. From the simulation results obtained in section 5.2 and the comparison with the experimental data from ClassNK, cargo behavior at different MCs can be described by the appropriate friction coefficient and rolling friction coefficient. If the friction coefficient can be identified at different MCs by laboratory experiments, the flow characteristics of cargoes can be approximately modelled, taking no account of moisture. The friction coefficient will be updated in the liquefaction model during compaction according to the existing fitting equations between friction coefficient and moisture content.

Based on the assumptions above, the DEM liquefaction model can predict the cargo flow, deformation, and liquefaction phenomenon. However, the interaction between water, air and solid skeleton are neglected, which may decrease the accuracy of the prediction. Some validations are presented in the follow section based on the DEM liquefaction model.

6.2 Model Validation

Validation of the approach includes two laboratory testing methods: the simple shear test and cyclic shear test. However, there is lack of experimental data. Therefore, the methods are not sufficient in testing the accuracy of the approach.

6.2.1 Simple Shear Test

The simple shear test is a laboratory testing method used to directly determine the shear modulus of soil. The principle of the test is inducing simple shear in a cylindrical soil sample (usually peat). The cylindrical soil sample is confined by a flexible wire-reinforced rubber membrane usually inside metal rings. The sample is placed between the base pedestal and the top cap. Vertical stress is applied to the sample from the top cap. The sample is sheared by moving the rings from side to side. This vertical load creates a total normal stress σ. In the simple shear test, the shearing takes places over the entire height of the sample. Therefore, the shearing strain γ can be measured in the simple shear test as (Jean-Louis Briaud, 2013):

$$\gamma = \Delta x / h_0$$

where Δx is the difference in horizontal movement between the top and the bottom of the sample and h_0 is the initial height of the sample. The shear stress τ is measured as the shear force divided by the cross-sectional area of the sample. Thus, the simple shear test gives the shear stress-strain curve for the sample and therefore a shear modulus G. If for the unsaturated state, the testing procedure is the same except for the measurement of the water stress, such as a *tensiometer*.

A DSS specimen filled with "balls" is considered for the PFC simulations herein. First, balls are first randomly generated inside the specimen. Consolidation of the simulated specimen is performed by displacing the top and bottom boundaries in the negative and positive y-direction, respectively, to achieve a desired vertical effective stress, σ_v', for example, the value of 100kPa. In the simple shear test, spin velocity is 0.01*L (m/s), L is the length of the shearing specimen. Sabatina Cuomo (2016) conducted simple shear tests on the unsaturated soil and saturated soil. The soil is loose and has a metastable structure along steep slope. The soil specific gravity (Gs) is equal to 2.55. Two experimental tests with saturated condition and unsaturated condition were conducted, as shown in Table 6.1, and the samples in PFC are shown in Figure 6.1. The parameters used in the simulation

are given in Table 6.2.

Table 6.1 List of experimental tests

condition	Test	e	σ', $\sigma - u_a$ (kPa)
Saturated	CL	2.02	76
Unaturated	CL*	1.66	100
CL=Constant vertical Load; * suction 50 Kpa;			

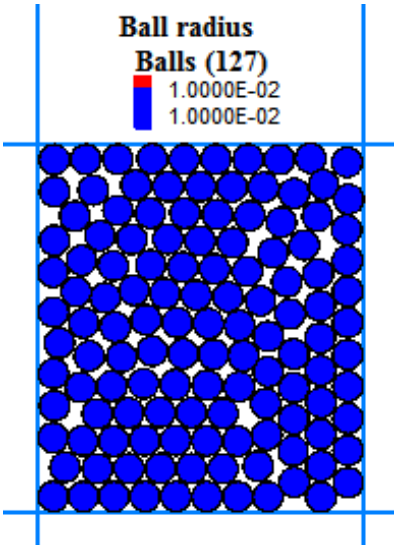

Figure 6.1 Simple shear samples

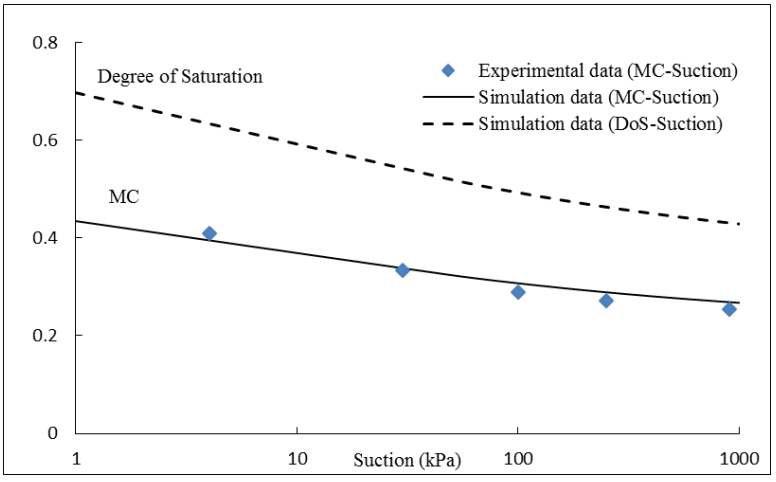

Figure 6.2 Soil Water Character Curve (MC: moisture content; DoS: degree of saturation)

Table 6.2 Coupled model input parameters for shear test

	Symbol	Saturated soil (Simple shear)	Unsaturated soil (Simple Shear)	Unsaturated soil (Cyclic Shear)
Deformation parameters	$\varphi_p(\circ)$	34.7	34.8	33
	$\varphi_{cv}(\circ)$	32	32	32
	k_B^e	5e8	5e10	1e5
	k_G^e	0.25e8	0.25e10	1e5
	k_G^p	5e8	5e10	5e4
	me, ne	0.5	0.5	0.5
	np	0.5	0.5	0.5
	R_f	0.7-0.98	0.7-0.98	0.7-0.98
	P_A	76kPa	100kPa	100kPa
Hydraulic parameters	g_a, g_n, g_c	0.5, 1.23, -0.624	0.5, 1.23, -0.624	5.0, 2.0, -1.0
	n_{sat}	0.721	0.721	1.0
	n_{res}	0.337	0.337	0.0
	MC(%)	51.9	51.9	-
	Poro_initial	0.668	0.624	0.5
Contact model parameters	*emod*	1e5	1e5	1e5
	kratio	2.0	2.0	2.0
	fric	0.8	0.99	Fig 5.1
	rfic	0.8	0.99	Fig 5.1
	dp_nratio	0.2	0.2	0.2
	dp_sratio	0.2	0.2	0.2
	dpmod	3	3	3

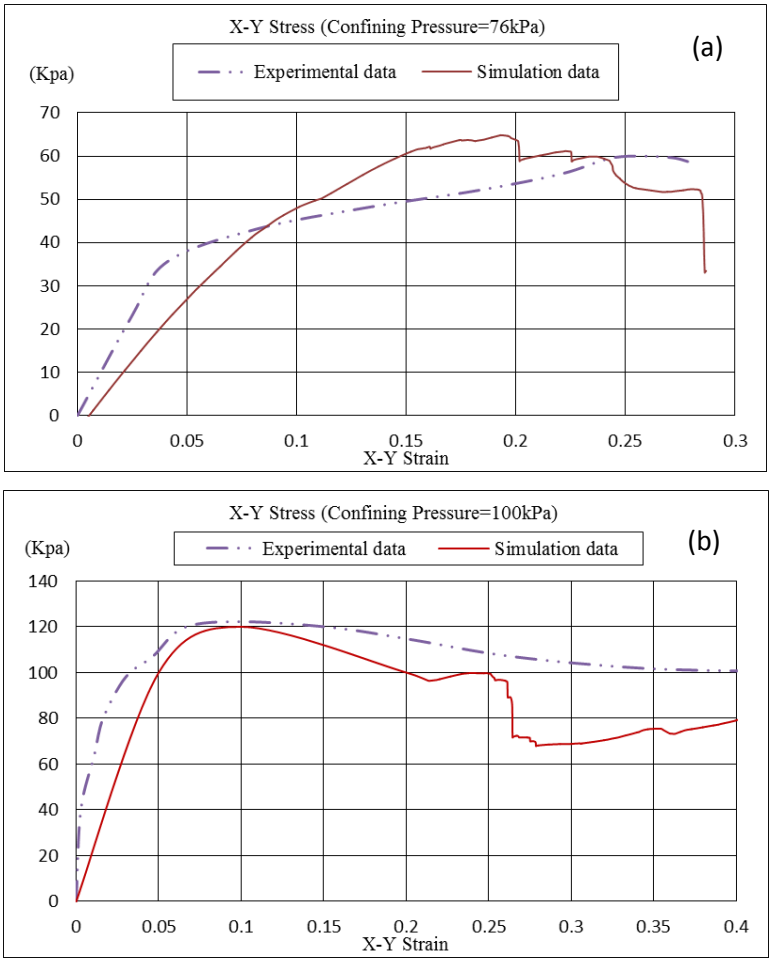

Figure 6.3 Compaction between Experimental results and simulation results. Simple Shear: (a) Saturated soil; (b) Unsaturated soil

The mechanical behavior of unsaturated soils is related to matric suction and water content or degree of saturation (Figure 6.2). As shown in Figure 6.3, when shearing to a certain extent, the specimens lose shear strength, which causes destruction. The simulation data shows good agreement with experimental data.

6.2.2 Cyclic Shear Test

Figure 6.4 presents the typical stress path and stress-strain response for a simulation with cyclic stress ratio (CSR=shear stress/vertical effective stress) of 0.08 and vertical effective

stress of 100 kPa. A gradual drop of vertical effective stress is observed from an initial value of 100 kPa with the application of cyclic shear until it reaches σ'_{vc}, a value of about 50kPa followed by a sudden overall drop of σ'_{vc} during the last two cycles. This is associated with the development of relatively large shear strains during the last two cycles of loading. During the shearing progress, the bulk modulus and shear modulus of the specimen decrease according to the UBCSAND liquefaction model. At the last two cycles, the deformation of cargoes is obvious due to the low bulk modulus and shear modulus after many cyclic shearing, causing a sudden drop of vertical effective stress. During cyclic shearing, a constant volume condition is enforced. It has been shown that the vertical stress acting on the top and bottom boundaries decreases gradually.

Based on the DEM liquefaction model developed in this chapter, at a constant of confining pressure (100kPa) and initial degree of saturation of 100%, specimen gradually is sheared and the effective stress decreases. When the shear modulus decreases to some extent, the shear strain suddenly becomes obvious, especially at the last several shearing cycles, which is similar to the experiment phenomenon — indicating shear failure. Compared to the experimental results, this further shows that the modelling approach presented in the thesis is suitable for addressing the cyclic behavior of the specimen, and the liquefaction behavior of cargoes.

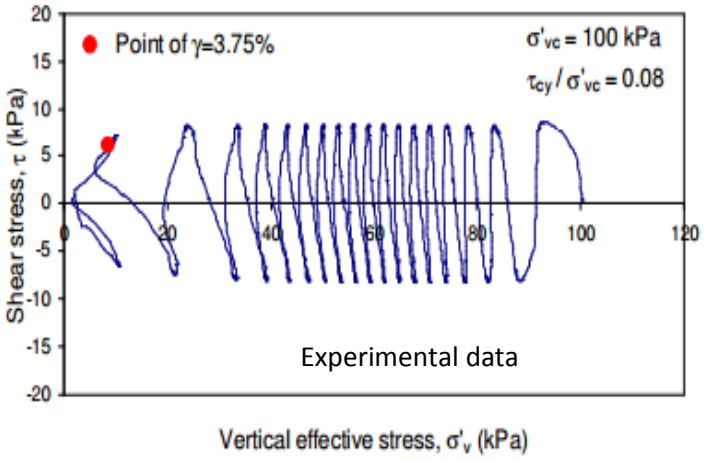

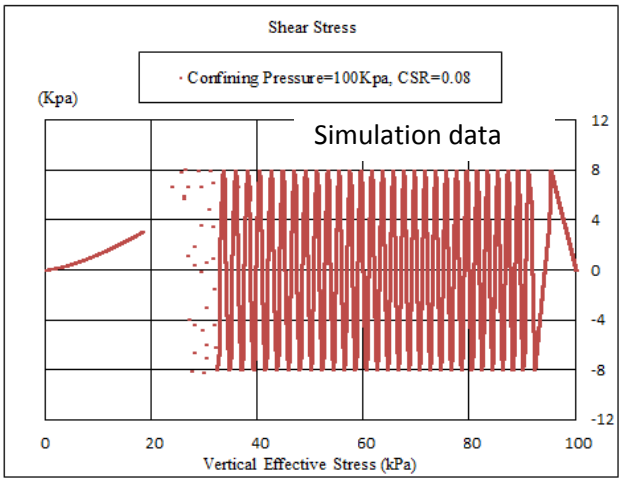

(a) Stress path

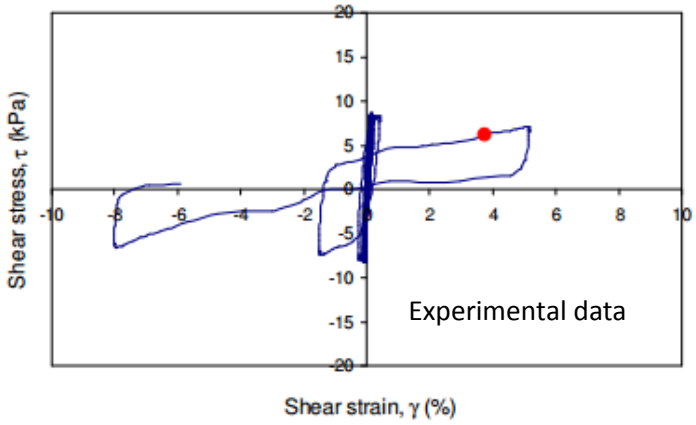

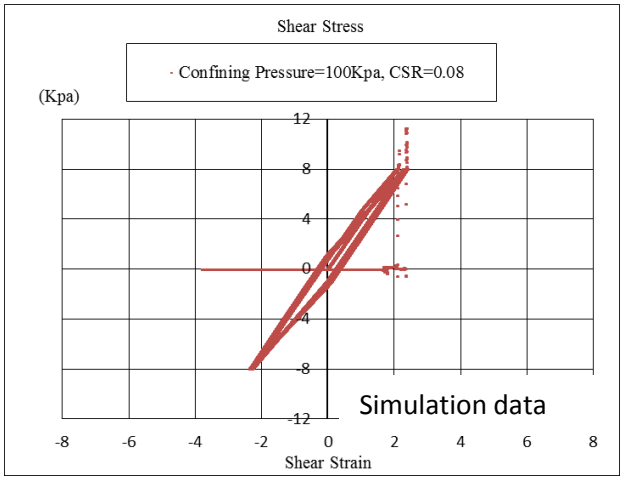

(b) shear stress-strain response

Figure 6.4 Results from cyclic laboratory DSS testing of Fraser River sand for CSR (τ/σ') of 0.08 (Wijewickreme et al. 2005)

6.3 Liquefaction Test

According to the numerical validations, this DEM liquefaction model can simulate the simple and cyclic shear stress-strain responses of the sample. During the voyage, the material is exposed to mechanical agitation and energy input, resulting in a gradual settling and compaction of the cargo. The cargo turns into a viscous fluid gradually. By specifying the movement of container or ship hold, the whole process of liquefaction can be determined by this liquefaction model in the form of time-domain analysis. Chapter 3 introduced contact parameters, deformation parameters and hydraulic parameters which need to be identified based on experimental methods. When studying ship response due to cargo shift, energy input like wave parameters also need to be provided. Based on the liquefaction model developed in the thesis, parametric investigation can be undertaken to identify the key parameters that trigger cargo and ship instabilities to investigate the root causes, as well as those that trigger the liquefaction phenomenon in order to address the problem in a comprehensive manner.

Before applying this liquefaction model, properties of cargo need to be identified by laboratory experiments, including the friction coefficient at different moisture contents (contact model parameters), bulk strengths (deformation parameters) and SWCCs (hydraulic parameters):

1) Contact model parameters: during compaction, the contact properties like friction coefficient will be updated. According to section 5.2, the flow characteristic varying with the degree of saturation or MC needs to be determined by the static incline test.
2) Deformation parameters: according to the stress on the particles based on the equation in section 3.1.2, the elastic-plastic strain of particles can be calculated. Deformation parameters will be obtained by simple shear and cyclic shear tests using an experimental approach. Meanwhile, with the deformation parameters, simple shear and cyclic shear tests will further verify the numerical method as shown in section 6.1 and section 6.2.
3) Hydraulic parameters: The soil-water characteristic curves (SWCCs) relate the water

content or degree of saturation to the pore water pressure (matrix suction) of a granular material. According to the initial degree of saturation and the elastic-plastic strain during compaction, the updated degree of saturation of particles will be calculated. The contact properties like friction coefficient can be determined to update the movement of the particles. Meantime, according to the SWCC, the pore water pressure can be validated by the pressure sensor in the experiment.

Employing the liquefaction model with the given parameters above, some information related to cargo liquefaction can be determined:

1) Evolution of the degree of saturation of each particle;
2) Liquefied percentage for all particles;
3) Liquefaction zone;
4) The fluctuation forces on the hold or container.

6.3.1 Hypothetical Property of A Cargo

Given a hypothetical property of a cargo, we can identify what factors such as amplitude, frequency or moisture trigger cargo liquefaction. During the carriage, the cargoes may experience compaction. Although the moisture content does not change, the degree of saturation increases during the compaction. In fact, when the degree of saturation increases, the friction coefficient and rolling friction coefficient decrease. Therefore, the relation of friction coefficient to the degree of saturation should be identified by the experimental approach before the assessment of cargo liquefaction. Two fitting equations are presented to describe the relation between the friction coefficient and rolling friction coefficient and the degree of saturation according to the experimental data from ClassNK, which can be implemented into the DEM liquefaction model, as shown in Figure 6.5. Deformation parameters and hydraulic parameters also need to be determined by laboratory experiment. In the following liquefaction simulations, the validation properties in Table 6.3 will be used.

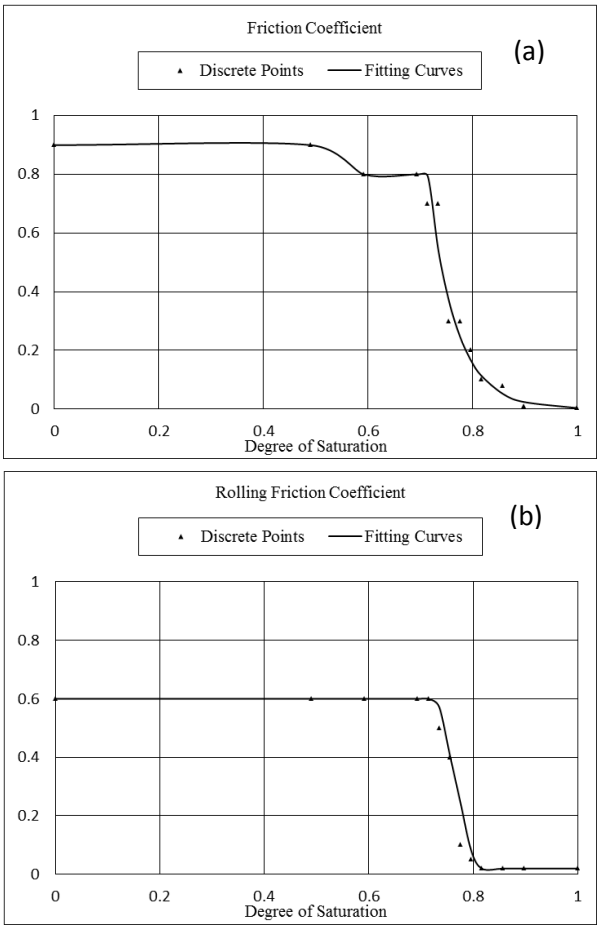

Figure 6.5 Fitting curves. (a) Friction coefficient vs degree of saturation;(b) Rolling friction coefficient vs degree of saturation

$$\text{fric} = \begin{cases} 0.9 & (0 \le DoS \le 48\%) \\ 0.8 & (48\% \le DoS \le 69\%) \\ 599492 * e\text{^}(-18.95 * DoS) & (69\% \le DoS \le 100\%) \end{cases}$$

$$\text{rfric} = \begin{cases} 0.6 & (0 \le DoS \le 71\%) \\ -8.0 * DoS + 6.45 & (71\% \le DoS \le 80\%) \\ 0.02 & (80\% \le DoS \le 100\%) \end{cases}$$

DoS: degree of saturation
fric: friction coefficient
rfric: rolling friction coefficient

Table 6.3 Coupled model input parameters for liquefaction test

	Symbol	Description	Range
Deformation parameters	$\varphi_p(\circ)$	Peak friction angle	33
	$\varphi_{cv}(\circ)$	Constant volume friction angle	32
	k_B^e	Elastic bulk modulus	5e5
	k_G^e	Elastic shear modulus	1e5
	k_G^p	Plastic shear modulus	1e5
	me, ne	Elastic bulk and shear modulus index	0.5
	np	Plastic shear modulus index	0.5
	R_f	Failure ratio	0.98
	P_A	Atmospheric pressure	100kPa
Hydraulic parameters	g_a, g_n, g_c	Empirical parameters	5.0, 2.0, -1.0
	n_{sat}	Saturation when the pores are filled with water	1.0
	n_{res}	Residual saturation when the part of water remains at high suction heads	0.0
	MC	Initial moisture content	0.5
	Poro_initial	Initial porosity	0.5
Contact model parameters	*emod*	effective modulus	1e5
	kratio	stiffness ratio	2.0
	fric	friction coefficient	0.8
	rfic	rolling resistance coefficient	0.6
	dp_nratio	normal and shear critical damping ratio	0.2
	dp_sratio	dashpot mode	3

6.3.2 Time Domain Analysis

Liquefaction is associated with a phase transition of initially solid water-saturated, loosely packed granular material into a highly viscous liquid. The phenomenon occurs when fine grain ore cargoes with sufficient amounts of moisture in their mass excited by ship motions and vibration. Under cyclic (or impulsive) loading, the material concentrates due to micro-scale particle movement, which yields a reduction of the pore space inside the soil skeleton and increases the pore-water pressure. If the water cannot be migrated by means of a drainage system, the increased pore pressure will reduce the shear strength of the granular material.

The Hexapod tests conducted by consulting firm MARIN of Australia (TWG, 2013) as shown in Figure 6.6, which showed that at high moisture contents, cracks will occur in the cargo surface. Free surface apparent in the corners of the ship hold can be shaped after shaking and a considerable compaction has occurred from the initial state. The water flows out to the bottom to form the wet base. The peak pile of cargoes turns to the flat pile, which is the typical process during liquefaction as described above.

Figure 6.6 Iron ore piles before and after a sea state test (TWG report, 2013)

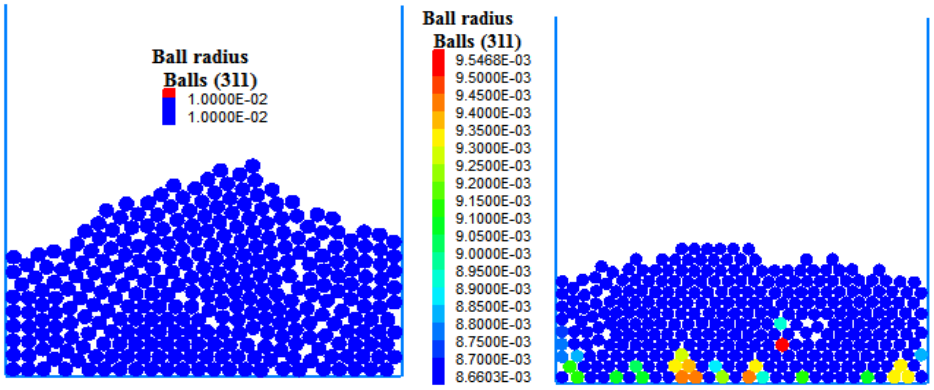

Figure 6.7 Iron ore piles before and after roll motion

The DEM liquefaction model based on PFC2D commercial software is used to simulate the whole process of liquefaction as shown in Figure 6.7. As seen from the simulation results, and compared with Figure 6.6, this model used herein can fully describe the liquefaction phenomenon from the initial state to liquefied state. The size of the particle is scaled by obtaining the elastic-plastic strain according to the stress on the particles, based on the UBCSAND model.

Roll oscillation of a 2D rectangular structure with an amplitude of 0.3rad and frequency of 1HZ is investigated to identify the interaction between cargo shift and structure motion, especially to address the liquefaction phenomenon. From Figure 6.8 shown below, the cargoes close to the wall are liquefied first (small size). When cargoes liquefy, they have enough space to move, resulting in more severe collisions. As seen in Figure 6.9, taking one ball with ID 106 in consideration, the degree of saturation increases to 100% from an initial degree of 50% at 20s. Note that some balls liquefy in a very short period of time according to the stress placed on them. At 50s, the liquefied percent reaches 100%, which means all of particles liquefy. The fluctuation force due to cargo shift on the container increases suddenly.

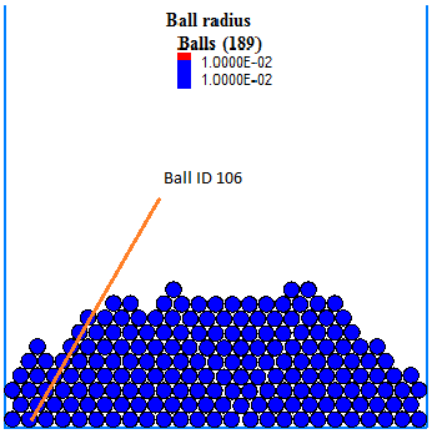

(a) Initial state of pile

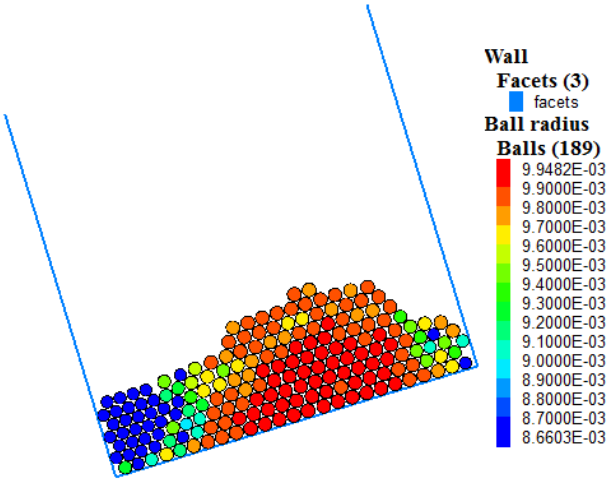

(b) Partial liquefied state

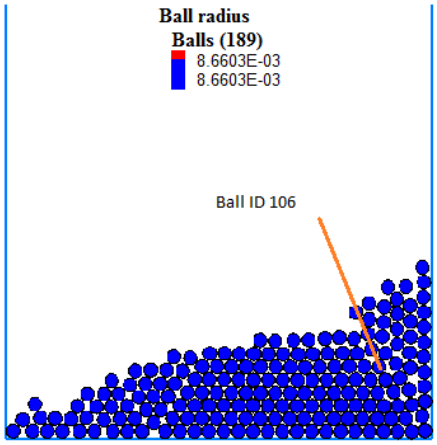

(c) Full liquefied state

Figure 6.8 Liquefaction process in roll motion

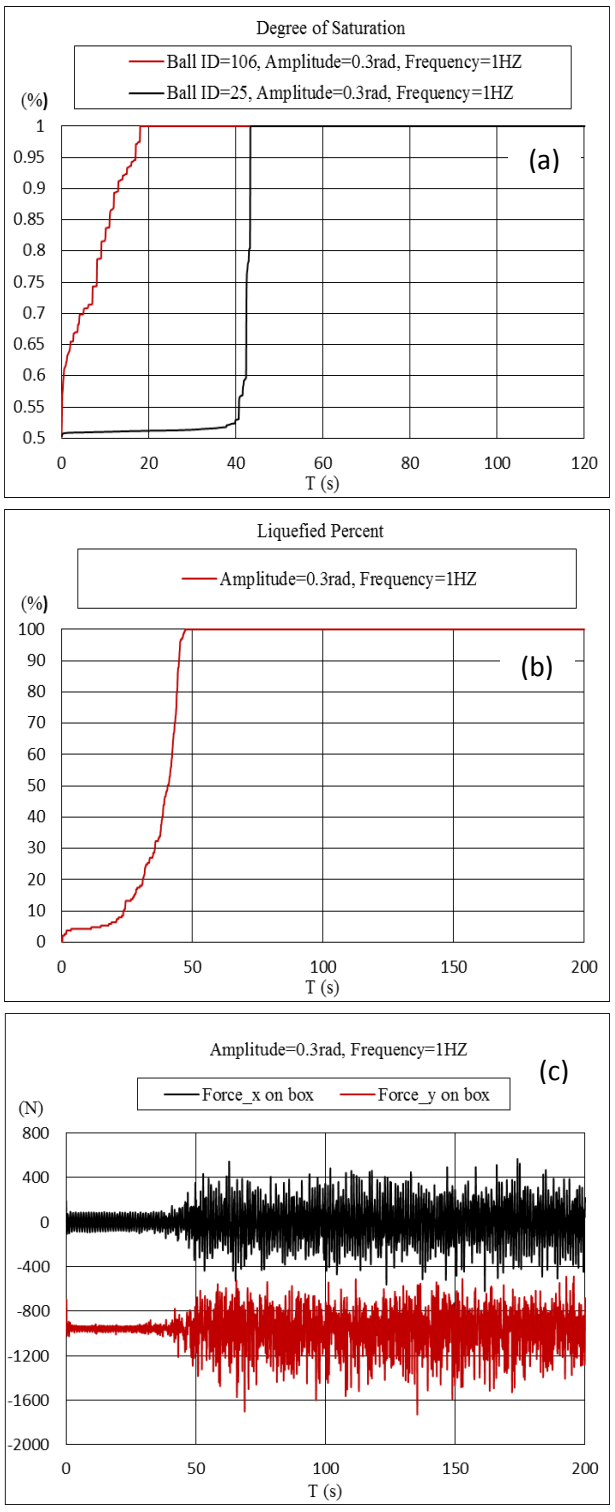

Figure 6.9 Development of (a) degree of saturation (ball id =106, 25), (b) liquefied percent, and (c) fluctuation forces on container due to cargo shift

6.3.3 Liquefaction Assessment Criterion

Liquefaction is a phenomenon in which the strength and stiffness of a soil are reduced by earthquake shaking or other rapid loading. Generally, if the effective stress of the soil decreases to zero, the soil turns liquefied as defined in soil mechanics. When compaction occurs, the water will accumulate the pore water pressure, which presses the particles apart. However, in consideration of the actual application of cargo liquefaction in a cargo ship, cargo behavior in the whole process should be captured for the coupled motion between the cargo shift and ship motion in waves. The model used in this thesis can address the problem of transitioning from unsaturated state to saturated state and fulfilling engineering application requests. From Figure 6.9, when the liquefied percentage reaches 100%, the fluctuation force due to cargo shift on the container increases suddenly and behaves like a fluid. Therefore, regarding the 100% liquefaction defined in section 4.1.3 as the liquefaction criteria is reasonable.

6.4 Dynamic Stability Analysis

Roll oscillation of a 2D rectangular structure (50cm*50cm), varying in amplitude, frequency and initial degree of saturation of cargoes, is investigated to identify the interaction between cargo shift and container motion, especially in order to predict the liquefaction phenomenon (see Figure 6.10).

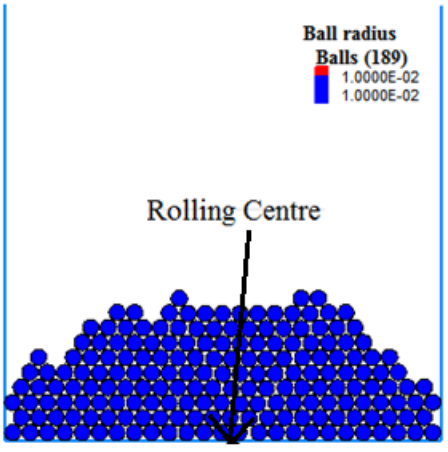

Figure 6.10 Initial appearance of cargoes for roll motion

Roll oscillation with varying initial degrees of saturation of cargoes is tested (See Figure 6.11- Figure 6.13).

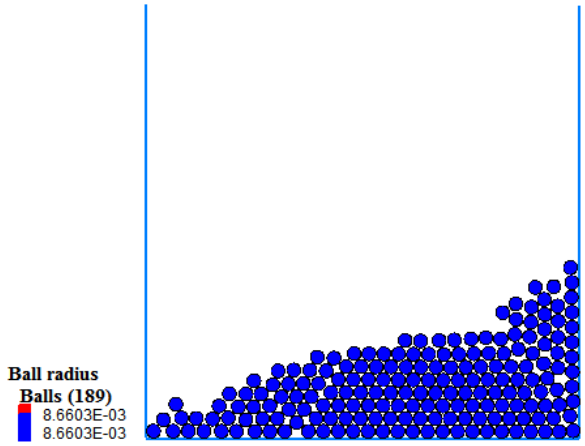

(a) Degree of saturation=0.5, Freq=1HZ, Amplitude=0.3rad

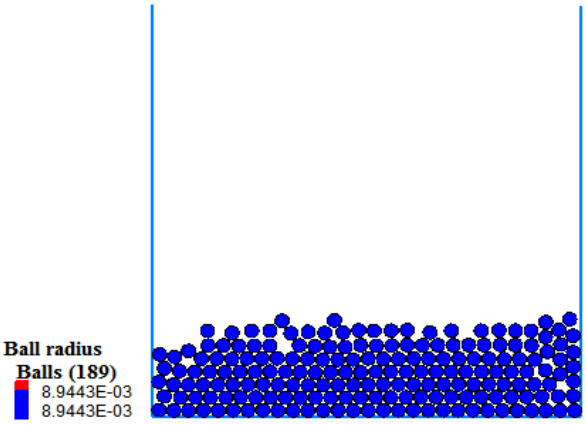

(b) Degree of saturation=0.6, Freq=1HZ, Amplitude=0.3rad

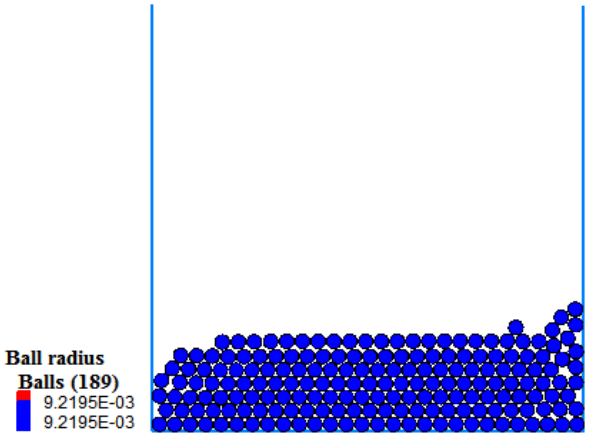

(c) Degree of saturation=0.7, Freq=1HZ, Amplitude=0.3rad

Figure 6.11 Appearance of cargoes after shaking versus initial degree of saturation

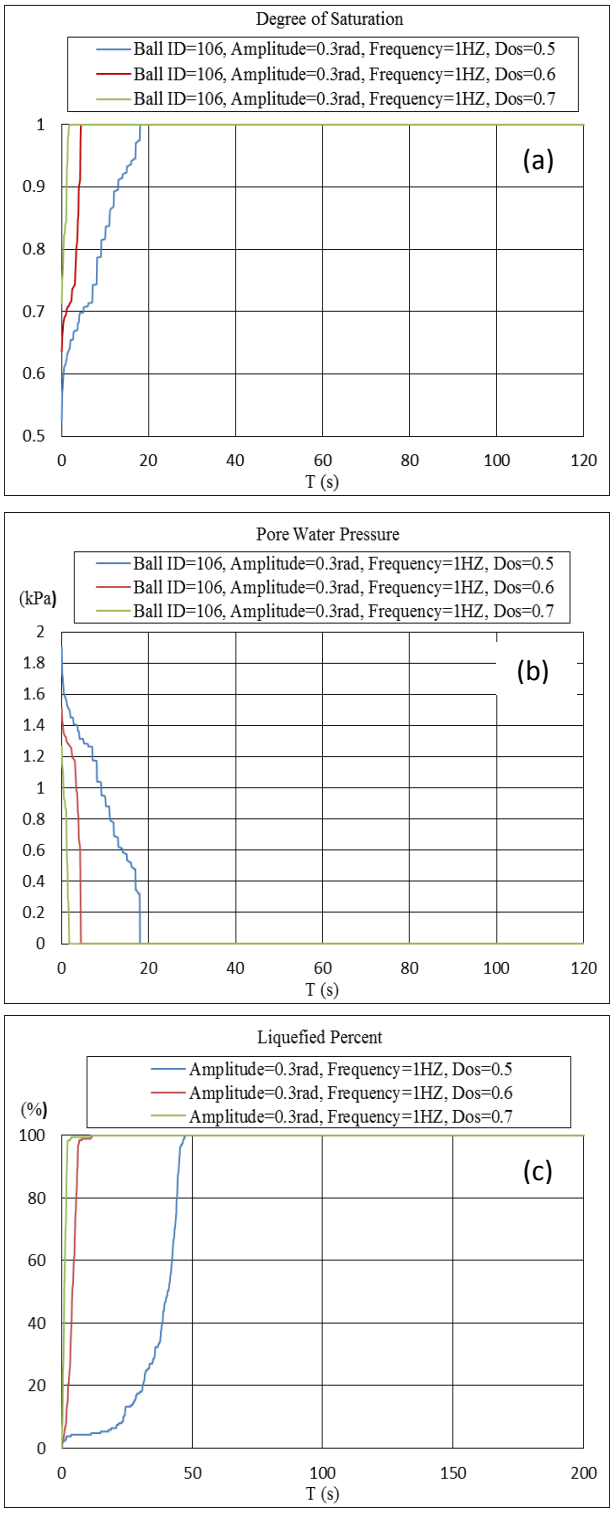

Figure 6.12 Development of (a) degree of saturation (ball id=106), (b) pore water pressure and (c) liquefied percent versus initial DoS

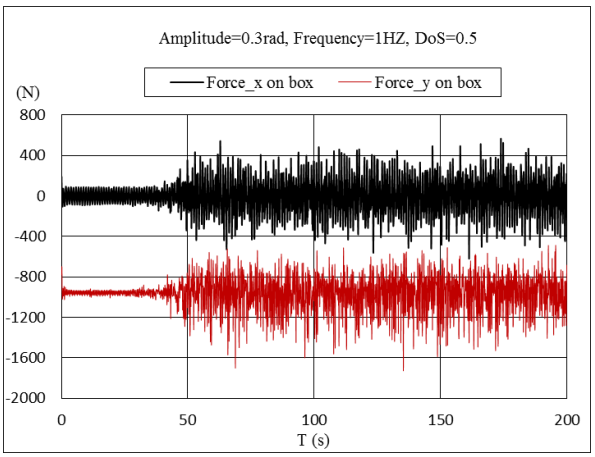

(a) Degree of saturation=0.5

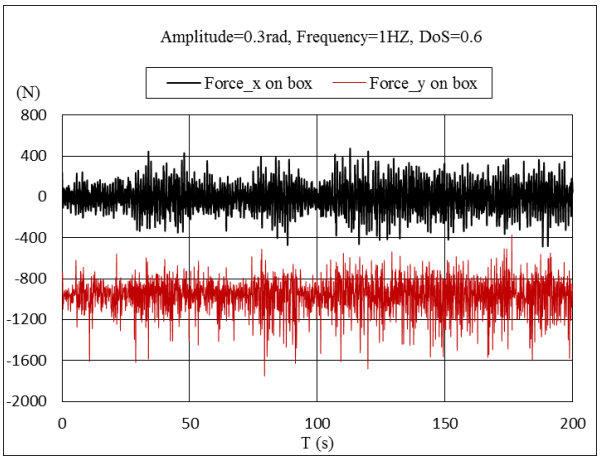

(b) Degree of saturation=0.6

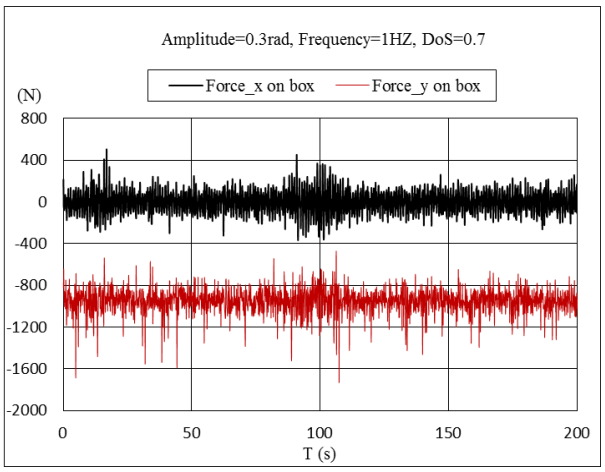

(c) Degree of saturation=0.7

Figure 6.13 Development of fluctuation force on the container due to cargo shift versus initial DoS

Following this, roll oscillation with the frequency of 1HZ and the initial degree of saturation of 50%, varying by amplitudes, is tested (see Figure 6.14 and Figure 6.15).

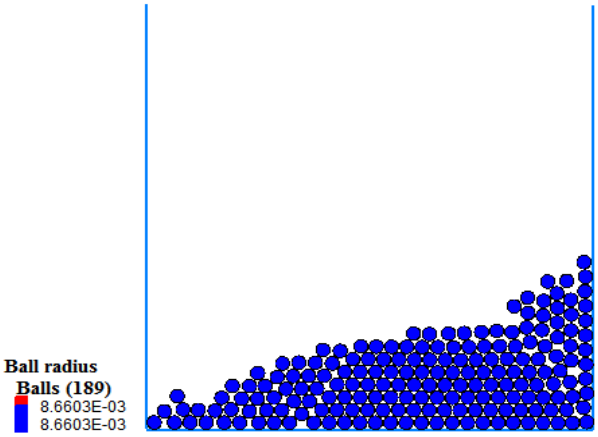

(a) Dos=50%, Freq=1HZ, Amplitude=0.3rad

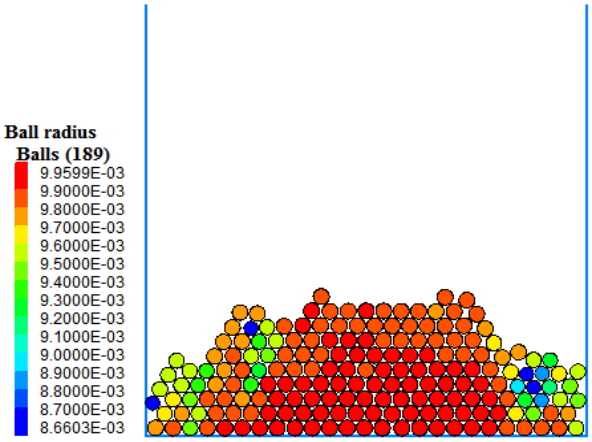

(b) Dos=50%, Freq=1HZ, Amplitude=0.2rad

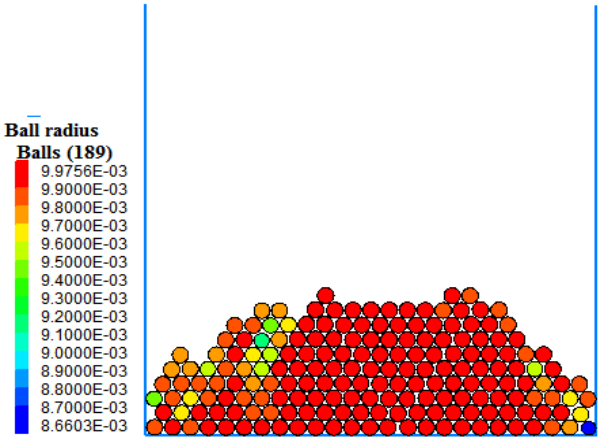

(c) Dos=50%, Freq=1HZ, Amplitude=0.1rad

Figure 6.14 Appearance of cargoes after shaking versus ampitude

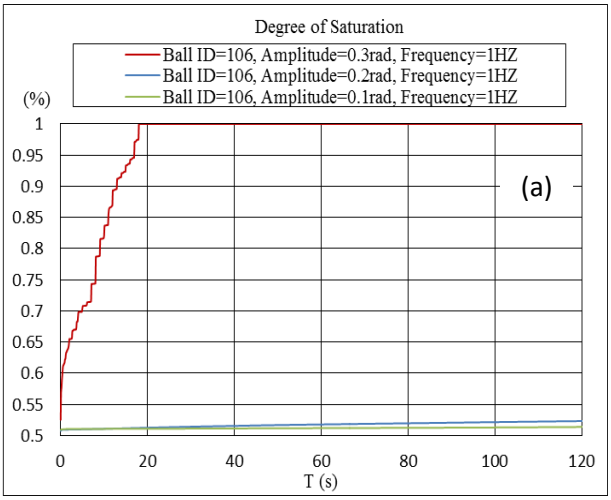
Degree of Saturation
Ball ID=106, Amplitude=0.3rad, Frequency=1HZ
Ball ID=106, Amplitude=0.2rad, Frequency=1HZ
Ball ID=106, Amplitude=0.1rad, Frequency=1HZ
(%)
1
0.95
0.9
0.85
0.8
0.75
0.7
0.65
0.6
0.55
0.5
(a)
0
20
40
60
80
100
120
T (s)

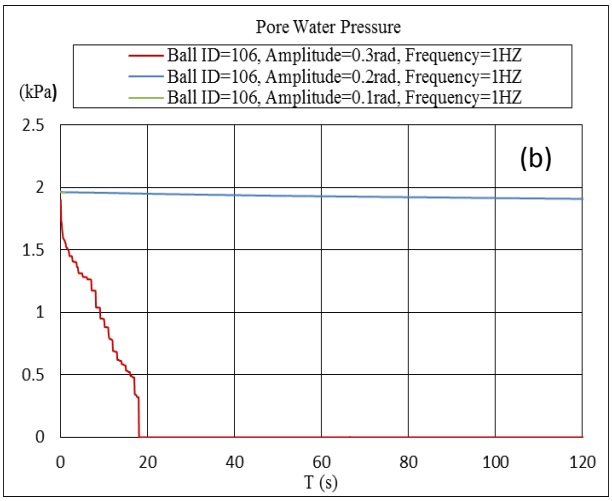
Pore Water Pressure
Ball ID=106, Amplitude=0.3rad, Frequency=1HZ
Ball ID=106, Amplitude=0.2rad, Frequency=1HZ
Ball ID=106, Amplitude=0.1rad, Frequency=1HZ
(kPa)
2.5
2
1.5
1
0.5
0
(b)
0
20
40
60
80
100
120
T (s)

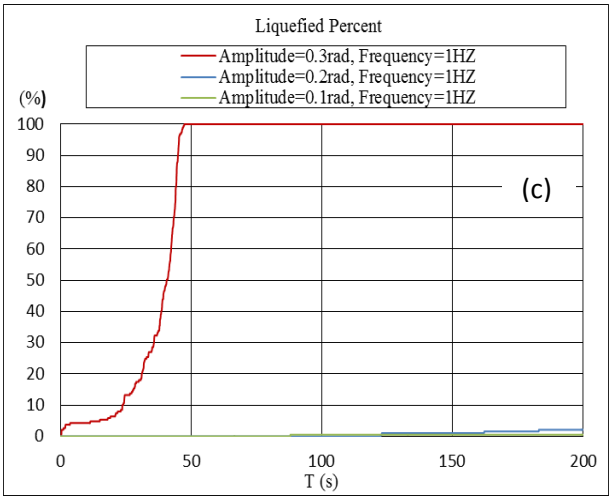
Liquefied Percent
Amplitude=0.3rad, Frequency=1HZ
Amplitude=0.2rad, Frequency=1HZ
Amplitude=0.1rad, Frequency=1HZ
(%)
100
90
80
70
60
50
40
30
20
10
0
(c)
0
50
100
150
200
T (s)

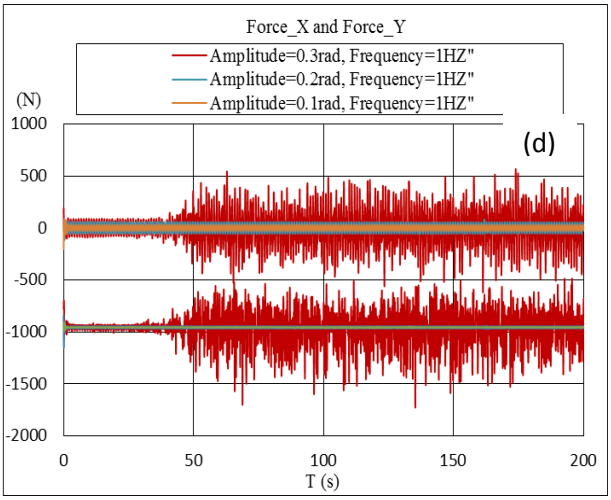

Figure 6.15 Development of (a) degree of saturation (ball id=106), (b) pore water pressure, (c) liquefied percent and (d) fluctuation force on the container versus initial amplitude

Roll oscillation with the amplitude of 0.3rad and the initial degree of saturation of 50%, varying by frequencies, is tested (see Figure 6.16 and Figure 6.17).

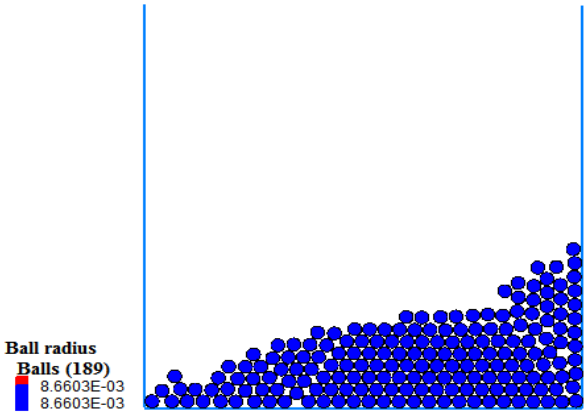

(a) Dos=50%, Freq=1HZ, Amplitude=0.3rad

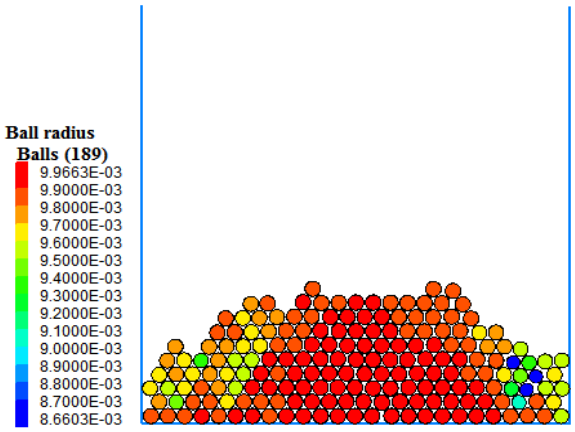

(b) Dos=50%, Freq=0.5HZ, Amplitude=0.3rad

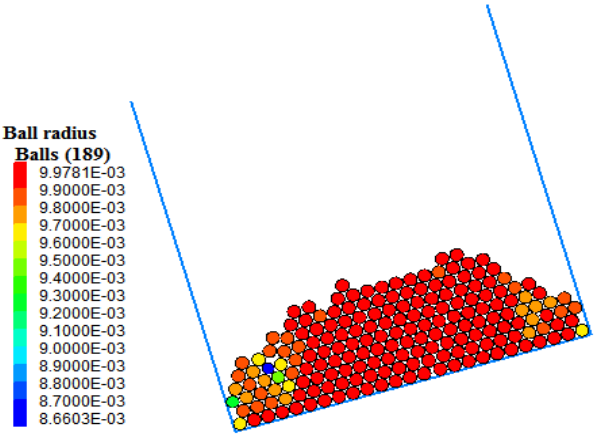

(c) Dos=50%, Freq=0.2HZ, Amplitude=0.3rad

Figure 6.16 Appearance of cargoes after shaking versus frequency

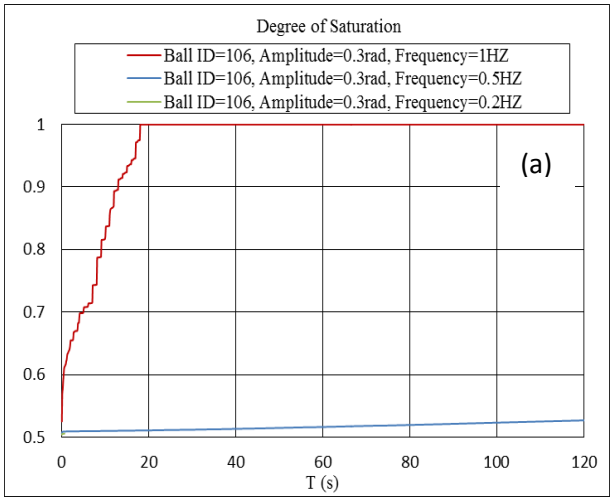

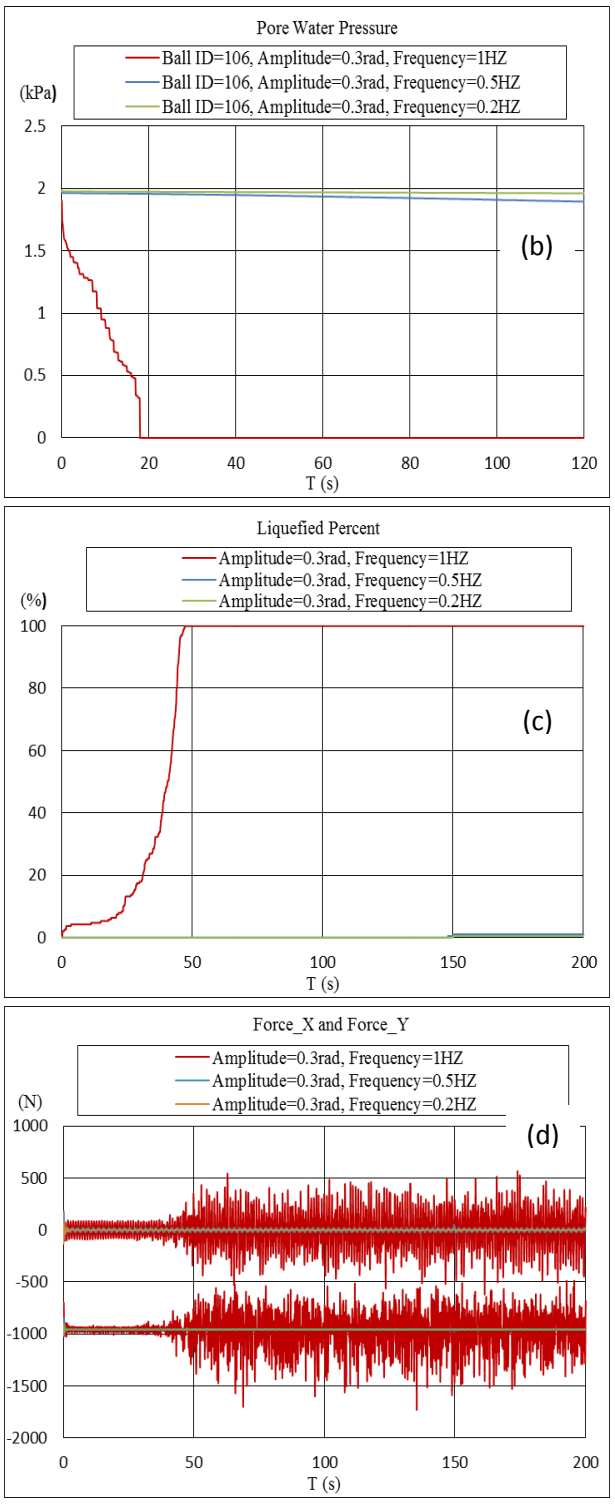

Figure 6.17 Development of (a) degree of saturation (ball id=106), (b) pore water pressure, (c) liquefied percent and (d) fluctuation force on the container versus frequency

Roll oscillation of a 2D rectangular structure (50cm*50cm) varying in amplitude, frequency and initial degree of saturation of cargoes is investigated to address the liquefaction phenomenon. It can be concluded that cargoes have a high tendency to flow with higher initial MCs of cargoes and higher frequencies and amplitudes of external loading, as discussed below:

1) As shown in Figure 6.12, the ball (ID=106) with an initial degree of saturation of 50% liquefied at 20s. While the ball with an initial degree of saturation of 60% and 70% liquefied in several seconds. According to the liquefaction model, the bulk modulus and shear modulus are small with a high level of initial degree of saturation. At the same external energy input, the cargoes with a higher degree of saturation have lower liquefaction resistance. Thus the cargoes containing a low level of degree of saturation will experience a longer time to reach a liquefied state.
2) If the amplitude and the frequency are constant, the flowability of cargoes at the initial degree of saturation of 50% is more evident than at the initial degree of saturation of 60% or 70%. The reason is that when the degree of saturation is high, the air contained in the sample is low. Therefore, it can be seen from Figure 6.13 that the radius of liquefied cargoes is larger at the degree of saturation of 50% than others. However, if under the same initial conditions, it can be seen that cargoes with a high initial degree of saturation will have large flowability.
3) As shown in Figure 6.13, cargoes with an initial degree of saturation of 50% contribute small fluctuation force on the container, as the cargoes have large shear strength to restrain cargo shift. When the cargoes reach the liquefied percentage of 100%, this causes cargoes to behave like liquid gradually. Similarly, cargo is less resistant to liquefaction with high energy input on the container (see Figure 6.14-Figure 6.17).

6.5 Conclusions

In this chapter, a DEM liquefaction model was developed to address the liquefaction phenomenon. The conclusions are summarized as:

1) The DEM combined with the UBCSABND model can effectively capture the cyclic

shear behavior, liquefaction phenomena and discrete characteristics of granular materials.

2) When the liquefied percentage reaches 100%, the fluctuation force due to cargo shift on the ship hold-shaped container will increase suddenly. Therefore, the definition of 100% liquefied cargoes in the model, regarded as the liquefaction criteria, is effective and reasonable.
3) It is concluded that the higher initial degree of saturation of cargoes, higher frequency and amplitude of the external loading on the container, leads to less liquefaction resistance of the cargoes.

Based on the assumptions presented in section 6.1, the validations were carried out to confirm the accuracy of the DEM liquefaction model. The simulation results indicate that the DEM liquefaction model can predict the liquefaction phenomenon of the cargoes after comparing with experimental data. The assumptions are the novel features of this new approach, but they need to be further validated by laboratory experiments.

Chapter 7 Ship Cargo Liquefaction in Waves

Prediction for ship response in waves needs to address two problems, including: 1) cargo flow due to cargo liquefaction, which has been addressed in Chapter 5 and Chapter 6; 2) the interaction with ship response in waves. To identify the ship response in waves due to cargo shift, a key factor is to build a numerical tank to determine the wave generation and predict the response of bodies in waves. In this chapter, regular and irregular waves are generated using the paddle wave generating method based on ANSYS Fluent commercial software. The Navier-Stokes equation, Volume of Fluid (VOF) method and dynamic meshing method are used to establish a two-dimensional wave tank with a wave-absorbing method employed to absorb the wave energy. The roll motion of a 2D rectangular structure in waves is analyzed and a CFD-DEM adapter is developed to simulate the interaction between the cargo shift and ship motion in waves. The liquefaction model in Chapter 6 is activated in the calculations.

7.1 Making Waves

7.1.1 Linear Wave

As shown in Figure 7.1, the numerical tank model includes three zones: the wave making zone, working zone, and absorption zone. The length of the wave absorption zone should be at least one times the desired wave length in order to eliminate the effect from a reflected wave. The boundary AB is set as a ‘pressure outlet’ and the others are set as ‘walls’, including the paddle OP.

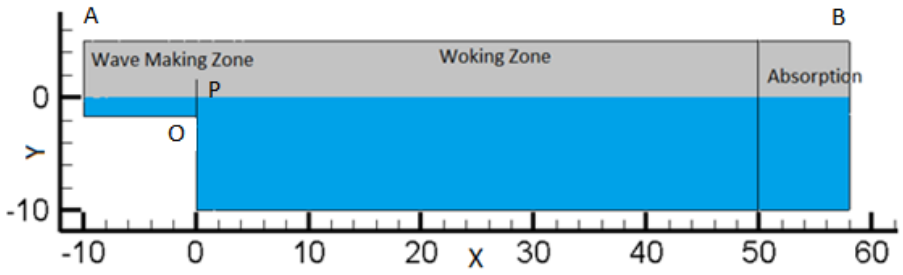

Figure 7.1 2D Numerical tank model

Figure 7.2 and Figure 7.3 shows the total mesh layout of the numerical tank and enlarged view of the mesh around the paddle. The dynamic mesh technique is used around the paddle to adapt the deformation of the mesh with triangle grids.

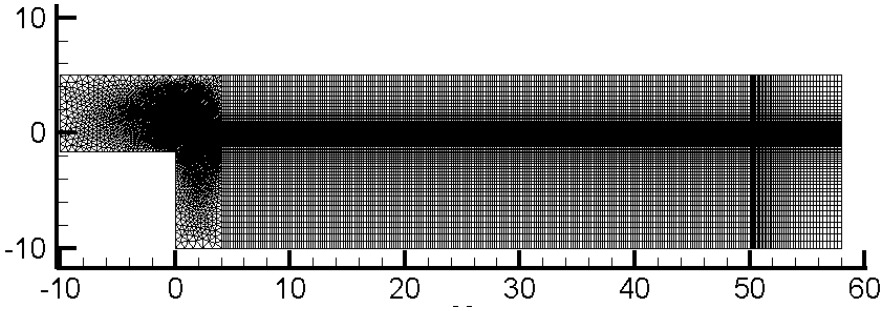

Figure 7.2 Total mesh layout

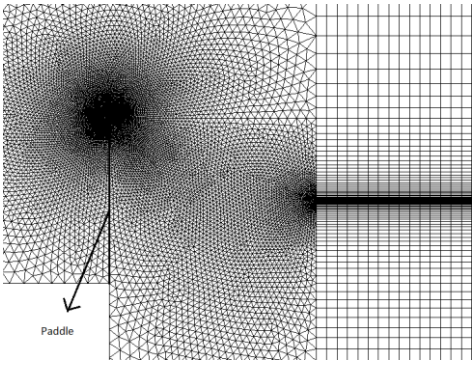

Figure 7.3 Enlarged view of mesh around paddle

Table 7.1 Parameters for making linear wave

Wave length (unit:m)	Wave height (unit:m)	Depth of paddle under water (unit:m)	Depth of numerical tank (unit:m)
8m	0.4m	1.6	10

According to the plane standing wave theory and the parameters shown in Table 7.1, the motion of paddle in this simulation is as follows:

$\theta(t) = 0.1451sin(2.7743t)$

$\dot{\theta}(t) = 2.7743 * 0.1451cos(2.7743t)$

This equation can be read by using the User Defined Function in Fluent software to control the motion of paddle based on dynamic mesh method. The regular wave is presented in Figure 7.4, and it can be seen clearly that the wave length is 8m. Based on the wave absorption theory, from x=50m to x=58m, the damping effect is obvious and the wave energy is clearly removed. As we can see from Figure 7.5, the wave surface at the probe is similar to the theoretical wave curve. Based on this method, the regular wave is generated to provide the wave condition for the coupled calculation of the response of a container due to cargo shift.

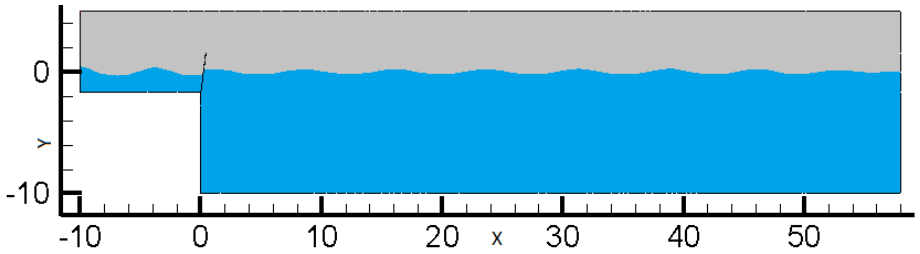

Figure 7.4 Appearance of wave surface

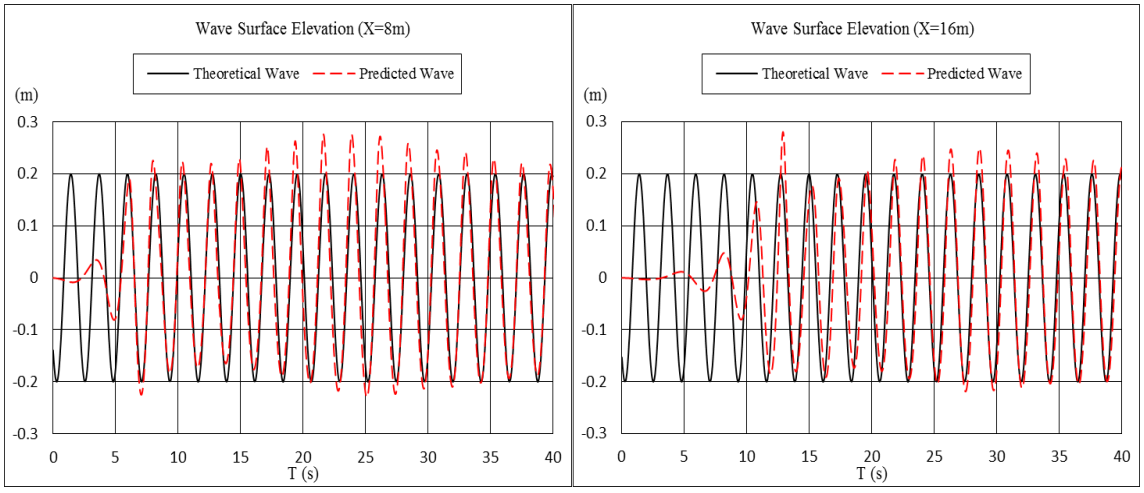

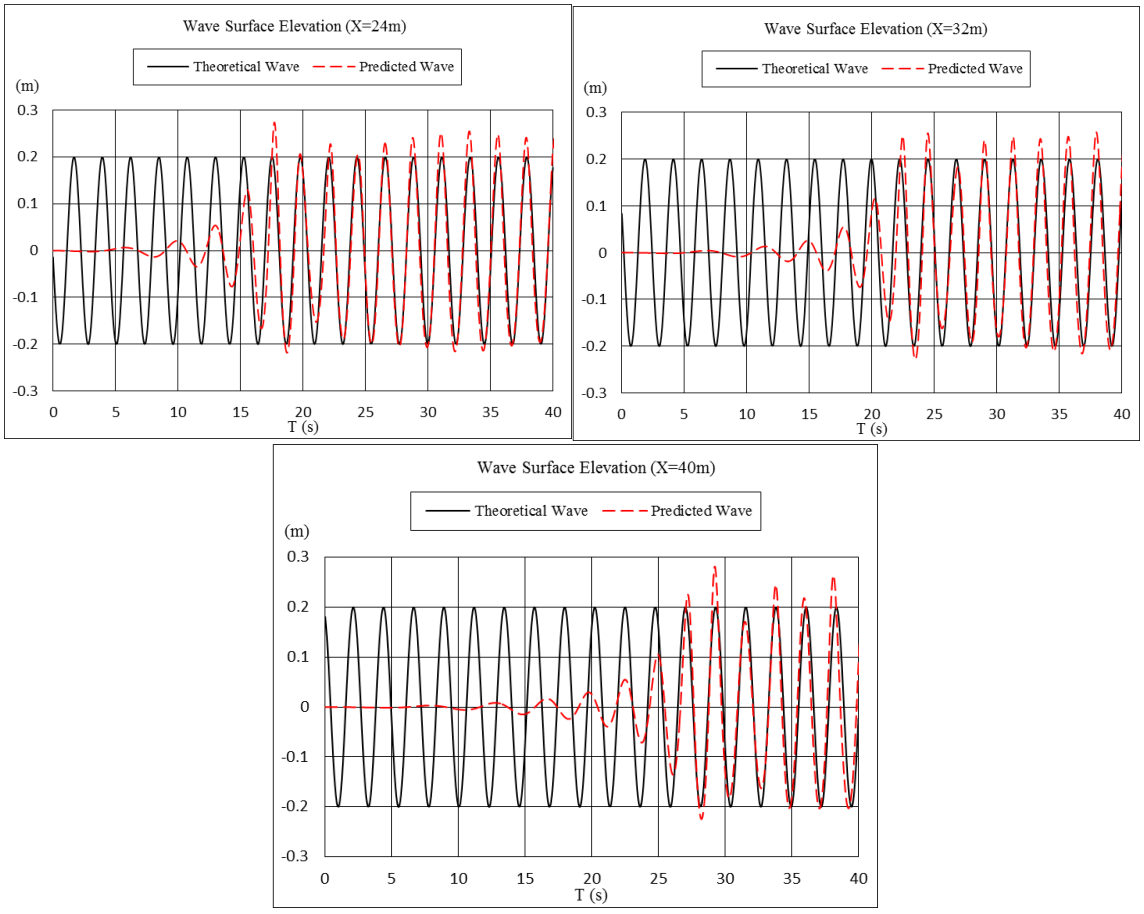

Figure 7.5 Time history curves of wave free surface (x=8m, 16m, 24m, 32m, 40m)

7.1.2 Irregular Wave

Irregular wave is generated in the numerical tank (see Figure 7.6). It can be observed from Figure 7.7 that the irregular wave is successfully built using this method.

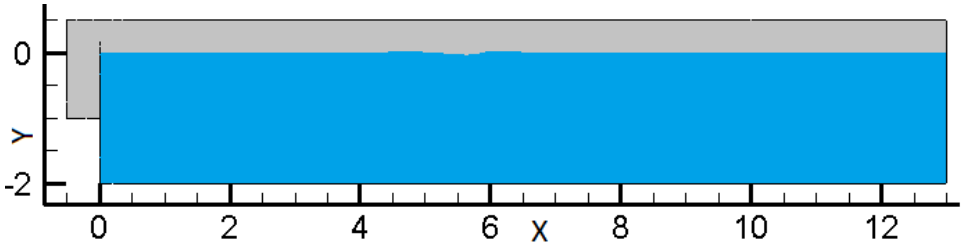

Figure 7.6 Appearance of irregular wave Surface

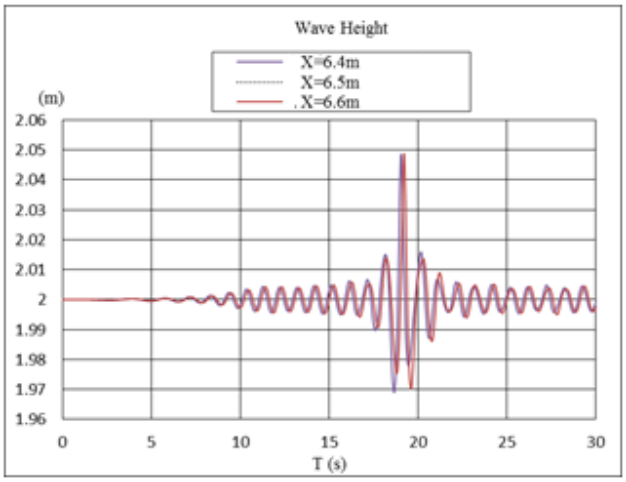

Figure 7.7 Time history curves of irregular wave height (x=6.4m, 6.5m, 6.6m)

7.2 Roll Motion in Waves

7.2.1 Regular Waves

Roll motion in waves of a rectangular structure was investigated in a wave tank at Texas A&M University (Jung, 2006) as shown in Figure 7.8 and Figure 7.9. The tank is 35m long, 0.9m wide and 1.2m deep. The structure was used to simulate a simplified barge in the beam sea condition. The rectangular structure with the dimensions of 0.9m long, 0.3m wide (B) and 0.1m high was used as a scaled down barge in the experiments as shown in Table 7.2. The structure floated at a draft that equals one-half of its height. The moment of inertia of the actual mass of the structure is 0.236 $kg \cdot m^2$.

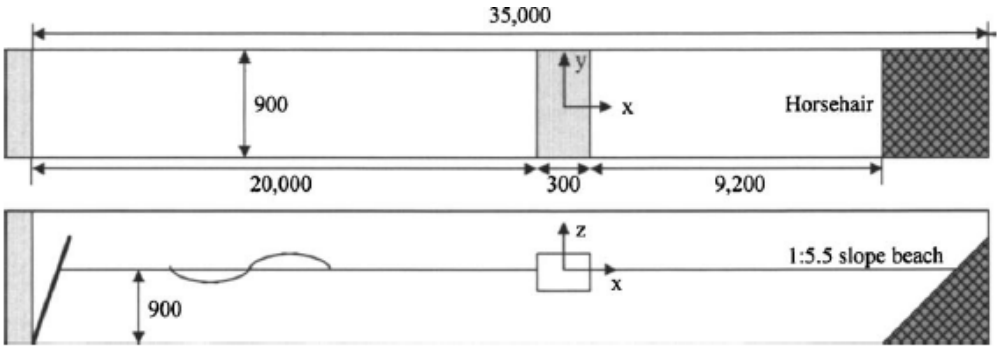

Figure 7.8 Sketch of experimental wave tank (unit: mm)

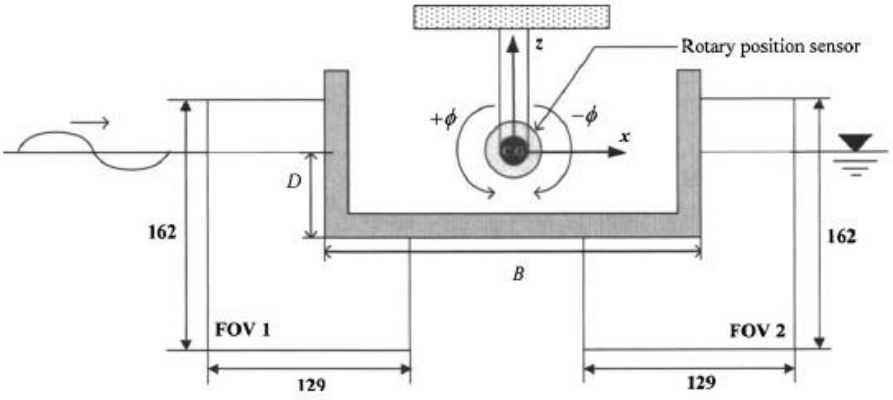

Figure 7.9 Setup of free-rolling structure with coordinate system and particle image velocimetry fields of view (unit: mm)

Table 7.2 Experimental conditions

Tank	Long	35m
	wide	0.9m
	deep	1.2m
rectangular acrylic structure	Long	0.9m
	wide	0.3m
	high	0.1m

Based on the experimental conditions, first, the roll decay is conducted in the calm water condition. We can see the profile of computation domain and mesh distribution in the two-dimensional numerical tank in Figure 7.10 and Figure 7.11. The mesh interface technique is used in the roll motion for the data transfer. For the roll decay test, the structure is initially inclined with an angle of 15 degrees and then released. The roll motion decays after each cycle due to the damping effect as shown in Figure 7.12. Comparing with the experimental data, the results shows good agreement.

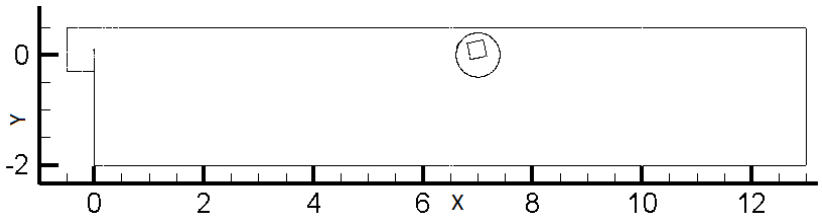

Figure 7.10 Profile of computation domain

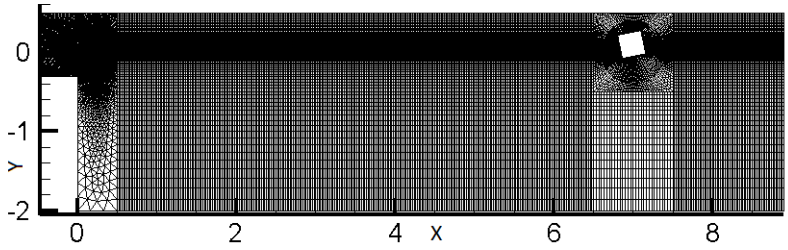

Figure 7.11 Mesh distribution

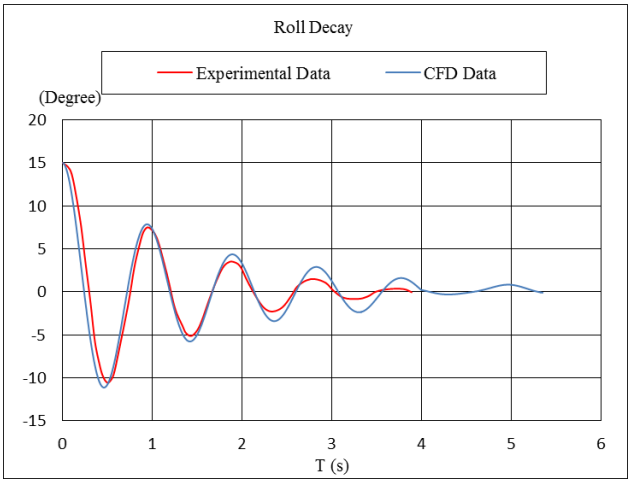

Figure 7.12 Time history of roll angle in roll decay test

The dynamic response of the barge-like structure under regular waves is tested in the numerical tank. The wave parameters are shown in Table 7.3. The gravity centre is set at the location of (7m, 0m) in Figure 7.13. The response of the structure in the regular waves is demonstrated by examining roll angle at the natural frequency. As shown in Figure 7.14, the numerical results show good agreement with the experimental data.

Table 7.3 Parameters of linear wave for roll motion

T (s)	ω (rad/s)	λ (m)	H (m)	kA
0.93	6.76	1.35	0.027	0.0628

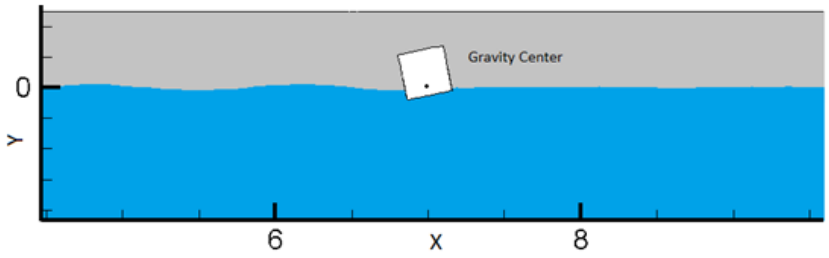

Figure 7.13 Profile of free water surface in linear wave

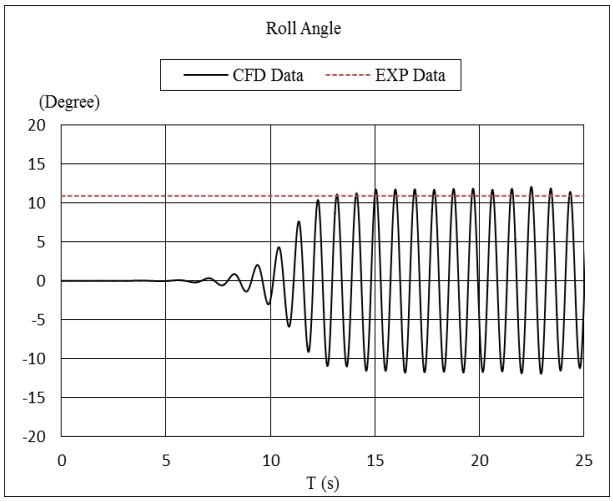

Figure 7.14 Time history of roll angle in linear wave (Kwang Hyo Jung, 2006)

7.2.2 Irregular Waves

The roll motion of the 2D rectangular structure in irregular waves is simulated in the numerical tank (see Figure 7.15). The rectangular structure is placed at x=6.5m according to the results in section 7.1.2 (see Figure 7.7). The roll angle of the structure is identified. The coupled interaction between the incident waves and the structure results in a large roll angle, as shown in Figure 7.16. The large roll angle may cause extreme danger and capsize the ship, especially for containers with liquefied cargoes since when the cargo liquefies, it behaves like a non-Newtonian fluid. With the irregular waves, the cargoes may flow to one side and not flow back quickly, which may cause the loss of ship vessels, as discussed in section 4.2. Therefore, the issue of how to predict and control cargo liquefaction, especially in irregular waves, and how to increase ship stability needs to be addressed scientifically.

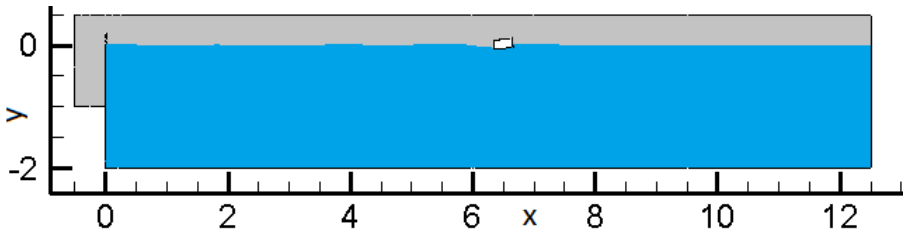

Figure 7.15 Profile of free water surface in irregular wave

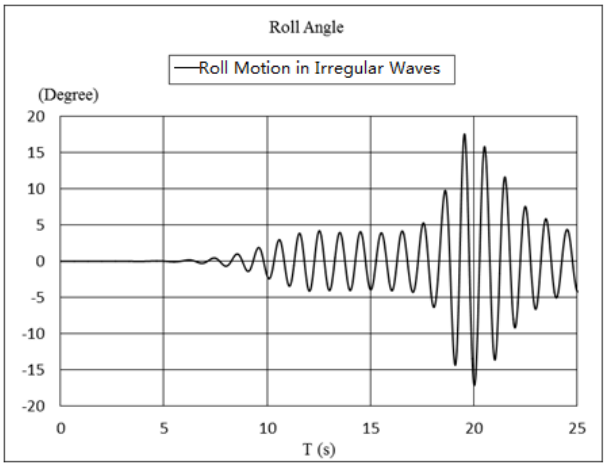

Figure 7.16 Time history of roll angle in irregular wave

7.3 CFD-DEM Adapter for Coupled Calculation

Cargo shift due to liquefaction has great influence on ship stability, especially in wave conditions. In Chapter 6, PFC software has been used to calculate cargo shift due to liquefaction, while ANSYS Fluent software can calculate the free 6-DOF motion in waves. Therefore, an adapter is developed to combine PFC software with ANSYS Fluent software, which allows for the transferring of data during the coupled calculations without any changes in the source of the simulation code.

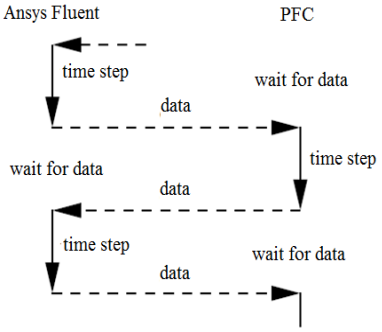

Figure 7.17 Algorithm for solution of coupled calculation for liquefaction

The algorithm of the adapter is sketched in Figure 7.17, which shows that the ANSYS Fluent firstly makes a calculation, sends data to the PFC, which then calculates during the same time step and sends data back to ANSYS Fluent and so on. Running a co-simulation requires the following steps:

(1) Preparation of Model Files: Before starting a co-simulation, each domain must be prepared separately. For ANSYS Fluent software, the mesh, turbulence model, materials, boundary condition and patch domain for water phase must be prepared first. For PFC software, the preparation process includes the distribution of cargoes and the initialization of gravity and properties of each particle.

(2) Coupling Process: The ANSYS Fluent software calculates firstly to obtain an angular velocity of the container or ship in waves, and then sends it to the PFC software code. Thus the corresponding moment on the container due to cargo shift will be obtained. This moment will transfer to ANSYS Fluent, and so on until the appearance of wanted data, as seen from Figure 7.18.

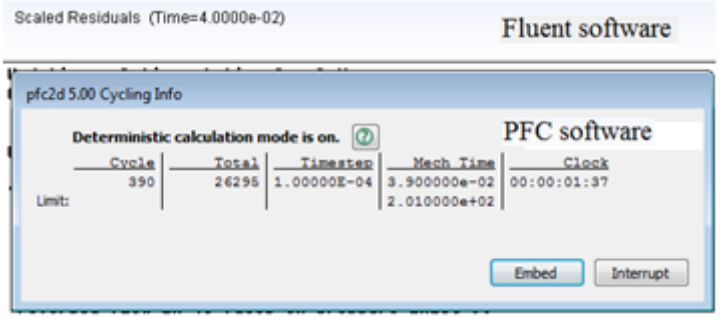

Figure 7.18 Adapter interface of coupled simulation

To validate the coupled model, a roll motion of a 2D rectangular structure containing granular materials in waves is conducted based on ANSYS Fluent software combined with PFC software. The wave parameter is shown in Table 7.3. As reflected in Figure 7.19, the container in PFC software and the container in ANSYS Fluent software keep the same response. We can see from Figure 7.20 that the ball (ID=106) gradually liquefies from the initial degree of saturation of 50%. Meanwhile, pore water pressure of this ball gradually decreases to 0kPa according to the UBCSAND liquefaction model. Under the condition of a real sea state, the cargo needs to experience a slow process to liquefy due to the low

energy input. 1.9% of the cargoes liquefy at the time 25s, which can be regarded as no liquefaction. The interaction between the cargo displacement and container motion is not evident and the maximum roll angle is kept at the level of 10 degrees.

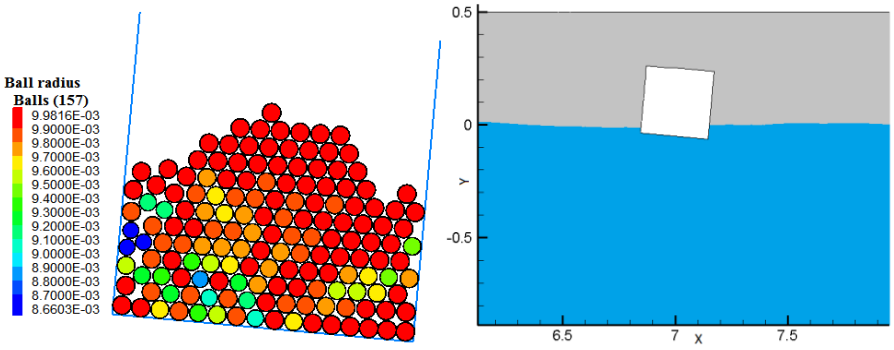

Figure 7.19 Appearances of the co-simulation at T=25s

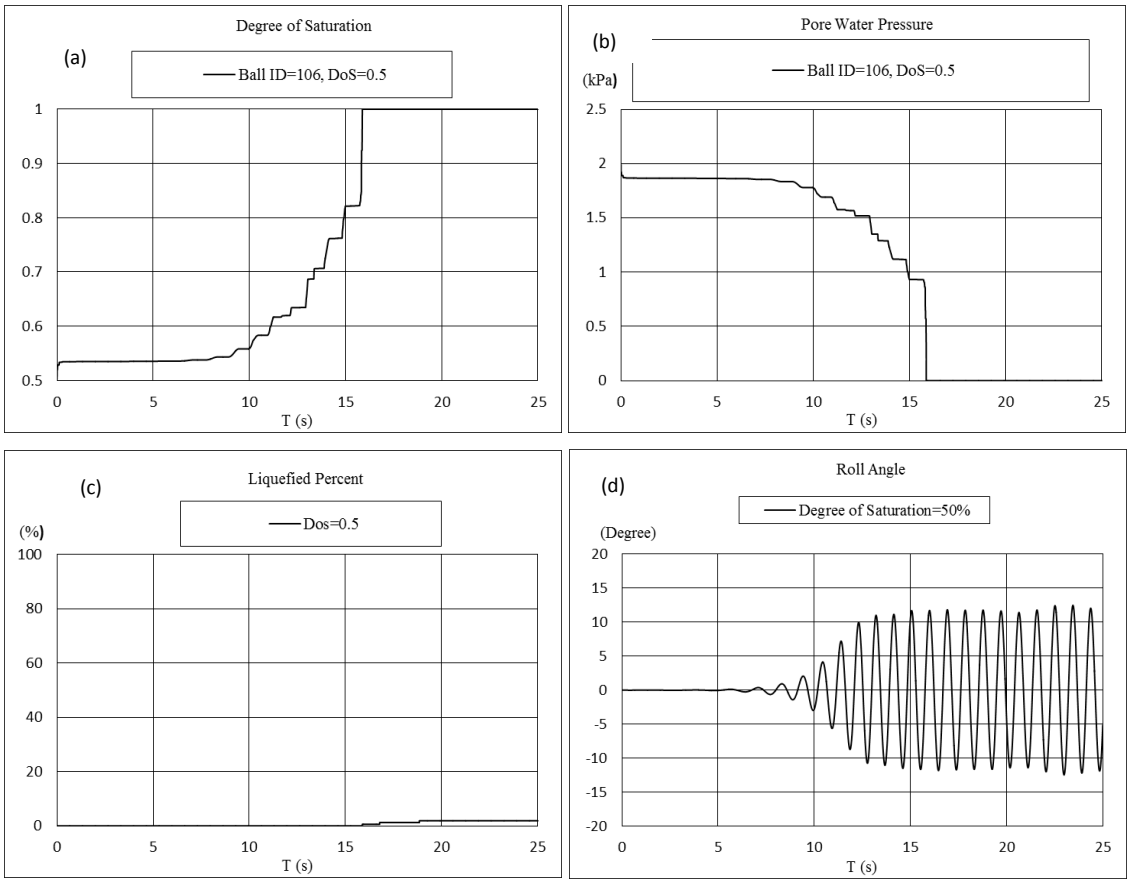

Figure 7.20 Time history curves of (a) Degree of saturation. (b) Pore water pressure. (c) Liquefied percent of cargoes. (d) Roll angle of the container

7.4 Numerical Validation

Numerical validation includes two parts: CFD numerical validation and DEM numerical validation. CFD numerical validation focuses on the sensitivities of grid size and time-step size. DEM numerical validation emphasizes the sensitivities of particle numbers and time-step size. In addition, coupled motion in waves based on the CFD-DEM adapter will be simulated, to identify the sensitivities of particle numbers.

7.4.1 Mesh Quantities and Time-step Size

Based on the validation studies of making waves in section 7.1 and section 7.2, additional validation work with special emphasis on the sensitivities of grid size and time-step size is conducted. The computational domain size is exactly the same as what is shown in Figure 7.1.

For the grid dependence study, a time step of 0.001s and three meshes are used. Special attention to the mesh near the free surface in the working zone is considered. It takes 5.4, 6.6 and 9.3 CPU hours to finish 40s simulation time on coarse, medium and fine grids, respectively. The comparisons of numerical results are shown in Figure 7.21a. It is apparent that the results, as calculated using different grids, are in good agreement. For the time-step size dependence study, three steps with coarse mesh are listed in Table 7.4. It takes 5, 5.4 and 14.6 CPU hours to finish 40s simulation with large, medium and small time steps, respectively. The comparison of computed results is shown in Figure 7.21b. It is apparent that the results of the time history curves of wave free surface (x=24), computed with the three time steps, are nearly identical. Considering an increased computing time, as listed in Table 7.4, the coarse grid and the time-step size of 0.001s is used in the following simulations.

Table 7.4 Summary on particle size, time-step size and computing time (CFD)

Mesh	Overall cells	Calculation time	Time-step size	Simulation time (1 processor)
Coarse	47144	40s	0.001s	5.4 hours
Medium	72694	40s	0.001s	6.6 hours
Fine	111788	40s	0.001s	9.3 hours
Coarse	47144	40s	0.0008s	5 hours
Coarse	47144	40s	0.0005s	14.6hours

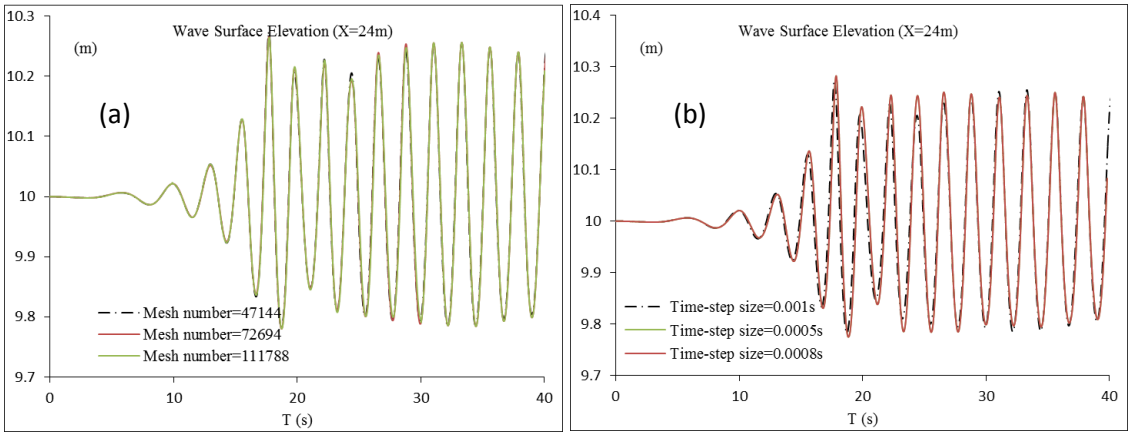

Figure 7.21 Time history curves of wave free surface (x=24m). (a) Mesh number. (b) Time-step size

7.4.2 Particle Size and Time-step Size

A prescribed sway oscillation test is conducted to identify the sensitivities of the particle size and time-step size in PFC software. The computational model of sway oscillation test is the same as that shown in section 5.4.1. Details of overall particle size and time-step size are listed in Table 7.5. The same mass of cargo with 201.06kg is applied in the simulations and the density of the particle is 2500kg/m^3. The time history curves of the fluctuation force on the container and the gravity center in Figure 7.22 and Figure 7.23 indicates that the results on different particle numbers and different time-step sizes show

little difference, which demonstrates that PFC software shows good computational stability. The fluctuation force on the container and the gravity centre of cargoes with the particle numbers of 2844 and the time-step size of 0.0001s during the oscillation test almost coincide with those with the particle numbers of 256 and the time-step size of 0.001s. Considering an increased computing time, as list in Table 7.5, the time-step size of 0.0001s is used in the following simulations and the particle size is dependent on the situation.

Table 7.5 Summary on particle size, time-step size and computing time (DEM)

Radius	Particle number	Calculation time	Time-step size	Simulation time (1 processor)
0.01m	256	40s	0.0001s	8 minutes
0.005m	1024	40s	0.0001s	20 minutes
0.003m	2844	40s	0.0001s	68 minutes
0.005m	1024	40s	0.0005s	18 minutes
0.005m	1024	40s	0.001s	15 minutes

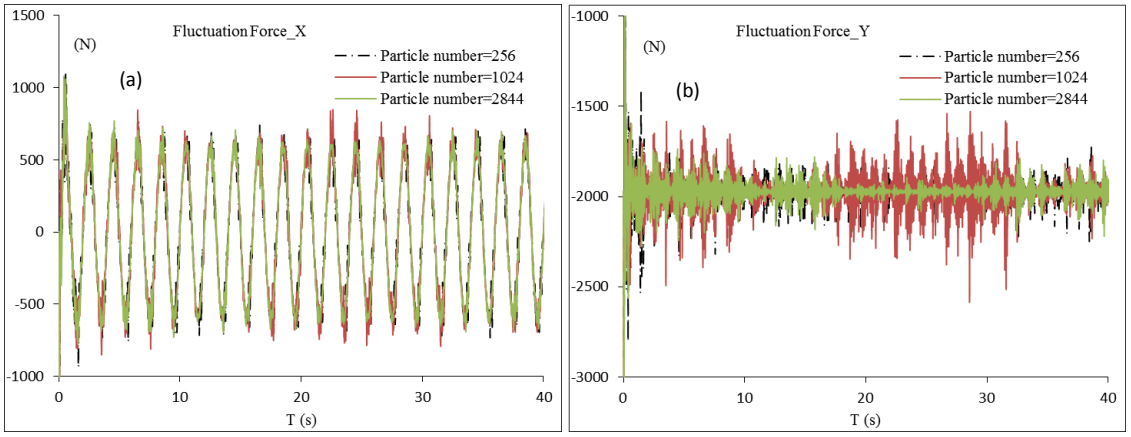

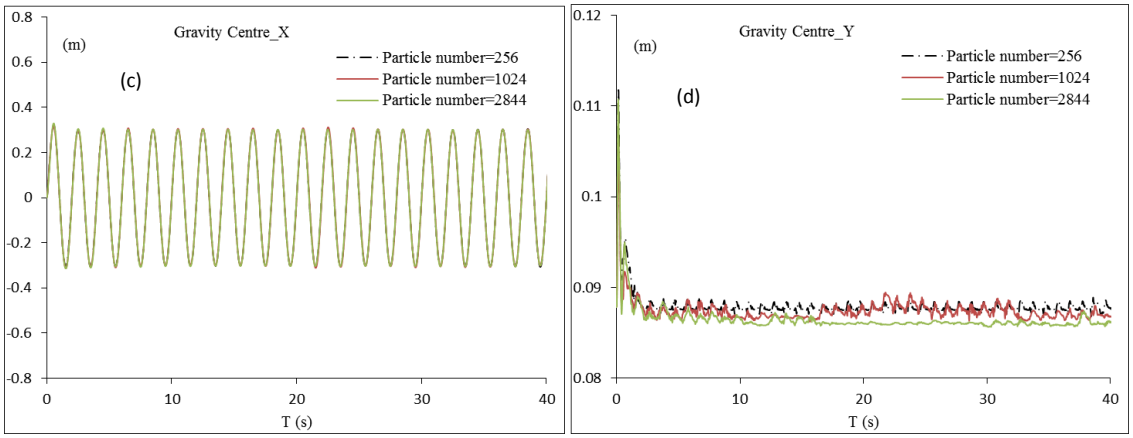

Figure 7.22 Fluctuation force and gravity centre of cargoes varying from particle number

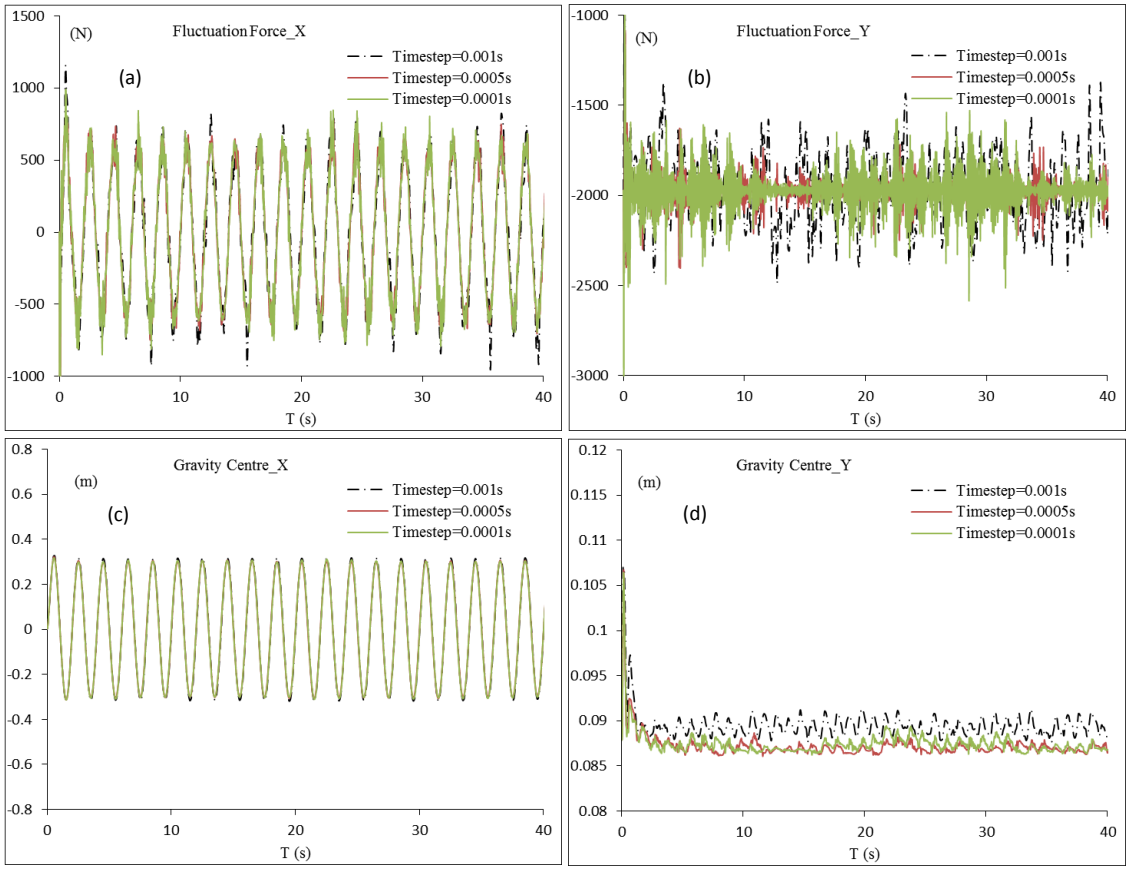

Figure 7.23 Fluctuation force and gravity centre of cargoes varying from time-step size

7.4.3 Coupled Motion Test in Regular Waves

A coupled motion test is conducted to identify the sensitivities of particle size in PFC software. The rectangular structure with dimensions of 0.3m long and 0.3m high, partially

filled with moist bulk cargo is used in the simulations (Figure 7.24). The structure is floated at a draft that equals one-sixth of its height. The moment of inertia of the actual mass of the structure is 0.236 Kg. m^2. Details of overall particle size are listed in Table 7.6. The same mass of the cargo with 14.988 kg is applied in the simulations. The density of particles is 1642.865 kg/m3 and the MC is 49%. The gravity centre is set at the location of (0m, 0m). The structure is free to respond only in the roll direction under an external excitation owed to linear waves, with a frequency of 5.932 rad/s and wave length of 1.75 m. The adapter coupling ANSYS Fluent software and PFC software, developed in section 7.3, is used to simulate the interaction between cargo movement and ship motion, which allows for the transferring of data during the coupled calculations without any changes in the source of the simulation code.

The time history curves of the roll angle of the container and the gravity centre of the cargo in Figure 7.25 indicates that results on different particle numbers show little difference. It takes 14.6, 15 and 23 CPU hours to finish 35s simulation time on coarse, medium and fine particle numbers, respectively. To maintain the same mass of the cargo, the initial gravity centre of the cargo is different, resulting in minor variations for the roll angle of the container. The selection of the particle size depends on the specific situation.

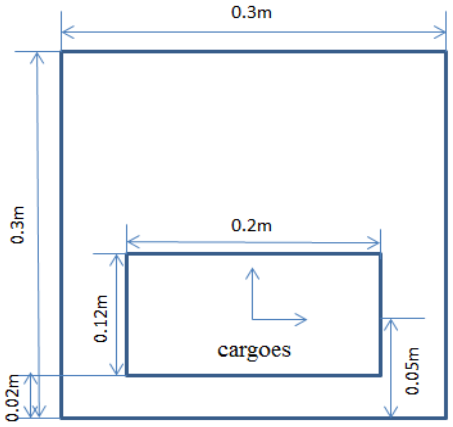

Figure 7.24 2D rectangular structure

Table 7.6 Summary on particle size, time-step size and computing time (CFD-DEM)

Radius	Particle number	Calculation time	Time-step size	Simulation time (1 processors)
0.0025m	464	35s	0.0001s	14.6 hours
0.002m	726	35s	0.0001s	15 hours
0.0015	1291	35s	0.0001s	23 hours

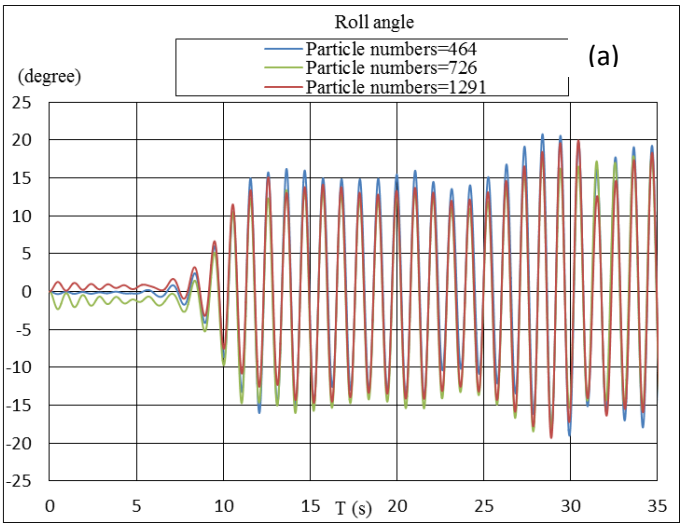

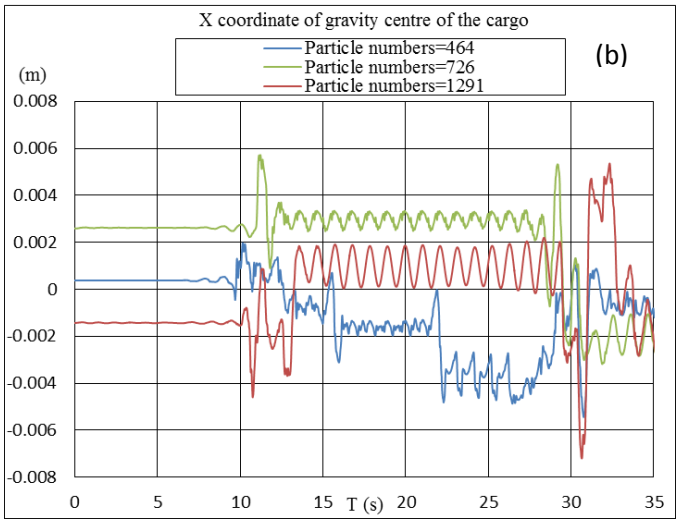

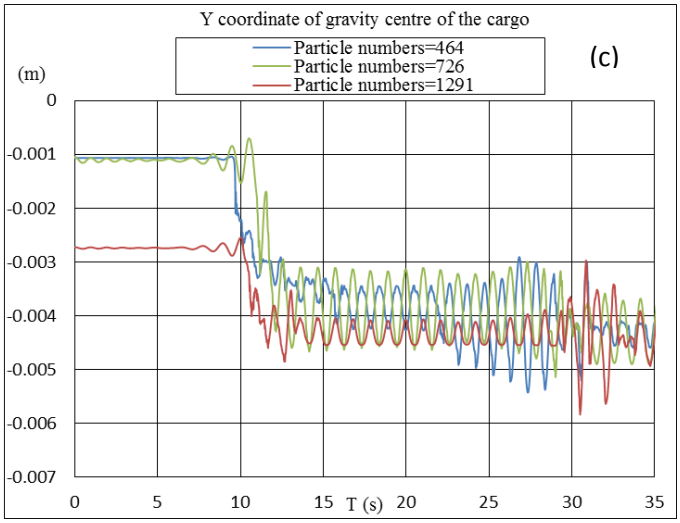

Figure 7.25 Roll angle and gravity centre of the cargo varying from particle number

7.5 Cargo Liquefaction Assessment in Waves

A parametric investigation is undertaken to identify the key parameters that trigger cargo and ship instabilities. On the XY plane appears 726 particles with the density of 1642.865kg/m3 and the radius of 0.002m. Two cases are carried out for the purpose of determining the effect of shifting cargo on the structure. The first is to change the moisture content of the cargo with the wave amplitude fixed at 0.02 m and the frequency at 6.75 rad/s (case 1). The second is to change the wave frequency with moisture content fixed at 49% and amplitude at 0.02m (case 2). Figure 7.26 shows the state of the cargo inside the structure in waves. The key findings are as follows:

a) Case 1: The maximum roll angle of the structure is approximately 18° at the moisture content level of 49%, which shows that the cargo has a high probability to flow with higher initial MCs (Figure 7.27a). The development of the roll angle at the MC level of 37% and the MC level of 40% is almost the same. This means that the roll motion of the structure is not affected by the displacement of the cargo containing low moisture content. From the development of the mass centre of the cargo in Figure 7.27b and Figure 7.27c, the cargo shows no shifting for a MC of 37% and 40%. On the other hand, for a MC of 49% and due to the low friction coefficient between particles, the cargo shows large flow-ability. Indeed, the moment due to cargo shift on

the structure affects the roll response of the structure.

b) Case 2: For the structure itself, the resonant frequency is 6.75rad/s. Therefore, for the wave frequency above or below the resonant frequency, the response of the structure is not obvious (Figure 7.28a). Especially for the wave frequency values of 5.93 rad/s, the peak roll angle is no more than 5°. From Figure 7.28b and Figure 7.28c, we see that at a wave frequency of 7.85rad/s, the phase of the cargo's displacement opposes that of the structure, and thus the overall motion is reduced.

c) For a MC of 49% and resonant frequency, the cargo has shown the shifting phenomenon. The X coordinate of the mass centre of the cargo fluctuates around the balance position. However, due to the limited space of the structure along the transverse direction and the small roll angle, the displacement of the cargo has been restricted slightly.

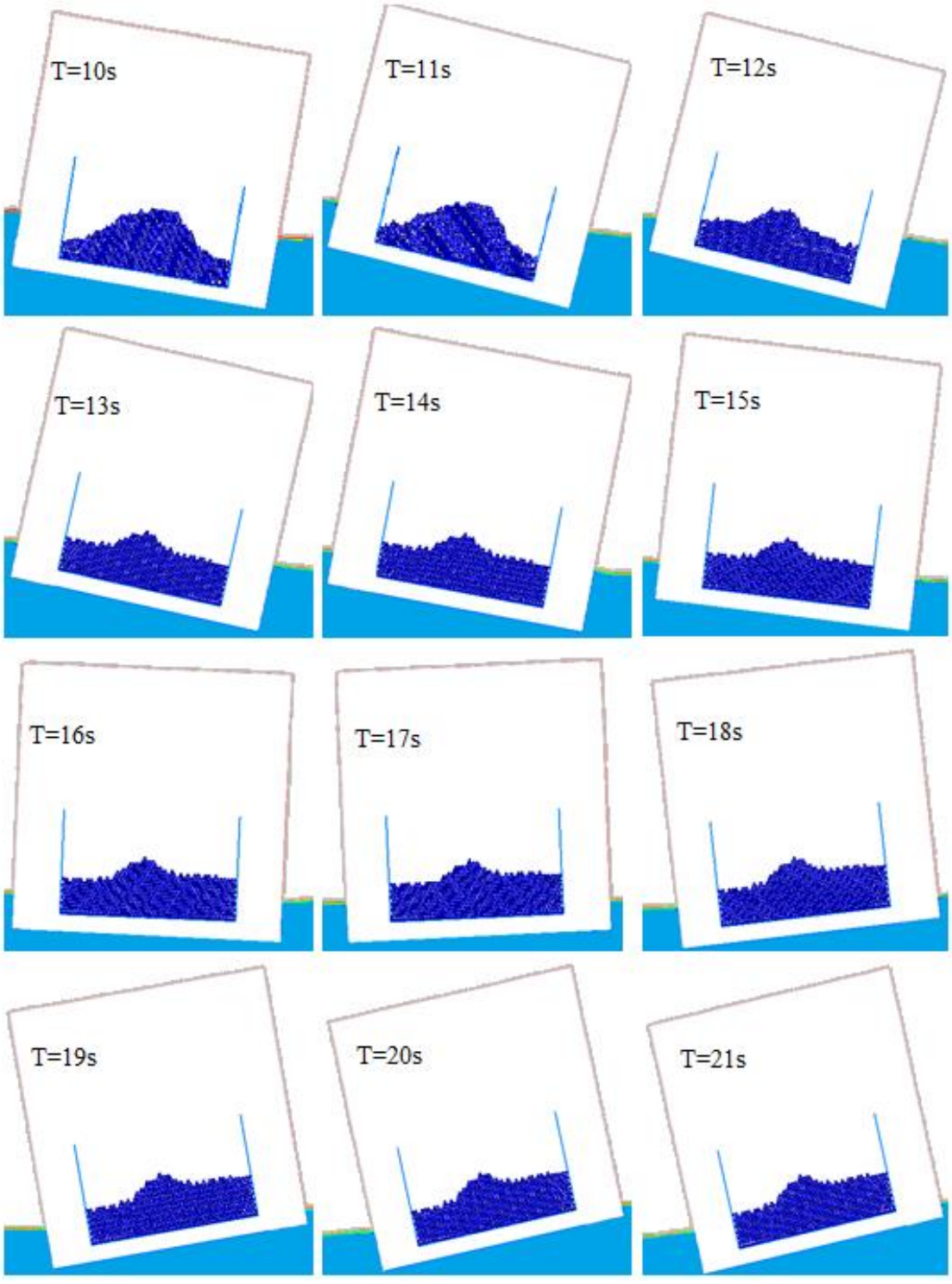

Figure 7.26 State of the cargo inside the hold during the coupled motion

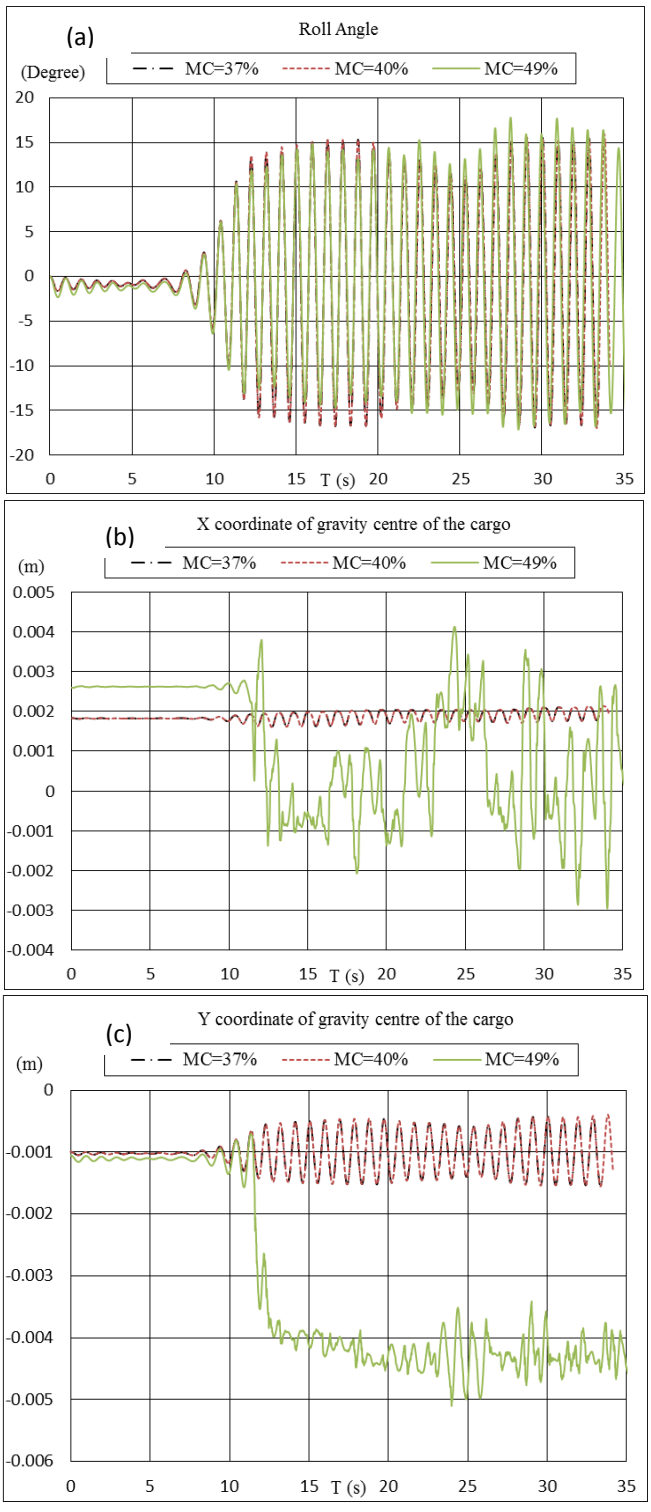

Figure 7.27 Roll angle of the container and mass centre of the cargo. The wave apmlitude is fixed at 0.02m, the frequency is fixed at at 6.753rad/s and the MC is varied as 37%, 40% and 49%

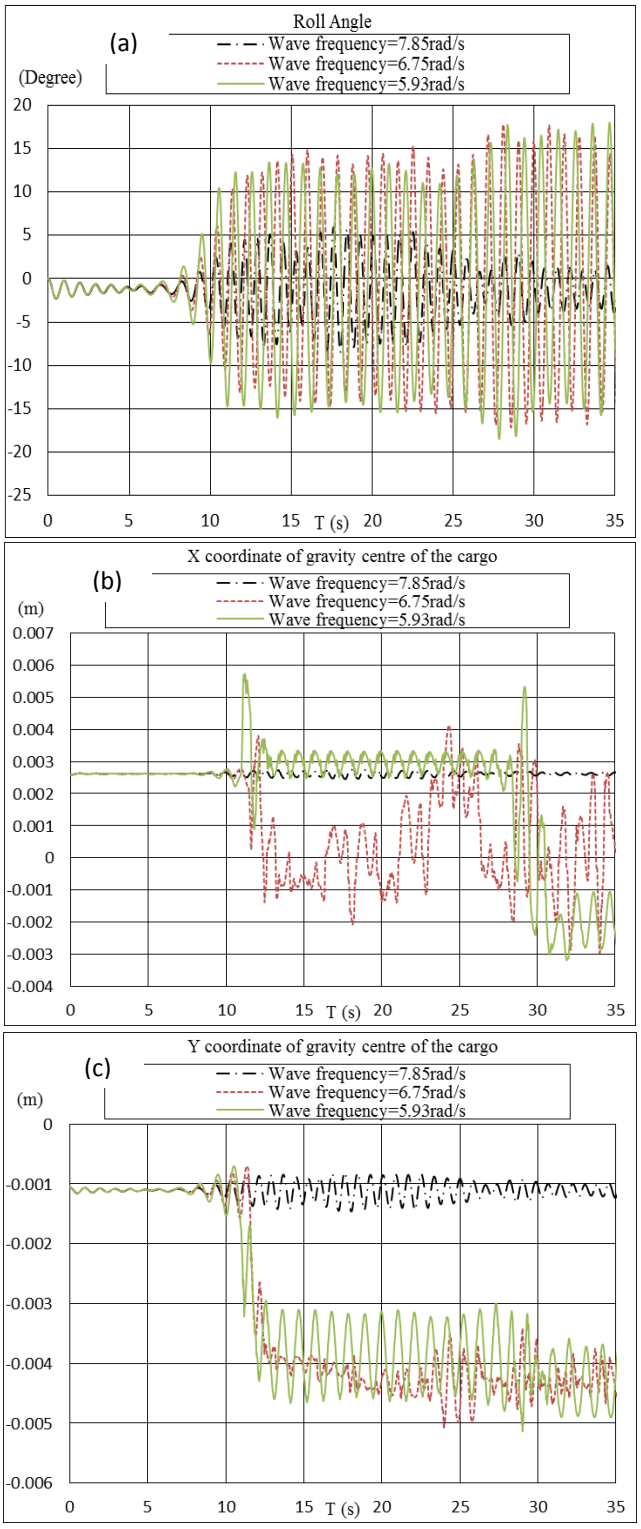

Figure 7.28 Roll angle of the container and mass centre of the cargo. The MC is fixed at 49%, the wave amplitude is fixed at 0.02m and the wave frequency is varied as 7.85rad/s, 6.75rad/s and 5.93rad/s (right)

Based on the parametric investigation above, the UBCSAND liquefaction model is activated to investigate the coupled simulation of 2D rectangular structure motion and cargo shift exposed to regular waves (Table 7.7). Two cases are tested using this method. The initial degree of saturation of the cargo is 50% and the validation properties of the cargo in Table 6.3 will be used.

Table 7.7 Parameters of linear wave for liquefaction

T (s)	ω (rad/s)	λ (m)	H (m)
0.93	6.76	1.35	0.027
0.93	6.76	1.35	0.04

It takes 27 CPU hours to finish 60s simulation time with one processor. As shown in Figure 7.29a, When the calculation time reaches 10s, the wave spreads to the container, causing the container to roll. The roll angle of the 2D structure shows irregularity as to the interaction between cargo shift and ship motion in waves. The roll angle of the container ranges from -10° to 10° with wave height of 0.04m, while the roll angle of the container ranges from -5° to 10° with wave height of 0.027m. This means that cargoes move to one side of the container and create a large moment to resist the righting moment of the container — resulting in a small heel. As we can see from Figure 7.29b, when the wave height is 0.027m, the liquefied percentage reaches 90% at 25s. When the wave height is 0.4m, the liquefied percentage reaches 90% at 20s, which indicates that the external energy input has a great influence on cargo liquefaction. When cargoes liquefies completely (100% liquefied percentage), the moment due to cargo shift shows a fluctuation around a fixed value of 0.8N.m and the roll angle fluctuates around a value of 2.5°. However, for the wave height of 0.04m, the fluctuation of the roll angle is close to the balance point of 0°. This can be explained by how energy input like waves will accelerate the liquefaction most definitely, but not always decrease the stability of the ship. As seen in Figure 7.29c, the moment due to cargo shift on the structure begins to fluctuate. For the wave height of 0.027m, the moment is around 0.8N.m. For the wave height of 0.04m, the moment is around 0.15N.m. Therefore, it can be concluded that energy input has a great influence on liquefaction and is proportional to the liquefaction rate. But, as

for the ship stability, this depends on a combination which includes cargo shift and the ship response in waves.

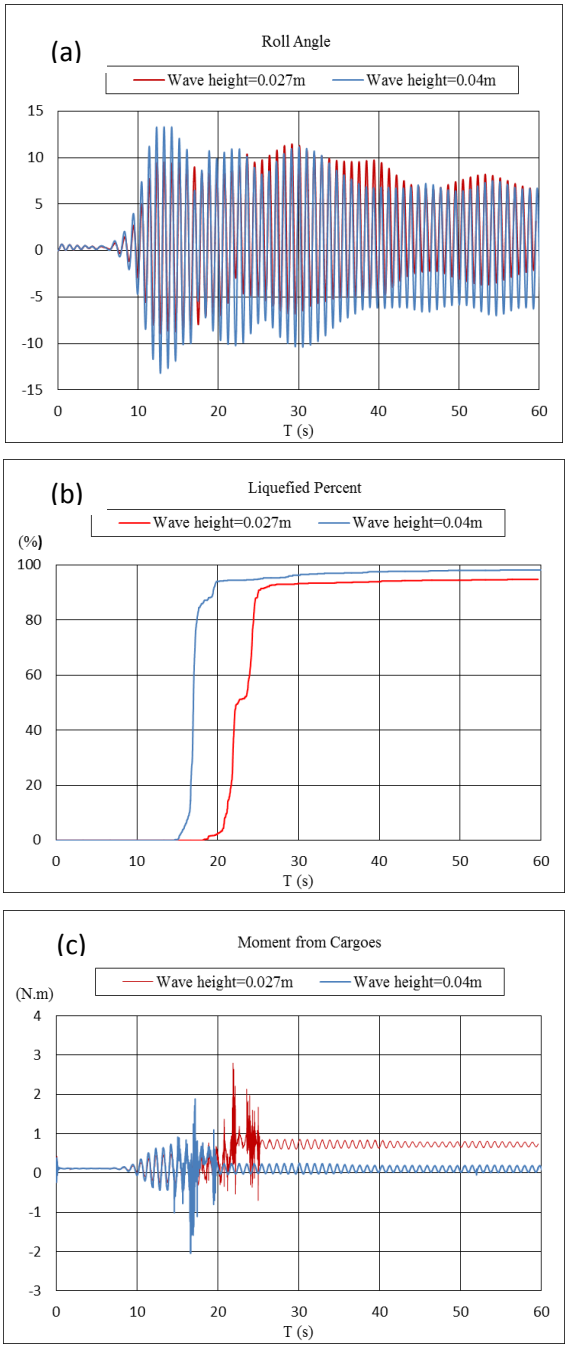

Figure 7.29 Development of (a) roll angle; (b) liquefied percent; (c) moment on the container versus wave height

7.6 Conclusions

In this chapter, the response of a 2D container in waves due to cargo shift, to address the liquefaction phenomenon, has been simulated by the method developed in the thesis. The method provides a better understanding of the liquefaction phenomenon, identification, and quantification of the controlling parameters. Based on the numerical results obtained in this chapter, some conclusions are summarized as follows:

1) The ANSYS Fluent can be used to model linear waves and irregular waves in a numerical tank. The dynamic response of the barge-like structure under linear waves tested in the numerical tank captured the coupled interaction between the linear waves and the structure.
2) To assess ship stability due to cargo shift, especially in wave conditions, an adapter to connect the ANSYS Fluent software with PFC software was developed to exchange data during the calculation. This adapter can predict the interaction between cargo shift and ship motion.
3) The response of the 2D structure in waves has been monitored during the carriage from cargo loading to cargo liquefaction. The roll angle of the container, cargo flow and liquefied percentage of cargoes were obtained based on this method.
4) External energy input has a great influence on liquefaction and is proportional to the liquefaction rate. But as for the ship stability, this is more complicated and is affected by cargo shift and the ship's motions in waves.

Chapter 8 Conclusions and Discussion

The risk of cargo liquefaction on ship safety, which can cause a sudden loss of stability of the carrying vessel, has risen sharply over the past few years. The IMSBC code requires that cargo that may liquefy should be shipped at a moisture content level below the TML, as determined in three laboratory methods specified in the IMSBC code. However, considering the ambiguity of testing and the variability in cargo properties and states, as well as conditions that can lead to liquefaction (pertaining to ship design and operation and environmental conditions), it is necessary to investigate the root causes that trigger the phenomenon and address the problem in a comprehensive manner. A numerical method was developed to assess the liquefaction potential based on the DEM code, which can determine the cargo flow, cargo deformation and its interaction with ship response in waves by combining with ANSYS Fluent software. Detailed conclusions are explained below.

8.1 Conclusions

The present research had the aim of assessing ship cargo liquefaction and the coupled motion of a 2D rectangular structure due to cargo shift in regular waves.

Chapter 1 of this thesis presented the history and latest developments in cargo liquefaction. The principles of liquefaction and the influence on ship stability were reviewed. Three methodologies currently listed in the IMSBC Code for iron ore fines determining Transportable Moisture Limit (TML), including Flow Table Test, Penetration Test and Proctor/Fagerberg Test. The methodology used in this thesis to address the cargo liquefaction problem was investigated. Following the introduction of this problem, Chapter 2 discussed the simulation methods expected to support and improve the test methods to determine cargo liquefaction, including experimental methods, continuum methods, and discrete element methods. The Finite Element Method is used to assess

earthquake liquefaction generally. However, it is not able to assess ship cargo liquefaction sufficiently, as ship stability due to cargo shift is a sea-ship-cargo problem. Therefore, Discrete Element Method (DEM) was discussed to show the advantages in predicting the discrete characteristic of cargo displacement.

Based on the discussions in Chapter 2, Chapter 3 summarized the computational methods involved in the simulation of cargo liquefaction used in the thesis. Namely, the UBCSAND liquefaction model was embedded into the DEM, and combined with ANSYS Fluent software to investigate a ship's response in waves due to cargo shift.

In Chapter 4, research on cargo liquefaction based on traditional methods was discussed to present the limitations in simulating cargo liquefaction. First, monotonic loading, cyclic loading, centrifuge test and shaking table test were presented to verify the UBCSAND liquefaction model based on FEM in PLAXIS software and to assess cargo liquefaction potential. It was concluded that with a higher initial degree of saturation of cargoes, frequency, and amplitude of the external energy input, the cargo is less resistant to liquefaction. As liquefied cargoes behave like a non-Newtonian fluid, ANSYS Fluent software is used to test tank sloshing and dam break of Newtonian and non-Newtonian fluids. As the simulations presented, instantaneous exciting force in irregular waves may cause liquefied cargoes to shift. To some extent, CFD methods can address the cargo liquefaction problem. However, there are some limitations in simulating the discrete characteristic of granular cargo flow. The FEM cannot identify the interaction between cargo shift and ship response, while the FVM cannot simulate the cargo flow during the transition from an unsaturated state to saturated state of granular materials. Therefore, a new method needed to be developed to overcome these limitations in the following chapters.

In Chapter 5, to solve the coupled motion between ship response and cargo shift during the whole process of a carriage, flow characteristics of the cargo needed to be identified. Static incline tests have been carried out to determine the flow characteristics at various

moisture contents. We used friction coefficients to represent moisture contents of cargo to neglect the existence of water. It was observed from the simulation results, when compared with the data from ClassNK, that the granular particle flow shows a good agreement with the nickel ore flow. However, the experimental data from ClassNK is based on the static incline test. Dynamic sloshing tests should thus be conducted to identify the accurate contact properties between particles.

During the carriage, external energy such as ship motion and propeller vibration may compact the cargoes, resulting in the deformation and change of properties of materials. Since the flow characteristics have been identified in Chapter 5, the deformation and properties change was addressed in Chapter 6. Namely, the DEM was used to simulate the flow, deformation and liquefaction phenomenon of the cargo combined with the UBCSAND model. Three assumptions have been presented: (1) each particle is regarded as a hypothetical assembler of particles, including many solid particles, water and air. The cargo just contains the solid skeletons. The porosity of the particles is also a hypothetical porosity. Water and air cannot be transferred to neighboring artificial particles as result of exerted elastic-plastic strain; (2) the radius of the particle can be scaled with the elastic-plastic strain according to the stress on the particles; and (3) various friction coefficients can be used to represent various moisture contents. According to the simulation results obtained from the numerical method based on some assumptions, the method can effectively capture the simple and cyclic shear behaviors, as observed in the laboratory constant volume DSS testing of sands. When the liquefied percentage defined in this chapter reached 100%, the fluctuation force on the container due to cargo shift increased suddenly. Therefore, the definition of 100% liquefaction in this model, regarded as the liquefaction criteria, is reasonable. However, due to the assumptions above and limited experimental data, more critical experiments should be carried out to validate the accuracy of the liquefaction model.

In Chapter 7, a numerical tank was built to determine the wave generation and predict the response of bodies in the waves, combined with Navier-Stokes equation, Volume of Fluid

(VOF) method and dynamic meshing method using ANSYS Fluent code. Roll motions of the 2D rectangular structure in waves have been analyzed and compared with the experimental data to validate the ANSYS Fluent code. To simulate the interaction between the cargo shift and ship motion in waves, a CFD-DEM adapter was developed to exchange data between the PFC and ANSYS Fluent code. Based on these two codes and the adapter, ship response due to cargo shift in waves was predicted. The 2D container response in waves and the ensuing cargo shift was assessed based on this method. It was concluded from the simulation results that external energy input such as waves has a great influence on cargo shift in the process of liquefaction, which affects the response of the container in return.

Given the satisfactory and reasonable results, it was shown that the approach developed in the thesis can address the ship cargo liquefaction phenomenon, and together with the CFD-DEM adapter, ship response in waves due to cargo shift can also be evaluated. The method developed in the thesis will provide a better understanding of the liquefaction phenomenon and could be feasibly used as a reference to support a suitable regulatory framework for liquefaction analysis of ship stability. This will improve decision making during the loading and transporting of cargoes and could be effective in helping to avoid instances of ship capsizing and casualties

8.2 Discussions

The novel features of this framework are:

1) Most research on liquefaction to date is based on the FEM, which has some limitations when addressing the discrete characteristics of granular materials. The DEM liquefaction model was developed first to investigate cargo flow and cargo liquefaction during carriage in a holistic way.
2) Ship response in waves, coupled with the effect of cargo shift on account of cargo liquefaction, was investigated. A CFD-DEM adapter was developed to exchange data to achieve a coupled calculation. This development can address the ship cargo

liquefaction problem in the real sea state.

Before using the DEM liquefaction model, three assumptions were presented: (1) each particle is regarded as a hypothetical assembler of particles, including many solid particles, water and air. The cargo just contains the solid skeletons. The porosity of the particles is also a hypothetical porosity. Water and air cannot be transferred to neighboring artificial particles as result of exerted elastic-plastic strain; (2) the radius of the particle can be scaled with the elastic-plastic strain according to the stress on the particles; and (3) various friction coefficients can be used to represent various moisture contents. The simulation results based on these three assumptions above shows good agreement with experimental data. To evaluate the assumptions, more critical experiments should be carried out to provide validations. Meanwhile, the present framework should be improved further to overcome some limitations.

8.3 Further Work

The method used in this thesis can still be improved in future research in the following ways:

1) More critical experiments should be carried out to provide data for the analysis of cargo properties.

Given the lack of experimental data on the properties of cargoes, the currently adopted parameters are hypothetical values. More data from the simple shear test and cyclic shear test need to be implemented to obtain more accurate properties of the cargo.

2) The Rolling Resistance Linear Model could be improved according to the real behavior of cargo.

The rolling resistance contact model used in the thesis incorporates torque acting on the contacting particles to prevent the roll motion to some extent. This could model the granular motion effectively. However, it is the simplest model. The static incline test in Chapter 5 is a quasi-static process and is not sufficient to describe the dynamic

characteristic of cargo. With critical experiments, modifying the model equations and parameters to make them as close to the real dynamic characteristics is necessary.

3) The liquefaction model should be improved to adapt to cargo deformation.
The radius of the particle can be scaled with the elastic-plastic strain according to the stress on the particles. This is a novel feature adopted by this thesis to overcome the limitation of the ball in the DEM code being regarded as a rigid body. This assumption should be further verified according to more critical experiments.

4) Moisture between particles should be considered.
In the investigations of CFD-DEM codes to date, the features of both mechanical and hydraulic behavior of the fluid-solid mixture system are captured, based on a saturated state. However, the cargo loading on the ship hold is generally unsaturated. To solve this problem, more attention needs to be paid to matric suction in the CFD-DEM equations.

5) Experiments should be carried out to provide validation to the simulation of ship response in waves due to cargo shift.

6) Codes in the method are based on the two-dimensional case. Three-dimensional simulations should be developed to model the real state of ship motion in waves.
The codes in the method, including the PFC software and ANSYS Fluent software, focus on the two-dimensional case. Therefore, codes for 3D should be developed to model the ship motion in waves.

7) Optimization analysis, including ship design and precautions during the carriage, should be carried out in the following study.

Reference

Arab A., Shahrour I., Lancelot L., 2011. A laboratory study of liquefaction of partially saturated sand. *Journal of Iberian Geology,* 37(1), 29-36.

Allen M. P., Tildesley D. J., 1987. Computer Simulation of Liquids. *Oxford University Press*.

Andrei Cristian, Hanzu Pazara Radu, 2013. The impact of bulk cargoes liquefaction on ship's intact stability. *UPB Scientific Bulletin, Series B: Chemistry and Materials Science*, 75, 47-58.

ANSYS FLUENT Theory Guide, 2012.

Beaty M., Byrne P.M., 1998. An effective stress model for predicting liquefaction behavior of sand. *Geotechnical Earthquake Engineering and Soil Dynamics III, ASCE Geotechnical Special Publication*, 75(1), 766-777.

Beaty M., Byrne P.M., 2011. UBCSAND constitutive model version 904aR.

Beaty Michael H., Byrne Peter M., 2011. UBCSAND constitutive model version 904aR.

Bian H.B., 2007. Numerical model for unsaturated sandy soils in seismic area: Application to liquefaction. *PHD thesis*, Universite´ des SciencesetTechnologiesdeLille.

Biot M.A., 1941. General theory of three-dimensional consolidation. *J. Applied Physics*, 12, 155-164.

Bishop A.W., 1959. The principle of effective stress. *Tek. Ukebl.*, 106(39), 113-143.

Blight G.E., 1967. Effective stress evaluation for unsaturated soils. *J. Soil Mech. Found. Engng., ASCE*, 93(SM2), 125-148.

BYRNE P.M., PARK S.S, BEATY M., SHARP M., GONZALEZ L., ABDOUN T., 2004. Numerical modeling of dynamic centrifuge tests. *13th World Conference on Earthquake Engineering*, No. 3387.

Bulk Carrier Guide (2010). Safe carriage of Iron ore & other iron concentrates in bulk. Retrieved online from bulkcarrierguide.com: <http://bulkcarrierguide.com/iron-ore>

Chen L.X., Miller G.A., Kibbey T.C.G., 2007. Rapid pseudo-static measurement of hysteretic capillary pressure-saturation relationships in unconsolidated porous media.

ASTM Geotech. Test. J., 30(6), 1-10.

ClassNK, 2011. Guidelines for the Safe Carriage of Nickel Ore.

ClassNK magazine 64th edition.

Cochard S., Ancey C., 2009. Experimental Investigation into the Spreading of Viscoplastic Fluids onto Inclined Planes. *Journal of Non-Newtonian Fluid Mechanics*, 158, 73–84.

Colagrossi A, Landrini M, 2003. Numerical simulation of interfacial flows by smoothed particles hydrodynamics. *Journal of Computational Physics,* 191, 448-75.

Coleman J.D., 1962. Stress-strain relations for partially saturated soils. *Géotechnique*, 12(4), 348-350.

Cundall P. A., Hart R., 1992. Numerical Modeling of Discontinua. *J. Engr. Comp*., 9, 101-113.

Cundall P.A., 1971, A computer model for simulating progressive large-scale movements in block rock mechanics. *Proceedings of Symposium of International Society of Rock Mechanics*, 2(8).

Dabeet A., 2014. Discrete element modelling of direct simple shear response of granular soils and model validation using laboratory tests. *PhD thesis,* The University of British Columbia.

Dabeet A., Wijewickreme D., and Byrne P., 2012. Simulation of cyclic direct simple shear loading response of soils using discrete element modelling. *15th world conference on earthquake engineering.*

Dafalias Y.F., Popov E.P., 1976. Plastic internal variables formalism of cyclic plasticity. *J. Appl. Mech., ASME*, 43, 645-651.

Feng, M., Fredlund, D.G., 1999. Hysteretic influence associated with thermal conductivity sensor measurements. *Proceeding from Theory to the Practice of Unsaturated Soil Mechanics, in associated with 52nd Canadian Geotechnical Conference and Unsaturated Soil Group*, 651-657.

Fortin J., Millet O., Saxcé G. de., 2003. Construction of an averaged stress tensor for a granular medium. *European Journal of Mechanics A/Solids,* 22, 567–582.

François Nicot, Nejib Hadda, Mohamed Guessasma, Jerome Fortin, Olivier Millet, 2013.

On the definition of the stress tensor in granular media. *International Journal of Solids and Structures*, 50, 2508–2517.

Fredlund D. G., Rahardjo H., 1993. Soil mechanics for unsaturated soils, *John-Wiley.*

Gard, 2014. Liquefaction of solid bulk cargoes.

Galavi V., Petalas A., Brinkgreve R.B.J., 2013. Finite element modelling of seismic liquefaction in soils. *Geotechnical Engineering Journal of the SEAGS &AGSSEA*, 44, 55-64.

Galavi V., 2010. Groundwater flow, fully coupled flow deformation and undrained analyses in PLAXIS 2D and 3D. Internal report from PLAXIS BV.

Genuchten V., Th. M., 1980. A closed-form equation for predicting the hydraulic conductivity of unsaturated soils. *Soil Sci. Soc. Am. J*., 44, 892–898.

Ghadampour Z., Talebbeydokhti N., Hashemi M. R., Nikseresht A. H., Neill S. P., 2013. Numerical Simulation of Free Surface Mudflow Using Incompressible SPH. *IJST, Transactions of Civil Engineering*, 37(C1), 77-95.

Gillham, R.W., Klute, A., Heermann, D.F., 1976. Hydraulic properties of a porous medium: measurement and empirical representation. *Soil Sci. Soc. Am. J.*, 40(2), 203-207.

Goniva, C., Kloss, C., Deen, N.G., Kuipers, J.A.M., Pirker, S., 2012. Influence of rolling friction modelling on single spout fluidized bed simulations. *Particuology,* 10, 582-591.

Huang X., Garcia M., 1998. A Herschel–Bulkley model for mud flow down a slope. *Journal of Fluid Mechanics,* 374, 305-333.

International Maritime Organization. International Maritime Solid Bulk Cargoes (IMSBC) Code.

Iwashita K., Oda M., 1998. Rolling resistance at contacts in simulation of shear band development by DEM. *Journal of Engineering Mechanics ASCE*, 124, 285-292.

Jean Louis, 2013. Geotechnical Engineering. *Unsaturated and Saturated Soils.*

Jaeger H. M., Nagel S.R., Behringer R., 1996. Granular solids, liquids and gases. *Reviews of Modern Physics,* 68(4), 1259-1273.

Jennings, J.E., 1961. A revised effective stress law for use in the prediction of the behavior of unsaturated soils. *In Symposium on pore pressure and suction in soils*, 26-30.

Ju L., Vassalos D., Jin W., 2013. Rolling motion of Newtonian and non-Newtonian fluids in a ship hold. *5th International Maritime Conference on Design for Safety.*

Ju L., Vassalos D., Boulougouris E., 2016. Numerical assessment of cargo liquefaction potential. *Ocean Engineering*, Volume 120, 1 July 2016, Pages 383-388.

Jung K.H Chang K.A, Jo H.J, 2006. Viscous effect on the roll motion of a rectangular structure. *Journal of Engineering Mechanics*, 132(2), 190-200.

Khezzar L., Seibi A., Goharzadeh A., 2006. Water Sloshing in Rectangular Tanks – An Experimental Investigation & Numerical Simulation. *International Journal of Engineering*, 3, 175-184.

KIM Yonghwan, 2001. Coupled Analysis of Ship Motions and Sloshing Flows. *16th International Workshop on Water Waves and Floating Bodies*, 21, 81-84.

Kleinhans M. G., Markies H., S. J. de Vet, A. C. in ’t Veld, and Postema F. N., 2011. Static and dynamic angles of repose in loose granular materials under reduced gravity. *JOURNAL OF GEOPHYSICAL RESEARCH*, 116.

Komatina D., Jovanovic M., 1997. Experimental Study of Steady and Unsteady Free Surface Flows with Water-clay Mixtures. *Journal of hydraulic research*, 35 (5), 579-590.

Kyokai N.K, 2012. Guidelines for the Safe Carriage of Nickel Ore (Second Edition).

Koromila, I.A., Spandonidis, C.C., Spyrou, K.J. (2013). Experimental investigation of cargo liquefaction and impact on the stability of a bulk – carrier. *Proc. 13th Int. Ship Stability Workshop*.

Lee B.H., Park J.C. and Kim M.H., 2010. Two-dimensional vessel-motion/liquid-sloshing interactions and impact loads by using a particle method. *ASME 2010, 29th International Conference on Ocean, Offshore and Arctic Engineering,* 6, 679-686.

Liu C.Y., 2009. A coupled hydraulic-mechanical elastoplastic constitutive model for unsaturated sands and silts. *PHD thesis,* University of Oklahoma.

Liu, D., Lin, P., 2008. A numerical study of three-dimensional liquid sloshing in tanks. *Journal of Computational Physics,* 227 (8), 3921-3939.

Lowe, D., 1976. Grain flow and grain flow deposits. *J. Sed. Pet*., 46, 188–199.

Lubachevsky B. D., 1991. How to Simulate Billards and Similar Systems. *J. Comp. Phys.,* 94(2) 255.

Luding Stefan, 2008. Introduction to Discrete Element Methods -Basics of Contact Force Models and how to perform the Micro-Macro Transition to Continuum Theory. *Discrete modelling of geomaterials*, 785 – 826.

London P&I Club, 2012. Vinalines Queen-Dangers of Carriage of Nickel Ore, Retrieved online from longonpandi.com: <http://www.londonpandi.com/article/665/vinalines-queen-dangers-of-carriage/>

Lloyd's List (2010). Seafarers Missing After Bulker Capsizes, Retrieved online from: <http://www.lloydslistdcn.com.au/archive/2010/october/29/seafarers-missing-after-bulker-capsizes>

Martin G.R., Finn W.D.L., Seed H.B., 1975. Fundamentals of liquefaction under cyclic loading. *Journal of the Geotechnical Engineering Division, ASCE*, 101.

Matson G.P., Hogg A.J., 2007. Two-dimensional Dam Break Flows of Herschel–Bulkley Fluids: The Approach to the Arrested state. *Journal of Non-Newtonian Fluid Mechanics*, 142, 79–94.

Miller S., Luding S., 2004a. Cluster Growth in two- and three-dimensional Granular Gases. *Phys. Rev. E*, 69(031305), 1-8.

Miller S., Luding S., 2004b. Event Driven Simulations in Parallel. *J. Comp. Phys*., 193(1), 306-316.

Mualem Yechezkel, 1976. A new model for predicting the hydraulic conductivity of unsaturated porous media. *Journal of water resources research*, 12, 513–522.

Muraleetharan, K.K., Wei, C.F., 1999. Dynamic behavior of unsaturated porous media: governing equations using the theory of mixtures with interfaces (TMI). *Int. J. Numer. Anal. Meth. Geomech.*, 23, 1579-1608.

Maritime Accident Casebook, 2010. Hong Wei: A Victim of Wetness? Available from: http://maritimeaccident.org/2010/12/hong-wei-a-victim-of-wetness-2/

Nurand, A., Byerlee, J. D., 1971. An exact effective stress law for elastic deformation of rock with fluids. *J. Geophys. Res*., 76, 6414–6419.

Pande, G., Beer, G., Williams, J.R., 1990. Numerical modeling in rock mechanics, *John Wiley and Sons*.

Petalas Alexandros., Galavi Vahid., 2013. Plaxis Liquefaction Model UBC3D-PLM *PLAXIS Report*.

Poschel T., Schwager T., 2005. Computational Granular Dynamics, Springer.

PFC, 2016. PFC 5.0 Help Manual

Poulovassilis, A., 1970a. Hysteresis of pore water in granular porous bodies. *Soil Sci.,* 109(1), 5-12.

Puebla, H., Byrne, M., P.Philips, P., 1997. Analysis of canlex liquefaction embankments prototype and centrifuge models. *Canadian Geotechnical Journal*, 34, 641-651.

Rapaport D. C., 1995. The Art of Molecular Dynamics Simulation. *Cambridge University Press*.

Report 4: Reference tests, TWG, 2013.

Report of Market Realist, 2015.

Rose T. P., 2014. Solid bulk shipping: cargo shift, liquefaction and the transportable moisture limit. Thesis of Master of Science at University of Oxford.

Roberta Brondani MinussiI, Geraldo de Freitas Maciel, 2012. Numerical experimental comparison of dam break flows with non-Newtonian fluids. *Journal of the Brazilian Society of Mechanical Sciences and Engineering*, 34 (2).

S Ji, 2013. Analysis of interaction between ice floe and ship hull with discrete element method in broken-ice field. *Chinese Journal of Applied Mechanics*, 30(4), 520-526.

Sun M. S., Incecik, A.,2015. A Numerical Study of Extreme Wave Train. *Proceedings of the 9th International Workshop on Ship and Marine Hydrodynamics.*

Sun D.A, Sheng D.C, Sloan S.W., 2007. Elastoplastic modelling of hydraulic and stress–strain behavior of unsaturated soils. *Mechanics of Materials*, 39, 212-221.

Spandonidis C.C., Spyrou K.J., 2012. Use of granular material dynamics simulation for the study of cargo shift of ships. *Proceedings of the 11th International Conference on the Stability of Ships and Ocean Vehicles*, 497-507.

Spandonidis C.C., Spyrou K.J., 2013. Micro-scale modeling of excited granular ship cargos: A numerical approach. *Ocean Engineering*, 74, 22–36.

Spandonidis C.C., Spyrou, K.J., 2016. Coupled vessel-dry-granular-cargo roll dynamics in regular beam seas. *Ocean Engineering*, 120, 238-245.

Sriskandakumar, S., 2004. Cyclic loading response of fraser sand for validation of numerical models simulating centrifuge tests. Master's Thesis, University of British Columbia, Department of Civil Engineering.

Sabatina Cuomo, Mariagiovanna Moscariello, Vito Foresta, 2016. Simple shear test son unsaturated soils. *Procedia Engineering,* 158, 122-127.

Technical Working Group, 2013. Iron ore technical working group submission for evaluation and verification.

Terzaghi K., 1936. The shear resistance of saturated soils. Proceedings for the 1st. *International Conference on Soil Mechanics and Foundation Engineerin*g, 1, 54-56.

Toumi M., Bouazara M., Richard M.J., 2009. Impact of liquid sloshing on the behavior of vehicles carrying liquid cargo. *European Journal of Mechanics A/Solids,* 28, 1026–1034.

Tsegaye A., 2011. Plaxis Liquefaction Model.

TWG report, 2013. Iron Ore Technical Working Group Submission for Evaluation and Verification.

Unno T., Kazama M., Sento N. and Uzuoka R., 2006. Cyclic shear behavior of unsaturated volcanic sandy soil under various suction conditions. *The 4th International Conference on Unsaturated Soils*, ASCE.

Usama El Shamy, Mourad Zeghal, 2005. Coupled continuum-discrete model for saturated granular soils. *Journal of Engineering mechanics*, 131, 413-426.

Wensrich C. M., Katterfeld A., 2012. Rolling Friction as a Technique for Modelling Particle Shape in DEM. *Powder Technology*, 217, 409-417.

Wijewickreme, D., Sriskandakumar, S., Byrne, P., 2005. Cyclic loading response of loose air-pluviated Fraser River sand for validation of numerical models simulating centrifuge tests. *Canadian Geotechnical Journal*. 42:2, 550-561.

Williams, J.R., Hocking, G., Mustoe, G.G.W., 1985. The theoretical basis of the discrete element method. *Numerical Methods of Engineering, Theory and Applications.*

Xue Y.D., Liu Z.Q., Wu. J., 2014. Direct shear tests and PFC2D numerical simulation of

colluvial mixture. *Rock and Soil Mechanics*, 35, 587-592.

Zhao X.Z., Hu C.H., 2012. Numerical and experimental study on a 2-D floating body under extreme wave Conditions. *Applied Ocean Research*, 35, 1-13.

Zhang J.W., Wu W.Q., Hu J.Q., 2016. A numerical study of the effects of the longitudinal baffle on nickel ore slurry sloshing in a prismatic cargo hold. *Marine Structures Marine Structures*. 46, 149-166.

Zhou J., Jian Q.W., Wu X.H., Li N., Zhu Y.M., 2013. Model experimental study of fluidization of iron concentrate ore in bulk. *Chinese Journal of Rock Mechanics and Engineering*, 32, 2536-2543.

Zhou J., Jian Q.W., Zhang J., Li N., 2013. Dynamic behaviors of iron ore concentrate under cyclic loading by hollow cylinder apparatus. *Chinese Journal of Geotechnical Engineering*, 35, 2346-2352.

Zhou J., Yang Y.X., Liu Y., Jia M.C., 2009. Numerical modeling of sand liquefaction behavior under cyclic loading, *Rock and Soil Mechanics,* 30, 1083-1088.

Zhou Z. Q., de Kat, J. O., Buchner, B., 1999. A nonlinear 3-D approach to simulate green water dynamics on deck. *Proceedings of the 7th International Conference on Numerical Ship Hydrodynamics*, 5(1), 1-15.

Zhu H.P., Zhou Z. Y., Yang R.Y., Yu A. B., 2007. Discrete particle simulation of particulate systems: theoretical developments. *Chemical Engineering Science*, 62(13), 2278-2296.

Appendix 1: Cargo Liquefaction Fatalities

Table 1 Accidents related to liquefaction and their consequences

No.	Ship name	Accident description	Casualties	References
1	Wen Qiao	Sank 17 September 2007 off North Korea, carrying iron ore fines	1	(Bulk Carrier Guide, 2010)
2	Heng Tai	Sank 2 October 2007 off India with destination in Bangladesh, carrying iron ore fines	2	(China P&I, 2010)
3	Black Rose	Sank 9 September 2009 off Paradip, western coast of India, with 23,000 MT of iron ore fines	1	(Bulk Carrier Guide, 2010)
4	Nam Yang 8	Sank 1 January 2010 off the island of Cayagan, The Philippines, carrying 2,600 MT of iron sand.	0	(Lloyd's List, 2010)
5	Jian Fu Star	Sank 27 October 2010 off China with 43,000 MT of nickel ore from Indonesia	13	(Lloyd's List, 2010)
6	Nasco Diamond	Sank 10 November 2010 off China, with 55,150 MT of nickel ore from Indonesia	21	(Lloyd's List, 2010)
7	Hai Xin	Sank 22 November 2010, China, with 6,055 MT of magnetite ore	0	(Lloyd's List, 2010)
8	Hong Wei	Sank 3 December 2010 off Philippines with 40,000 MT of nickel ore from Indonesia	10	(Maritime Accident Casebook, 2010)

9	Vinalines Queen	Sank 25 December 2011between Luzon and China of nickel ore from Indonesia	22	(London P&I Club, 2012)
10	Sun Spirit	Sank 23 January 2012 off Catanduanes, The Philippines, carrying iron sand	0	
11	Trans Summer	Sank February 2014 off coast of Hong Kong sailing from Indonesia to China carrying nickel ore.	0	

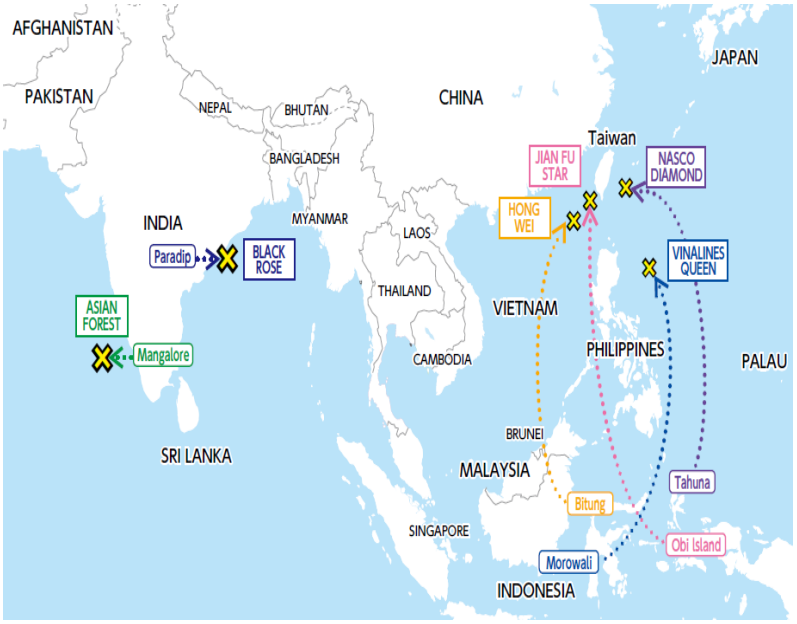

Figure 1 Sinking sites of ships that capsized and sank caused by cargo liquefaction since 2009 (ClassNK magazine 64th edition)

Note: Further details regarding maritime accidents can be found in the documents submitted to IMO.

Appendix 2: Test Procedures for Cargoes TML

Group A cargoes are apt to liquefy, and group A cargoes are classified as: A) Concentrates are refined like iron and nickel concentrate; b) Various nickel ore with different color and size; c) Coal with 75% is made up of particles less than 5mm in size (IMSBC Code). Cargo liquefaction can result in cargo shift. Due to compaction owing to ship motion, the spaces between particles reduce resulting in pore water pressure increasing, which weakens the friction between particles. This process will result in cargo shift. For avoiding cargo liquefaction, the moisture content should be limited below transportable moisture limit (TML) which is determined by the appropriate authority. Three methodologies are listed in IMSBC code for TML determination including Flow Table Test, Penetration Test and Proctor/Fagerberg Test as shown in Figure 1. If the moisture content of the cargoes exceeds the TML, the cargoes are in the risk of liquefaction during carriage (see Figure 2).

(a) Flow table test

(b) Penetration test

(c) Proctor/Fagerberg test

Figure 1 Three methodologies listed in IMSBC Code

Figure 2 Iron ore fines before and after liquefaction

Appendix 3: Precautions and Recommendations

Even the moisture content of the cargoes is less than TML, the cargoes have the hazard of liquefaction because of the measurement error and the moisture migration from the atmosphere. Therefore, some precautions can be used to enhance the ship stability during the voyage. ClassNK listed some precautions as shown below:

1) Cargo hold should have longitudinal bulkheads and the master should retain the operation manual;
2) The cargoes with moisture should limit below TML with the test results conducted within six months to the date of loading; Test to determine the moisture content should be conducted within seven days to the date of loading;
3) When the cargo is transported from stockyard to the ship, notice that the cargo may have been affected by rainfall or waves; Use radar to detect rainfall at early stage
4) If the moisture content of the cargo exceeds the TML, the loading of cargoes shall not be accepted;
5) At loading stage, cargo should be properly trimmed as far as possible;
6) During voyage, moisture should be discharged by a pump;
7) Moisture deposition and cargo behavior should be monitored during voyage. The cargo distribution should be trimmed as soon as possible;

Appendix 4: TWG Report

In the unsaturated state, when the degree of saturation of the cargoes increases, the friction coefficient decreases. If we use the definition of soil liquefaction in soil mechanics, even the soil did not liquefy, the ship stability could be influenced. Iron Ore Technical Working Group conducted some research on evaluation and verification of liquefaction. However, TWG report continues to use the definition of liquefaction in soil mechanics, which is not accurate and applicable to the study on cargo liquefaction and ship stability. Some conclusions from TWG report are shown as below:

Iron ore fines are mainly found as goethites, hematites or magnetites and mixtures of each (TWG report, 2013). Iron ore fines with high goethites have a high liquefaction resistance. Especially cargoes with high geothites content show high holding water ability as shown in Figure 1. The bulk strength of cargoes with high goethites appear to strengthen as the degree of saturation increases up to 90%, where the hematites and magnetitic ores appear to weaken as the degree of saturation increases (see Figure 2). In the Hexapod model tests, goethite ores also show high liquefaction resistance at all water contents, even higher than TML (see Figure 3, Figure 4 and Figure 5).

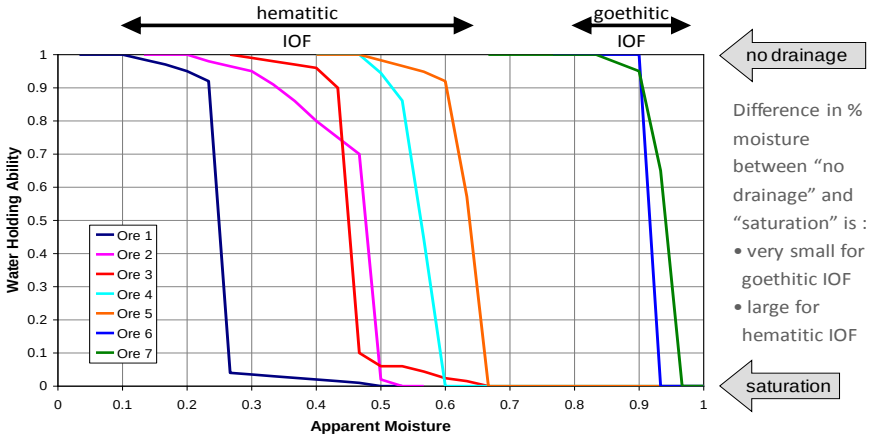

Figure 1 Water Holding Ability as a function of apparent moisture content for IOF (TWG report, 2013)

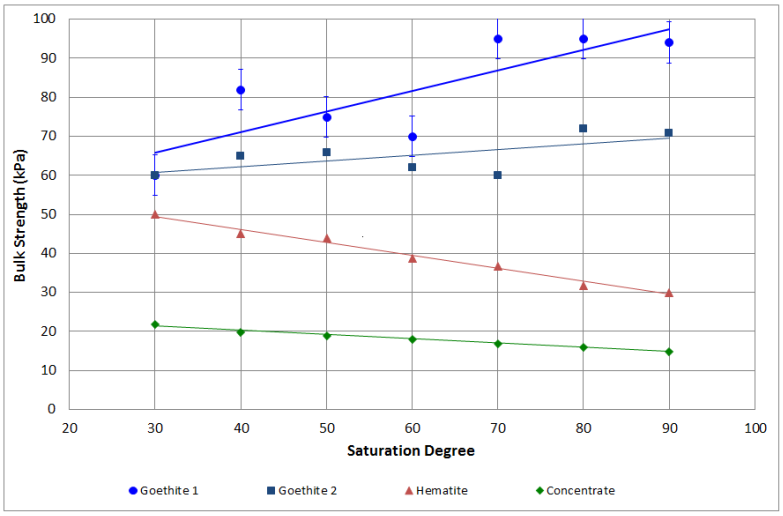

Figure 2 Bulk Strength verses saturation degree for iron ore fines (TWG report, 2013)

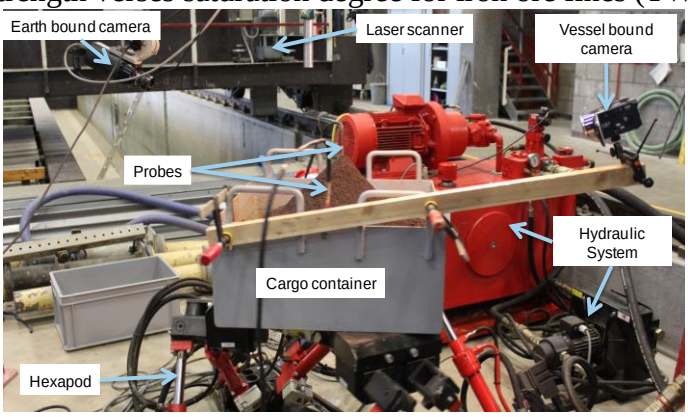

Figure 3 Hexapod Apparatus showing model cargo and hold and instrumentation (TWG report, 2013)

Figure 4 A Goethite sample before and after sea state test (TWG report, 2013)

Figure 5 A hematite sample before and after sea state test (TWG report, 2013)

Appendix 5: Particle Flow code

A. PFC

Discrete Element Method (DEM) was originally developed by Cundall in 1971 to problems in rock mechanics. The theoretical basis of the method was established by Isaac Newton in 1697. Williams, Hocking and Mustoe in 1985 showed that DEM could be viewed as a generalized finite element method. Its application to geomechanics problems is described in the book Numerical Methods in Rock Mechanics, by Pande, G., Beer, G. and Williams, J.R.. A DEM-simulation consists of three parts: the initialization, explicit time-steeping and post-processing. The forces and motion are computed from the initial condition and relevant physical laws and contact models. Particle Flow Code (PFC) is classified as a discrete element code, however, is a simplified version of DEM because of the restriction to rigid particles and cannot handle the deformation problems. Newton's second law is used to determine the motion of each particle, while the force-displacement law is used to update the contact forces. PFC provides a particle-flow model containing the following assumptions (PFC manual): 1) The particles are treated as rigid bodies; 2) The fundamental particle shape is a {disk with unit thickness in 2D; sphere in 3D}; 3) Particles interact at pair-wise contacts by means of an internal force and moment. Contact mechanics is embodied in particle-interaction laws that update the internal forces and moments; 4) Behavior at physical contacts uses a soft-contact approach where the rigid particles are allowed to overlap one another at contact points. The contacts occur over a vanishingly small area (i.e., at a point), and the magnitude of the overlap and/or the relative displacement at the contact point are related to the contact force via the force-displacement law; 5) Long range interactions can also be derived from energy potential functions.

B. Rolling Resistance Linear Model

Rolling Resistance Linear Model will be selected to simulate the cargoes flow characteristic. The effect of rolling resistance at contacts between particles, and associated energy dissipation, may be of major importance for many granular applications in dense, quasi-static and dynamic regimes. The rolling resistance contact model provided in PFC is the simplest model, which incorporates torque acting on the contacting particles to prevent the roll motion at some extent. In real granular contacts, there are different contact mechanisms, like adhesion of contact point. This will be analyzed based on specific cases. Rolling Resistance Linear Model is introduced briefly in this section as follows. More detailed introduction is presented in PFC help manual.

B.1. Behavior

The behavior of the linear rolling resistance contact model is similar to the linear model, except that the internal moment is incremented linearly with the accumulated relative rotation of the contacting pieces at the contact point. The linear component includes linear elastic (no-tension), frictional behavior, while the dashpot component provides viscous behavior (see Figure 1). The linear force is produced by linear springs with constant normal and shear stiffnesses, k_n and k_s. The dashpot force is produced by dashpots with viscosity given in terms of the normal and shear critical-damping ratios, β_n and β_s. The normal and shear components of the linear force by F_n^l and F_s^l, respectively. The normal and shear components of the dashpot force by F_n^d and F_s^d, respectively.

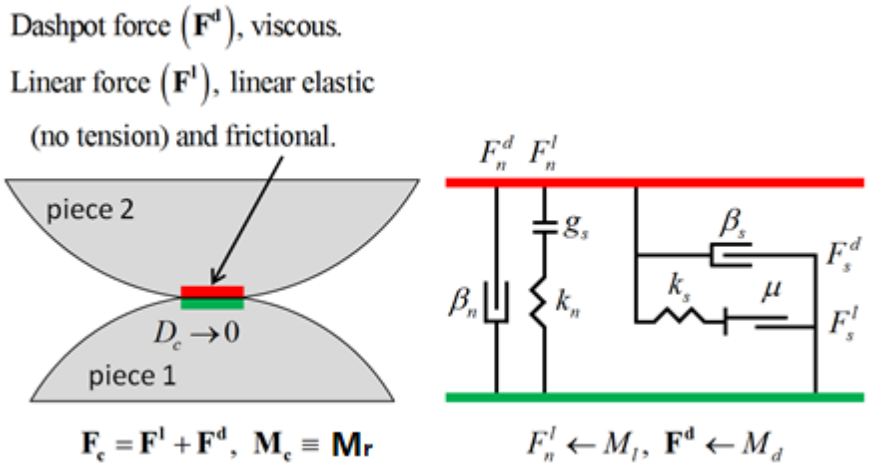

Figure1 Behavior and rheological components of the rolling resistance linear model

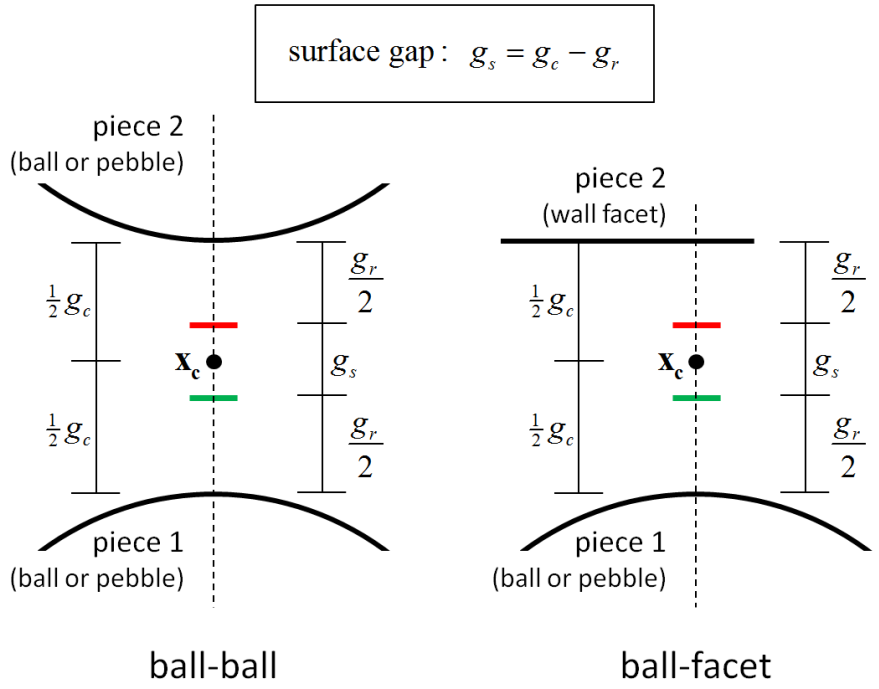

Figure 2 Surface gap for the linear-based models

B.2. Activity-Deletion Criteria

A contact with the rolling resistance linear model is active if and only if the surface gap ($g_s = g_c - g_r$) is less than or equal to zero. The force-displacement law is skipped for inactive contacts (see Figure 2).

B.3. Force-Displacement Law

The relative displacement increment at the contact during a timestep Δt is given by $\Delta\delta_n$ and $\Delta\delta_s$ in this equation of the "Contact Resolution" section. If the contact transitions from inactive to active during the current timestep, then only the portion of this increment that occurs while the surface gap is negative is used to perform the incremental update of the normal and shear forces. The relative displacement increment is adjusted:

$\Delta\delta_n \coloneqq \alpha\delta_n, \Delta\delta_s \coloneqq \alpha\delta_s$

$$\alpha = \begin{cases} \dfrac{g_s}{g_s - (g_s)_o} & (g_s)_o > 0 \text{ and } g_s < 0 \\ 1 & \text{otherwise} \end{cases}$$

$(g_s)_o$: the surface gap at the beginning of the timestep

The force-displaccement law updates the contact force and moment as:

$\boldsymbol{F_c = F^l + F^d}, \quad \boldsymbol{M_c = M_r}$

$\boldsymbol{F^l = -F_n^l \hat{n}_c + F_s^l}, \quad \boldsymbol{F^d = -F_n^d \hat{n}_c + F_s^d}$

$\boldsymbol{F^l}$: the linear force

$\boldsymbol{F^d}$: the dashpot force, both forces are resolved into normal and shear forces

$\boldsymbol{M_r}$: the rolling resistance moment

Where $F_n^{\{l,d\}} > 0$ is tension.

The force-displacement law for the Rolling Resistance Linear Model consists of the following steps:

1) Update the linear normal force based on the normal-force update mode;
2) Update the linear shear force as follows;
3) Update the dashpot normal force based on the dashpot behavior mode;
4) Update the dashpot shear force based on the dashpot behavior mode;
5) Update the rolling resistance moment.

B.4. Energy Partitions

Energy partitions track the energy that a contact model stores or dissipates. The linear model provides three energy partitions:

Strain energy: stored in the linear springs;

Slip energy: defined as the total energy dissipated by frictional slip; and

Dashpot energy: defined as the total energy dissipated by the dashpots.

B.5. Properties

The properties defined by the rolling resistance linear contact model are listed in the Table 2.

Table 2 Parameters of Rolling Resistance Linear Model

Group	Symbol	Description
Linear Group	k_n	Normal stiffness [force/length]
	k_s	Shear stiffness [force/length]
	μ	Friction coefficient [-]
	g_r	Reference gap [length]
	M_l	Normal-force update mode [-]
	E^*	Effective modulus [force/surf.]
	k^*	Normal-to-shear stiffness ratio [-]
	S	Slip state [-]
	F^l	Linear force [force]
Dashpot Group	β_n	Normal critical damping ratio [-]
	β_s	Shear critical damping ratio [-]
	M_d	Dashpot mode [-]
	F^d	Dashpot force [force]
Rolling resistance Group	k_r	Rolling resistance stiffness [force*length]
	μ_r	Rolling resistance coefficient [-]
	s_r	Rolling slip state [-]
	M^r	Rolling resistance moment [force*length]

B.6. Methods and Deformability

Table 3 Rolling Resistance Linear Model methods

Method	**Arguments**	**Symbol**	**Range**	**Description**
deformability	emod	E^*	[0.0, +∞)	Effective modulus
	kratio	k^*	[0.0, +∞)*	Normal-to-shear stiffness ratio
* By convention, setting $k^* = 0.0$ sets $k_s = 0$ but does not alter k_n.				

The method to use rolling resistance linear model is shown in Table 3. The deformability of a homogeneous, isotropic, and well-connected granular assembly experiencing small-strain deformation can be fit by an isotropic material model, which is described by the elastic constants of Young's modulus (E) and Poisson's ratio (ν). E and ν are emergent properties that can be related to the effective modulus (E^*) and the normal-to-shear stiffness ratio ($k^* \equiv k_n/k_s$) at the contact as follows: E is related to E^* , with E increasing as E^* increases; ν is related to k^*, with ν increasing up to a limiting positive value as k^* increases.

Appendix 6: Tank Sloshing

A. Dam Break

A dam break flow experiment was performed in a tank measuring 3.22 m × 1 m ×1.8 m (Zhou et al., 1999), as shown in Figure 1. After the flap was removed, the water with an initial water height equal to 0.6 m flowed freely. The water elevations and pressure were measured using two water height probes (H1 and H2) and one pressure gauge (P1).

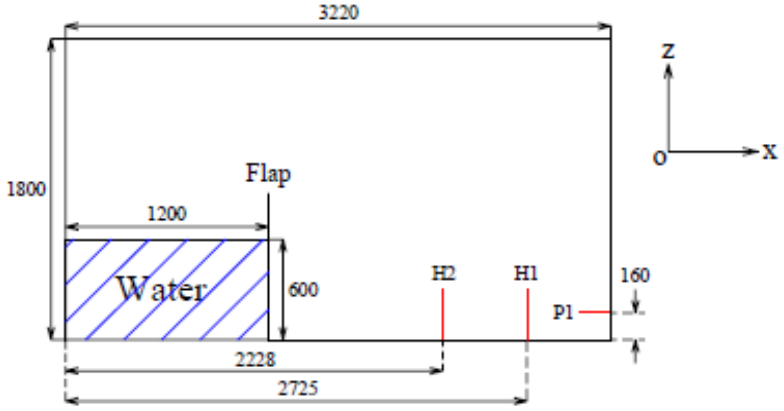

Figure 1 Sketch of the 2-D dam break experiment (units: mm)

The problem can be considered as a two-dimensional flow problem in the simulation. The computed results are compared with the experimental results and with other numerical results obtained by the SPH method (Colagrossi and Landrini, 2003). The interface profiles and rolling motion obtained by the two methods are similar, as shown in Figure 2 compare the water elevations at H1 and H2. It is apparent that the present results agree reasonably well with the experiment results. When $t\sqrt{(g/h0)}>6$, because of the limit in accuracy of measurements in the chaotic flow and the difference between flap lifting process, the calculation data show a large deviation from the experimental data. A comparison of the pressure time histories is shown in Figure 3, Figure 4 and Figure 5. At $t\sqrt{(g/h0)}>6$, the wave flow encounters P1, which causes the first pressure peak.

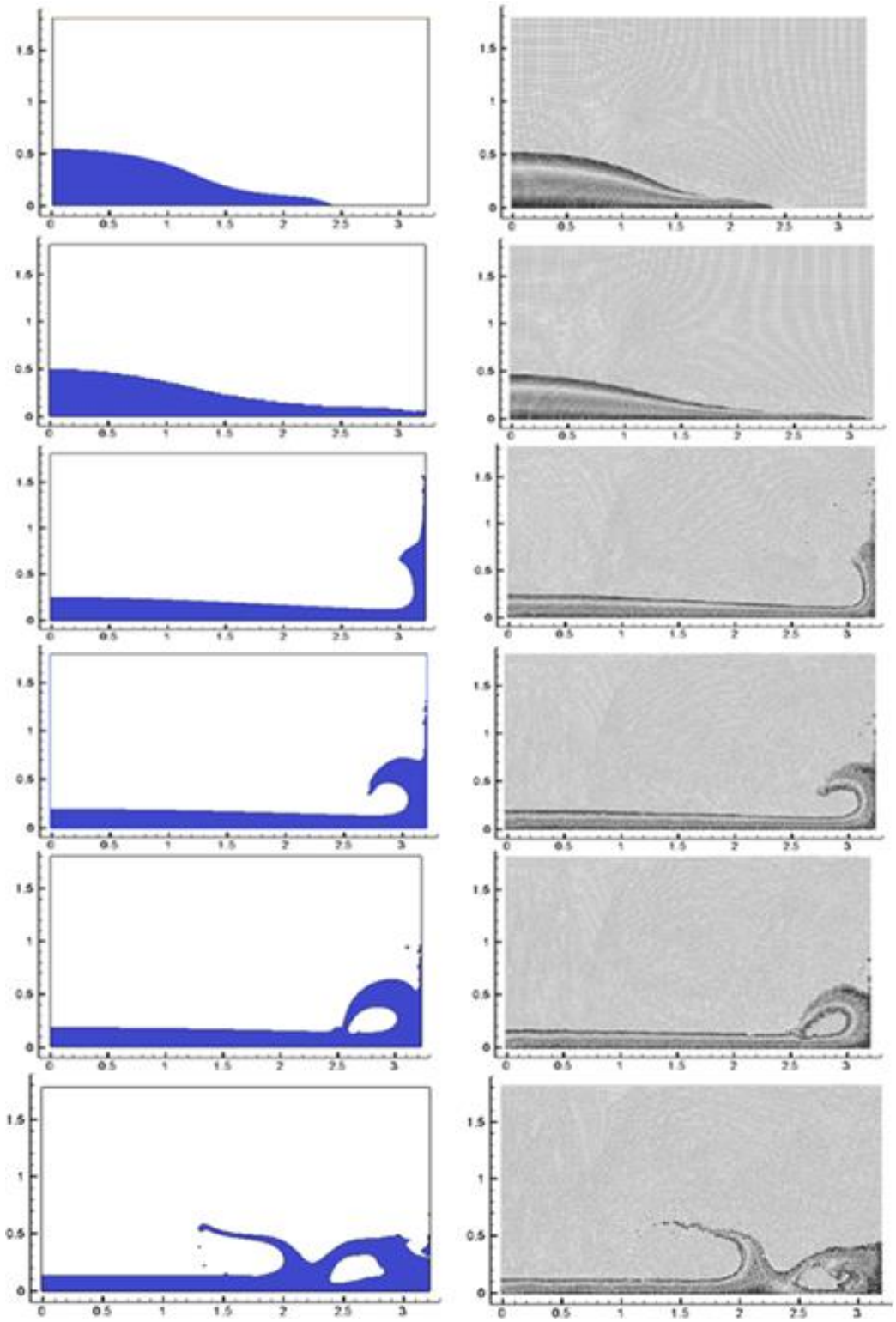

Figure 2 Contours of 2-D dam break ($t\sqrt{(g/h0)}$ =1.66, 2.43, 4.81, 5.72, 6.17, 7.37)
(Left: present computation, right: SPH computation)

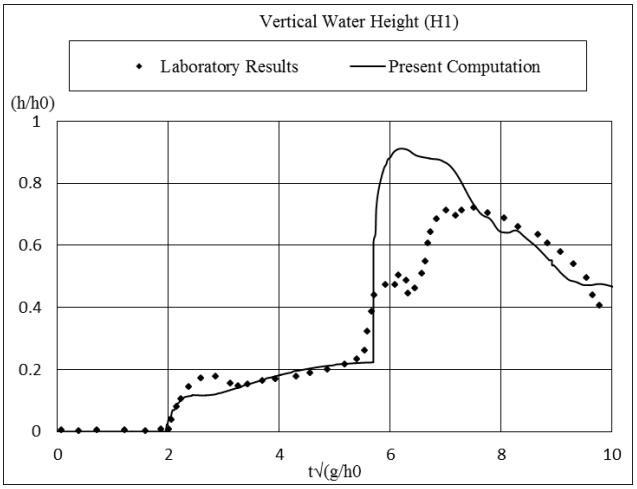

Figure 3 Comparison of the time history for vertical water height at H1

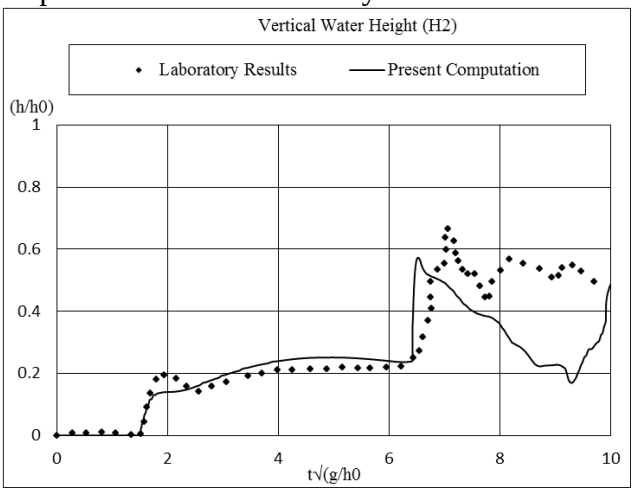

Figure 4 Comparison of the time history for vertical water height at H2

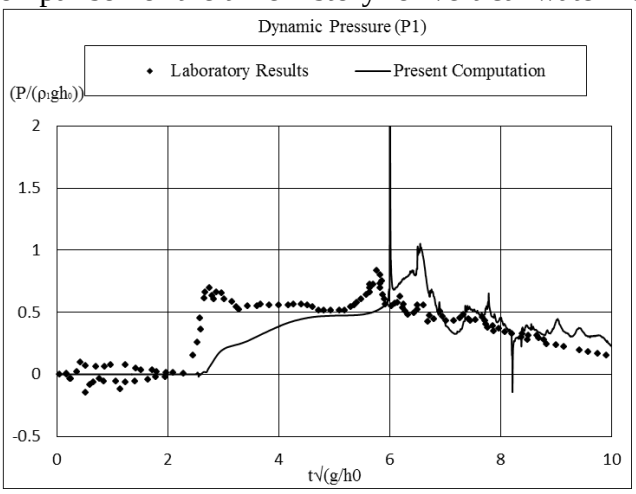

Figure 5 Comparison of the time history for dynamic pressure at P1

B. Tank Sloshing

The numerical simulation based on ANSYS Fluent software is used to solve the tank sloshing problem and compare with the experiments of liquid sloshing in a horizontally excited tank which have been performed by Liu and Lin (2008). The tank is 0.57 m long, 0.31 m wide and 0.3 m high. The static water depth is 0.15 m. The lowest natural frequency (ω_0) of liquid motion in the tank is 6.0578s^{-1}. The tank is fixed on an oscillating table in sinusoidal motion: x= -a*sin(t). The motion amplitude (a) is 0.005 m and the sloshing frequencies (ω) are $0.583\omega_0$ and $1.0\omega_0$, non-resonant and resonant cases, respectively. The water elevations were measured using three water height probes (H1, H2, and H3). The sketch of the sloshing experiment is shown in Figure 6. The sloshing problem can be simplified to a two-dimensional section. Dynamic mesh method is used to simulate the tank movement. The no-slip wall condition is imposed on the entire boundary and Laminar flow method is used in the calculations. Grid dependence test was carried out in the previous calculations and by contrasting data, a fine grid is adopted. The element size (δx) is uniform in the x-direction, whereas the element size (δz) varies in the z-direction which is refined locally at the interface between water and air, as shown in Table 1. Contrasting data have been omitted.

Table 1 Meshes employed in the grid dependence study

Grid	$x \times z$	δx	δz	Total elements number
Coarse	56×60	0.01	0.005	3360
Medium	70×75	0.008	0.004	5250
Fine	114×150	0.005	0.002	17100

The numerical method can be validated with the experimental data. The free surface elevation at H1, H2 and H3 is calculated and compared with experimental results. It could be seen that the present results have a good agreement with the experimental results, as shown in Figure 7 and Figure 8.

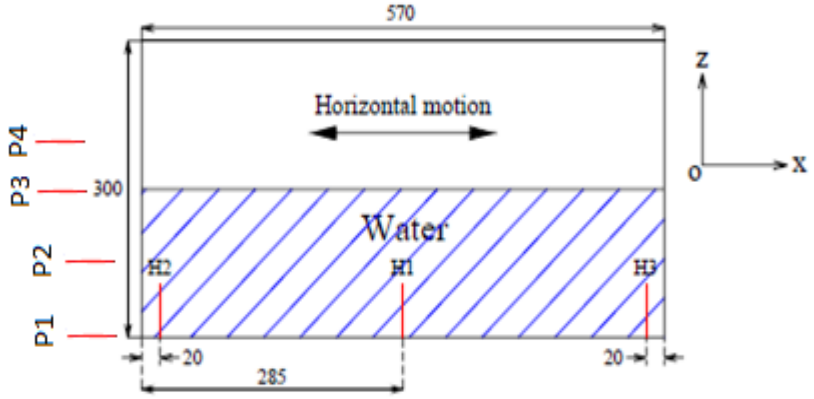

Figure 6 Sketch of the sloshing experiment (units: mm)

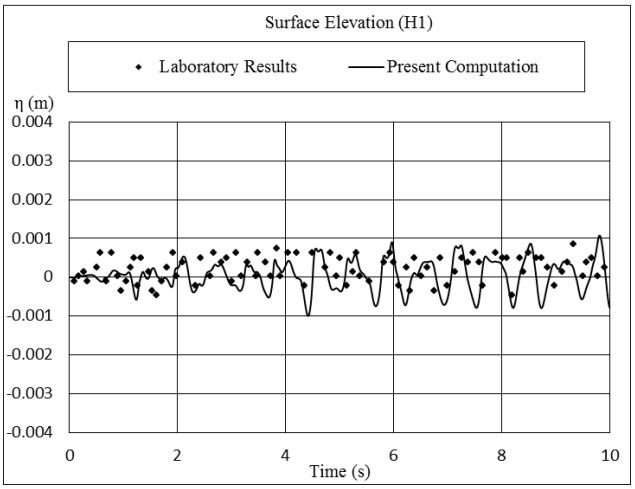

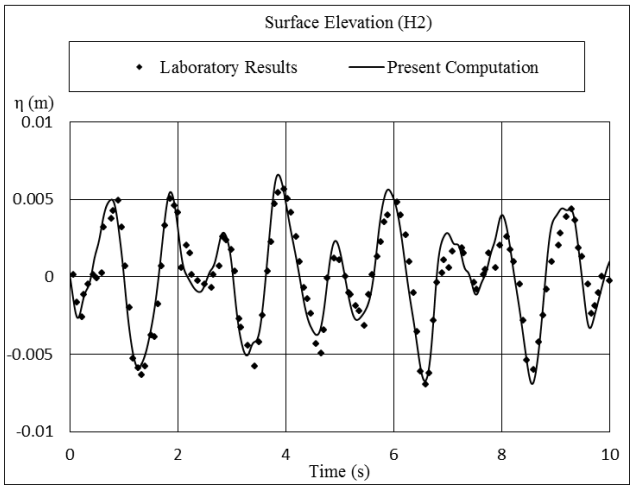

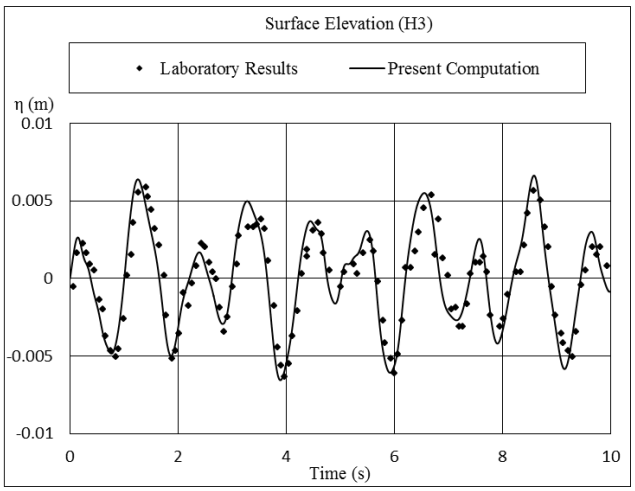

Figure 7 Comparison of free surface elevation at H1, H2 and H3 ($\boldsymbol{\omega}=0.583\boldsymbol{\omega_0}$)

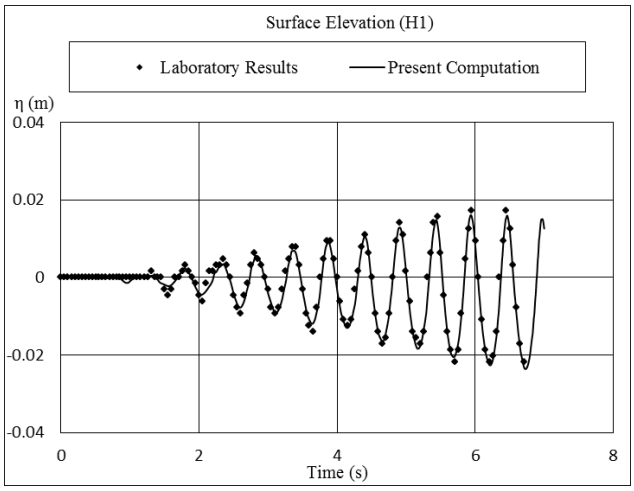

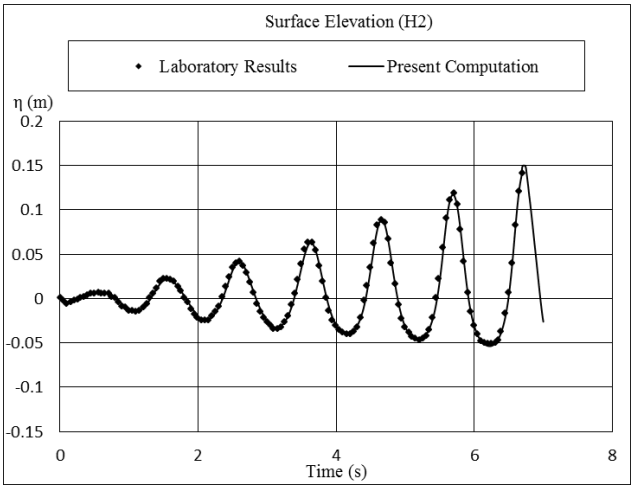

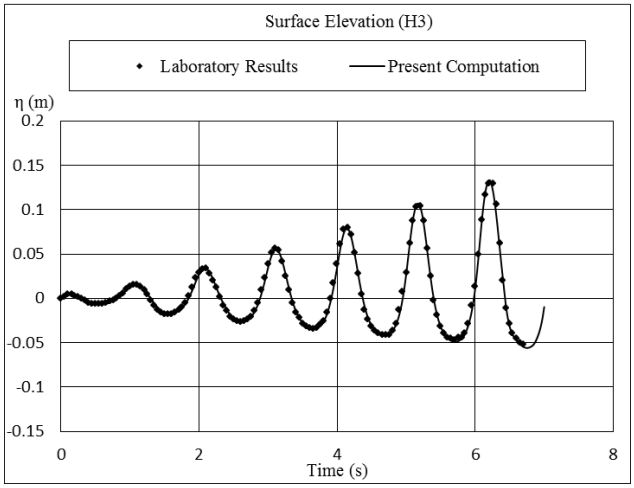

Figure 8 Comparison of free surface elevation at H1, H2 and H3 ($\boldsymbol{\omega}=1.0\boldsymbol{\omega_0}$)

Four pressure monitoring points are set at 0m, 0.075m, 0.15m and 0.2m in the z-direction, respectively. It can be seen in Figure 9 that for the resonance case ($\omega=1.0\omega_0$), the amplitude of pressure fluctuation increases gradually with time and the pressure fluctuates much stronger than the case for the non-resonance.

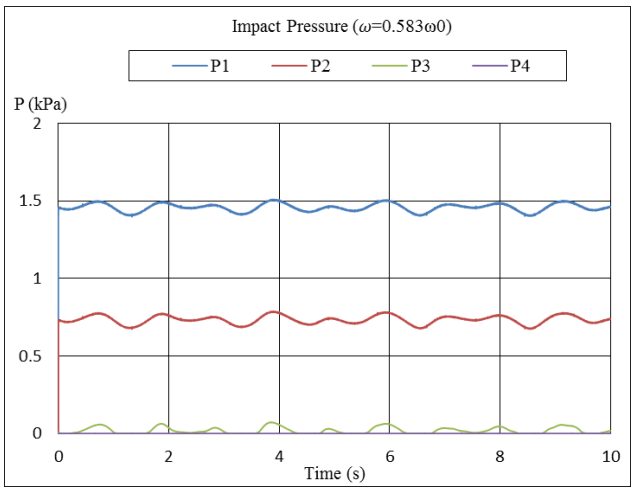

(a) $\omega=0.583\omega_0$

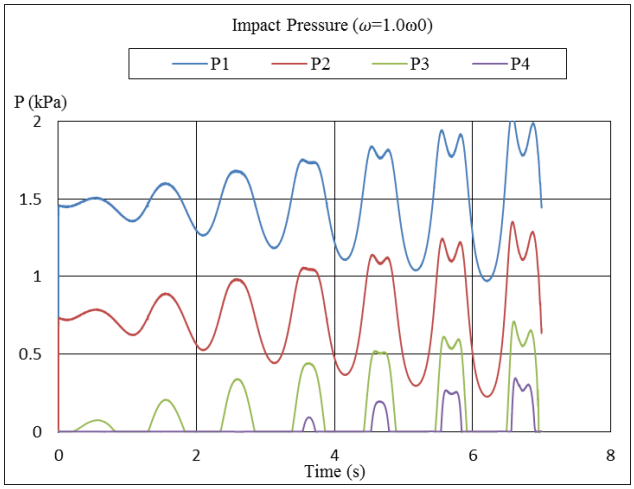

(b) $\omega=1.0\omega_0$

Figure 9 Time history for impact pressure at P1-P4

C. Dam Break and Tank Sloshing of Non-Newtonian Fluid

The dam-break flow involving non-Newtonian fluids is investigated here, based on Fluent software involving the VOF method. According to the experiments of non-Newtonian dam-break flows by Roberta Brondani Minussi, Carbopol 940 is used as experimental, which could be modelled by the Herschel-Bulkley constitutive equation.

$$\eta = 1/2[\tau_c(-\dot{D}_\Pi)^{-\frac{1}{2}} + 2^n k(-\dot{D}_\Pi)^{(n-1)/2}]$$

n: the flow index

k: the consistency index

τ_c: the yield stress

$\dot{D}$: the strain rate tensor ($\dot{D} = (\nabla u + \nabla u^T)/2$)

$\dot{D}_\Pi$: the second invariant of $\dot{D}$ ($\dot{D}_\Pi = [(tr(\dot{D}))^2 - tr(\dot{D}^2)]/2$))

Properties of this fluid used on the dam-break experiment are shown in Table 2.

Table 2 Property of Carbopol 940

Concentration	Yield pressure τ_c(Pa)	Consistency K (Pa.s^n)	Flow index n
11.6%	30.002	0.01	0.005

A sketch of the dam break experiment is shown in Figure 10. H0 is 100mm. The numerical data were compared with the experimental data and some published data in the literature. The present method showed better agreement with the experimental results, as indicated in Figure 11 and Figure 12.

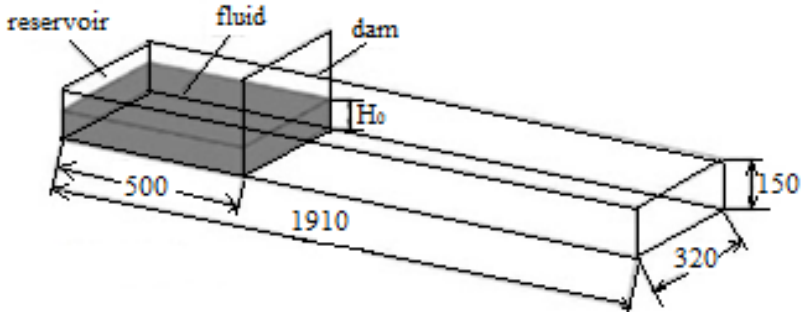

Figure 10 Sketch of dam break experiment (units: mm)

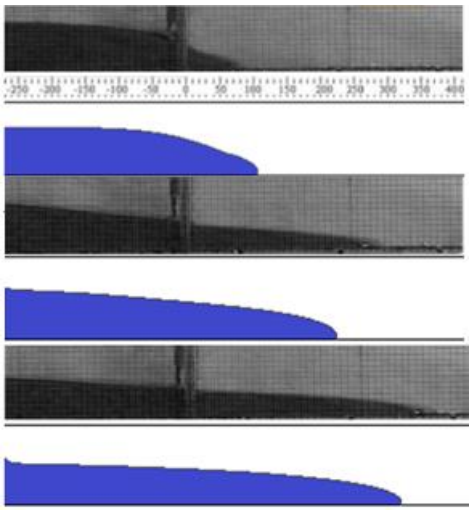

Figure 11 Numerical-experimental comparison at T=0.2s, 0.6s, and 1.0s

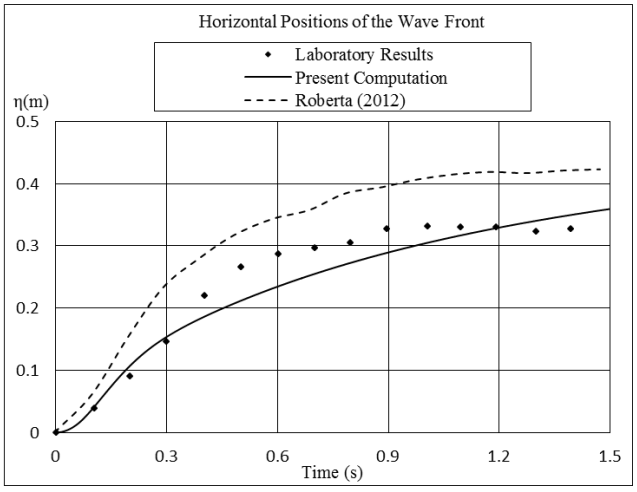

Figure 12 Horizontal positions of the wave front

The sensitivity analysis of the variables in the Herschel-Bulkley constitutive equation on the character of Carbopol 940 was studied including the dam break and tank sloshing, as shown in Figure 13 and Figure 14. However for the sloshing motion, when T>0s and T<1s, the tank has a horizontal velocity 0.4m/s and when t>=1s, the tank stops.

It is known that if n<1, the fluid is shear-thinning, while n>1 produces a shear-thickening fluid. Shearing thinning means viscosity decreases when the velocity gradient increases.

Yield pressure means when only the shear stress is greater than yield pressure (τ_c) the local fluid moves and the greater yield pressure, the more inert the fluid. If n=1 and τ_c=0, this model reduces to a Newtonian fluid. Figure 13 shows that liquefied cargoes which have low index n and yield pressure have large flow characteristic. For the instantaneous exciting experiment shown in Figure 14, when T<1s, water sloshing is severe and it has not the restriction of yield pressure. When T>1s, the non-Newtonian fluid will stay one side for a long time. During the carriage, the cargo will experience a transition from solid to partially liquefied state, and then to fully liquefied state. All of these three states have an impact on ship stability. When the cargo liquefied enough, this will greatly change the flow properties of the cargoes and tend to flow. The liquefied cargoes flow to one side of the ship and do not completely return, which influences the position of gravity centre of the ship and further reduces the ship stability.

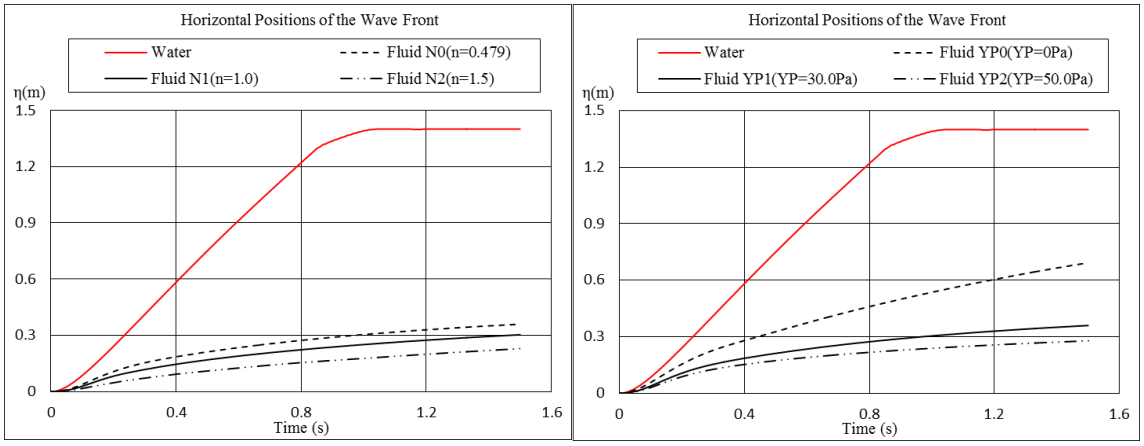

Figure 13 Horizontal positions of the wave front versus flow index n (left) and yield pressure $\boldsymbol{\tau_c}$ (right) for dam break

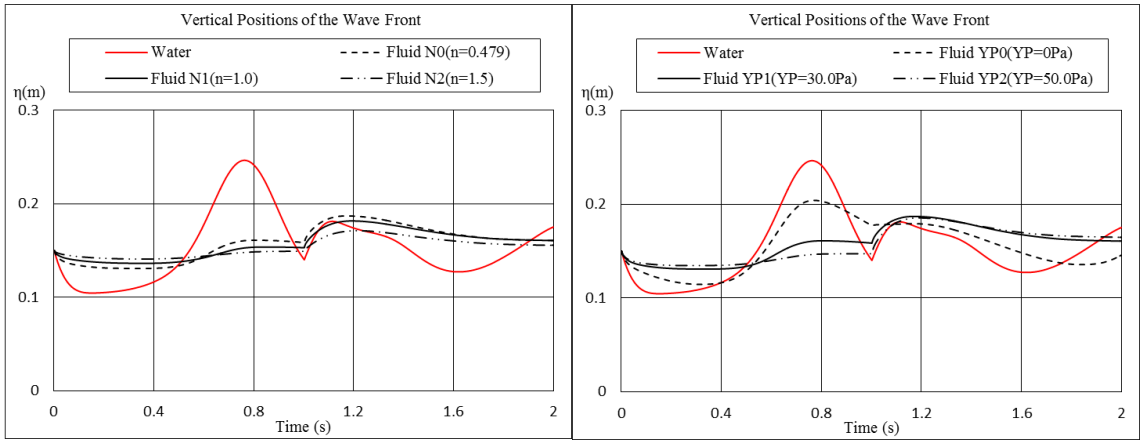

Figure 14 Vertical positions of the wave front versus flow index n (left) and yield pressure $\boldsymbol{\tau_c}$ (right) for tank sloshing (right wall)

Appendix 7: Paddle Wave Generating Method

For simulating ship response due to cargo shift in waves, paddle wave making method is used to generate regular wave and irregular wave (Sun & Incecik, 2015).

A. Linear Wave

Paddle wave generation method is to solve boundary values by Fourier method of potential flow theory. To derivate the paddle wave generating formula, length of paddle under water is l, paddle amplitude at water surface is E, and the wave spreading direction is positive. The water surface is x=0 and the static paddle is y=0.

The amplitude at different depth of paddle e is:

$$\begin{cases} e(y) = 0; & 0 \le y \le (h-1) \\ e(y) = \frac{E}{l}(y-h+l); & (h-1) < y \le h \end{cases} \quad (1)$$

The paddle horizontal displacement is:

$$x = e(y)\sin(\omega t) \quad (2)$$

The paddle horizontal velocity is:

$$u = \frac{dx}{dt} = \omega \cdot e(y) \cdot \cos \omega t \quad (3)$$

The fluid on the plane and the plane should have the same normal velocity:

$$\boldsymbol{c} \cdot \boldsymbol{n} = \boldsymbol{c_p} \cdot \boldsymbol{n} \quad (4)$$

$\boldsymbol{c}$: the velocity of fluid particle

$\boldsymbol{c_p}$: the velocity plane

$\boldsymbol{n}$: the unit outer normal vector

Based on small amplitude wave assumption, i.e. L ≫ A, denote φ to be velocity potential,

u and v to be horizontal and vertical velocity of wave at wave paddle respectively, then

$$\frac{\partial \varphi}{\partial x} = u = \omega \cdot e(y) \cdot \cos(\omega\, t) \quad (x = 0) \tag{5}$$

$$\frac{\partial \varphi}{\partial y} = v \qquad (x = 0) \tag{6}$$

Velocity potential satisfies Laplace equation,

$$\frac{\partial^2 \varphi}{\partial x^2} + \frac{\partial^2 \varphi}{\partial y^2} = 0 \tag{7}$$

The boundary condition in this case is as follows:

Vertical velocity at seabed is zero:

$$v = \frac{\partial \varphi}{\partial y} = 0 \qquad (y = 0) \tag{8}$$

The free surface boundary condition:

$$\frac{\partial^2 \varphi}{\partial^2 t} + g \cdot \frac{\partial \varphi}{\partial y} = 0 \quad (y = h) \tag{9}$$

General solution to the velocity potential of wave propagation is derived based on Fourier method:

$$\varphi = C_0 \frac{\omega}{k_0} \cosh(k_0 y) \sin(k_0 x - \omega t) - \sum_{n=1}^{\infty} C_n \frac{\omega}{k_n} \cosh(k_n y) e^{-k_n x} \cos(\omega t) \tag{10}$$

Solve the derivative of φ and substitute it in free surface boundary condition can yield:

$$-C_0 \omega \cosh(k_0 y) \sin(k_0 x - \omega t) \left(\frac{\omega^2}{k_0} - g\, tanh(k_0 y)\right) +$$

$$\sum_{n=1}^{\infty} C_n\, \omega\, cosh(k_n y)\, e^{-k_n x}\, cos(\omega t) \left(\frac{\omega^2}{k_n} + g\, tanh(k_n y)\right)\Big|_{y=0} = 0 \tag{11}$$

The dispersion relation is further derived as:

$$\frac{\omega^2}{k_0} - g \tanh(k_0 h) = 0 \tag{12}$$

$$\frac{\omega^2}{k_n} + g \tan(k_n h) = 0 \tag{13}$$

For (13), there is an infinite number of k corresponding to a specific ω, which is denoted as k_n. k_n lies in $(n\pi - \pi/2)/d \sim n\pi/d$ interval. C_o and C_n in (10) is solved based on boundary conditions. Substitute (10) to (5) and multiply by $\cosh(k_o y)$, followed by integrating:

$$C_o \int_0^h \cosh^2(k_0 y)\, dy + \sum_{n=1}^{\infty} C_n \int_0^h \cosh(k_0 y)\cos(k_n y)\, dy = \int_0^h \mathrm{e}(y)\cosh(k_0 y)\, dy \tag{14}$$

The dispersion relation (12), (13) can validate $\int_0^h \cosh(k_0 y)\cos(k_n y)dy = 0$, therefore:

$$C_o = 2k_0 \frac{\int_0^h \mathrm{e}(y)\,\mathrm{ch}(k_0 y)\, dy}{k_0 h + \cosh(k_0 h)\sinh(k_0 h)} \tag{15}$$

The final result of C_o is obtained by integrating (1):

$$C_o = \frac{2E}{k_0 l} \frac{k_0 l \sinh(k_0 h) - \cosh(k_0 h) + \cosh(k_0 h - k_0 l)}{k_0 h + \cosh(k_0 h)\sinh(k_0 h)} \tag{16}$$

The same approach can be applied to solve C_n:

$$C_n = \frac{2E}{k_n l} \frac{k_n l \sinh(k_n h) + \cosh(k_n h) - \cosh(k_n h - k_n l)}{k_n h + \cosh(k_n h)\sinh(k_n h)} \tag{17}$$

Furthermore, wave function in front of wave paddle is derived based on calculating average displacement of water particle in vertical direction from (8):

$$\begin{aligned} \eta(\mathrm{x},\mathrm{t}) = \int \frac{\partial \varphi}{\partial y} dt \Big|_{y=h} \\ = C_o \sinh(k_0 h)\cos(k_0 x - \omega t) \\ + \sum_{n=1}^{\infty} C_n \sin(k_0 y) e^{-k_o x} \sin(\omega t) \end{aligned} \tag{18}$$

The first part of right hand side of the equation above is propagating wave and second part

is standing wave. Standing wave can be neglected after moving away from wave paddle. The wave amplitude is also observed as:

$$A = C_o \sinh(k_0 h) \tag{19}$$

Substitute (16) with C_0 value:

$$A = \frac{2E}{k_0 l} \cdot \frac{k_0 l \sinh(k_0 h) - \cosh(k_0 h) + \cosh(k_0 h - k_0 l)}{k_0 h + \cosh(k_0 h) \sinh(k_0 h)} \cdot \sinh(k_0 h) \tag{20}$$

Therefore, two hydrodynamic transmission functions are obtained:

$$T(\omega) = \frac{A}{E} = \frac{2\sin(k_0 h)}{k_0 l} \frac{k_0 l \sinh(k_0 h) - \cosh(k_0 h) + \cosh(k_0 h - k_0 l)}{k_0 h + \cos(k_0 h) \sinh(k_0 h)} \tag{21}$$

$$T_1(\omega) = \frac{A}{\tilde{\theta}} = \frac{2\sin(k_0 h)}{k_0} \frac{k_0 l \sinh(k_0 h) - \cosh(k_0 h) + \cosh(k_0 h - k_0 l)}{k_0 h + \cos(k_0 h) \sinh(k_0 h)} \tag{22}$$

In (22), $\tilde{\theta}$ is paddle amplitude and satisfied the scenario in small amplitude wave theory below.

B. Irregular Wave

Based on the Longue-Higgins wave model theory, the realistic sea surface in space and time $\eta(x, t)$ can be expressed by the linear sum of the individual wave component with different wave amplitude, different wave frequency and random phase angle in the usual way as:

$$\eta(x, t) = \sum_{i=1}^{N} a_i * cos(k_i - \omega_i t + \tau_i) \tag{23}$$

Where a_i, k_i and ω_i are wave amplitude, wave number and relative wave frequency for group component i respectively. i=1, 2…N represents each wave component. And τ_i is the phase of wave component i. For generating of random wave, the phases of each wave component τ_i are selected in the usual way by randomly selecting a number between 0 and 2π using the random number function in Mathcad. Joint North Sea Wave Project

(JONSWAP) was carried out in 1968. Based on the given significant wave height and wave spectrum period, the formulation can be represented as:

$$s(\omega) = \frac{320*H_{1/3}^2}{T_p^4} \cdot \omega^{-5} \cdot exp(-\frac{1950}{T_p^4} \cdot \omega^{-4}) \cdot \gamma^A \quad (24)$$

$\lambda = 3.3$ (Peakedness factor)

$\omega_p = \frac{2\pi}{T_p}$ (Circular frequency at spectral peak)

σ a step function of ω

If $\omega < \omega_p$, σ=0.07

If $\omega > \omega_p$, σ =0.09

In this part, JONSWAP is selected as the target wave spectrum.

C. Wave Absorption

Wave absorption aims to reduce the wave energy in the numerical tank. Source terms in momentum equations are introduced in the absorption zone which can be written as:

$$\frac{\partial(\rho u)}{\partial t} + u\frac{\partial(\rho u)}{\partial x} + v\frac{\partial(\rho v)}{\partial y} = \mu\left(\frac{\partial^2 u}{\partial x^2} + \frac{\partial^2 u}{\partial y^2}\right) - \frac{\partial p}{\partial x} + D(x)u \quad (25)$$

$$\frac{\partial(\rho v)}{\partial t} + u\frac{\partial(\rho v)}{\partial x} + v\frac{\partial(\rho v)}{\partial y} = \mu\left(\frac{\partial^2 v}{\partial x^2} + \frac{\partial^2 v}{\partial y^2}\right) - \frac{\partial p}{\partial x} - \rho g + D(x)v \quad (26)$$

$D(x)$ is the damping coefficient function relative to x position.